Dissertation

submitted to the
Combined Faculties for the Natural Sciences and for Mathematics
of the Ruperto-Carola University of Heidelberg, Germany
for the degree of
Doctor of Natural Sciences

presented by

Diplom-Physikerin Jessica Agarwal
Born in Kiel, Germany

Oral examination: 26 July 2007

The Emission of Large Dust Particles from Comet 67P/Churyumov-Gerasimenko Constrained by Observation and Modelling of its Dust Trail

Referees: **Prof. Dr. Eberhard Grün**
Simon F. Green, PhD

Zusammenfassung.
Gegenstand der Arbeit ist die Untersuchung von Staubteilchen des Kometen 67P/Churyumov-Gerasimenko, die größer als 60μm sind. Zu diesem Zweck werden astronomische Bilder des Staub-Trails dieses Kometen ausgewertet. Solche Teilchen stellen den größten Teil der Staubmasse dar, die von Kometen in den interplanetaren Raum eingetragen werden. Im Gegensatz zu kleineren Teilchen verbleiben sie auf Trajektorien, die der des Kometen sehr ähnlich sind. Dem Beobachter erscheinen sie als eine schmale Struktur entlang des projizierten Kometenorbits, die als Staub-Trail bezeichnet wird. Die erste im Rahmen dieser Arbeit untersuchte Beobachtung wurde im April 2004 in sichtbarem Licht mit dem Wide Field Imager am ESO/MPG-2.2m-Teleskop auf La Silla (Chile) durchgeführt. Der Abstand des Kometen von der Sonne betrug zu diesem Zeitpunkt 4.7 A.E. Zwei weitere Beobachtungen wurden im August 2005 und im April 2006 im mittleren Infrarot (24 μm) ausgeführt mit der MIPS-Kamera auf dem Spitzer-Weltraumteleskop. In beiden Fällen war der Komet 5.7 A.E. von der Sonne entfernt. In der dazwischenliegenden Zeit, im November 2005, hatte er das Aphel passiert. Zur Interpretation der Daten werden simulierte Trailbilder erzeugt. Das verwendete Modell der kometaren Staubemission hat fünf freie Parameter: den Exponenten der Größenverteilung des Staubs, die Emissionsgeschwindigkeiten der Teilchen, die Effizienz des Strahlungsdrucks, die Albedo des Staubs und die Staubproduktionsraten. Für diese Parameter werden diejenigen Werte bestimmt, die eine bestmögliche Reproduktion der Beobachtungen ermöglichen. Die Ergebnisse für die erstgenannten vier Parameter entsprechen den Erwartungen. Die abgeleiteten Produktionsraten hingegen sind nicht vereinbar mit der Helligkeit der Kometenkoma, die beobachtet wurde, während sich der Komet im inneren Sonnensystem befand.

Abstract.
The abundance and properties of dust particles larger than about 60 μm emitted by comet 67P/Churyumov-Gerasimenko are constrained by evaluating astronomical images of its dust trail. Such particles carry the bulk of refractory mass released from comets to interplanetary space. In contrast to smaller particles, they remain on trajectories similar to that of the parent comet during many revolutions around the Sun. They are observable as a narrow structure along the projected comet orbit, the dust trail. The first observation evaluated in this thesis was carried out in April 2004 in visible light with the Wide Field Imager on the ESO/MPG 2.2m telescope on La Silla (Chile), when the comet was at a heliocentric distance of 4.7 AU. Two observations were performed in August 2005 and April 2006 at mid-infrared wavelengths (24 μm) with the MIPS instrument on board the Spitzer Space Telescope. In both instances, the comet was at 5.7 AU from the Sun, having passed aphelion in November 2005. To interpret the data, simulated images of the cometary dust trail are generated. The adopted model of cometary dust emission has five free parameters: the exponent of the dust size distribution, the particle emission speeds, the radiation pressure efficiency, the dust albedo, and the dust production rates. For these parameters, values are derived that are most suitable to reproduce the observations. The results for the first four parameters are in agreement with expectations. But the derived production rates cannot be reconciled with the measured brightness of the coma in the inner solar system.

Contents

Chapter 1

Introduction

Comets are the most obvious sources of interplanetary dust. Their nuclei are conglomerates of ice and dust on mostly highly elliptical orbits (Whipple, 1950, 1951). At sufficiently close distance to the Sun, the ices near the nucleus surface sublimate, releasing and accelerating the embedded dust. The characteristic bright coma and tail of a comet are due to sunlight scattered by these particles. Cometary dust seems to be a mixture of very different components, including amorphous and crystalline silicates and dark organic material. The particle sizes are thought to cover many orders of magnitude, ranging from compact nanometre-sized grains to fluffy aggregates several centimetres in size and larger.

Multiple evidence suggests that the total cross-section in a cometary coma is dominated by dust particles of 1 to 10 μm. Both the excess colour temperatures derived from fits to the thermal infrared emission of cometary comae (Divine et al., 1986) and the presence of silicate emission features in mid-infrared spectra of comets (Hanner, 2003) require a dominant grain size smaller than about 20 μm. On the other hand, the bulk of particles must be larger than visible wavelengths, because the spectral properties of the scattered light are similar to those of the incident sunlight (Grün and Jessberger, 1990). Also in situ measurements during spacecraft fly-bys suggest that the coma is dominated by μm-sized particles (Divine and Newburn, 1987; Green et al., 2004).

The dust mass, by contrast, that is released from a comet to interplanetary space is mainly carried by the mm-sized and larger particles (e. g. Sykes and Walker, 1992; Fulle, 2004; Green et al., 2004). These grains are characterised by low emission speeds (a few m/s) and little sensitivity to solar radiation pressure. They remain close to the comet orbit for many revolutions around the Sun and appear to the observer as a faint, linear structure, the *debris trail* or *dust trail* of the comet. Trails of eight short-period comets were first observed with the Infrared Astronomical Satellite (IRAS) in 1983 (Sykes et al., 1986a,b). A more recent survey with the Spitzer Space Telescope has shown that debris trails are commonly associated to short-period comets, because trails along the orbits of 27 out of 34 observed comets were detected (Reach et al., 2007). When the Earth passes through a cometary trail, a meteor shower is observed. For example, the famous meteor shower of the Leonids – observable annually in November – is related to the trail of comet 55P/Temple-Tuttle (e. g. Jenniskens, 2001). Of many meteor streams, however, the parent bodies remain unknown. For spacecraft missions to comets, the dust is not only one of

the primary topics of research, but also a safety issue. Despite the installation of specially designed dust shields, the Giotto spacecraft recorded attitude disturbances and damage to instruments due to impacts of mm-sized particles while passing by comet 1P/Halley at a distance of 600 km and with a relative speed of 70 km/s (Reinhard, 1986). Likewise, the 350-kg impactor of the Deep Impact probe registered several dust impacts before hitting the nucleus of comet 9P/Tempel 1 (A'Hearn et al., 2005). The Rosetta spacecraft of the European Space Agency is scheduled to reach comet 67P/Churyumov-Gerasimenko (henceforth abbreviated as 67P/C–G) in 2014, deploy a lander ("Philae") to the nucleus, and follow it into the inner solar system. Because of the low velocity of Rosetta relative to the comet, the consequences of dust impacts will be much less severe than they were for the fly-by missions. Detailed knowledge of the cometary dust environment will, nevertheless, be vital for the planning of spacecraft operations and thereby for the optimisation of the scientific return of the mission.

With astronomical means, mm-sized and larger particles are best studied when separated from smaller dust grains, which otherwise dominate the total cross-section in the field of view. Due to radiation pressure, sub-millimetre sized particles disperse into interplanetary space on timescales of weeks to months from their release. Their presence is not expected in the neighbourhood of an inactive comet far from the Sun. Larger particles remain close to the comet orbit on much longer time scales. Particles of different sizes can be discriminated because the tail of young, small particles is roughly aligned with the Sun-comet radius vector, while the trail of old, large grains is parallel to the orbit. To an observer well outside the orbital plane of the comet these populations appear at different position angles. This situation, for example, is given in the image of comet 2P/Encke shown in Reach et al. (2007). For comet orbits with low inclination against the ecliptic – such as 67P/C–G – the comet orbital plane as seen from Earth is projected to a nearly one-dimensional structure, and the angular separation of tail and trail is lost. The trails of such comets can therefore only be studied when the comet is not active; observations are best performed at heliocentric distances beyond 3 AU where water ice does not sublimate.

The purpose of the present work is to characterise the mm-sized and larger dust particles emitted from 67P/C–G by observations and modelling of its dust trail. Particular focus is given to the size distribution and production rates of such particles. Fulle et al. (2004) and Moreno et al. (2004) have inferred an unusually high production rate of mm-sized and larger particles at heliocentric distances between 3 AU and 1.7 AU before perihelion in 2002 by analysing images taken while the comet was active. The presence of significant quantities of large particles in the coma at 3 AU would have severe consequences for the Rosetta mission, because the lander is scheduled for deployment during this part of the trajectory. The goal of the present work was to investigate whether the observed tail and trail of 67P/C–G can be equally explained with a more conservative model of the cometary activity. To this purpose, astronomical images of the 67P/C–G trail had to be obtained that were appropriate for the analysis of the large dust grains alone. Then a simulation tool was developed in order to interpret the data.

This thesis is outlined as follows. Chapter 2 gives an overview of the basic physical and astronomical quantities relevant for the subsequent chapters; definitions are provided and data compiled from the literature. Chapter 3 contains a summary of observational data on comet 67P/C–G in the literature. In Chapter 4, the acquisition and processing of data

from three observing campaigns targeting the 67P/C–G dust trail – one in visible light and two in the mid-infrared – are described. Each of the final images covers about half a degree of the projected orbit behind the nucleus, and the data were obtained at heliocentric distances between 4.7 AU and 5.7 AU. In Chapter 5, a mathematical method to generate simulated images of a cometary trail is presented, and the adopted physical model of the dust emission is defined. The five free parameters of this model are constrained in Chapter 6 in such a way that the simulated images reproduce the observations. The results are discussed in Chapter 7.

Chapter 2

Cometary Dust

This chapter summarises the current knowledge on cometary dust as far as it is relevant for this work. The definitions of some quantities used in the following chapters are given, values for specific parameters are compiled from the literature. The data discussed in this chapter were not obtained specifically from observations of 67P/C–G but from different samples of comets or theoretical studies, as indicated in the text.

2.1 Terminology – Trail, Tail, Antitail and Neckline

In this work, "trail" is used to describe all dust observed along the projected orbit of the comet, while "old trail" refers to particles emitted at least one orbital period back, i. e. during the 1995/96 apparition of 67P/C–G or earlier. Dust emitted during the last apparition in 2002/03 is considered as "young". The "tail" of a comet consists of smaller particles that are driven away from the comet orbit towards the outer solar system by solar radiation pressure. The term "antitail" describes a part of the tail that seems to point towards the Sun instead of away from it. This, however, is a purely projectional effect. Viewed in three dimensions there is no difference between an ordinary tail and an antitail. A "neckline" (Kimura and Liu, 1977; Richter et al., 1991; Müller et al., 2001) consists of large particles emitted at a true anomaly of 180° before the observation. The orbital periods of large particles are similar to that of the parent comet. Their orbits in general are inclined with respect to the comet orbit, but the particles cross the orbital plane of the comet twice during each revolution around the Sun. One of the intersection points is given by the point of emission. The other intersection point lies on the line of nodes defined by the emission point and the Sun. The position of the second intersection point on the line of nodes depends on the semi-major axis of the particle orbit. Since the orbital periods are less sensitive to small changes of the orbital energy than the semi-major axes (Kepler's third law), large particles emitted at a given time cross the orbital plane of the comet almost simultaneously, but at different positions along the nodal line. To an observer in, or close to the comet orbital plane, they appear as a bright line.

2.2 Material and Bulk Density

Cometary dust grains are assumed to be fluffy aggregates of submicron-sized building-blocks (Greenberg and Li, 1999). The material of the building blocks is a mixture of both amorphous and crystalline silicates on the one hand, and carbonaceous material on the other (e. g. Hanner, 2003; Lisse et al., 2006). The silicates include a component of crystalline minerals that must have been processed at high temperatures close to the Sun (Brownlee et al., 2006) and afterwards transported to the cold outer regions of the solar system to be included in the icy agglomerate of the comet nucleus. While the building-blocks have the bulk density of the material (a few g/cm^3 for silicates), the overall density of the aggregates is lower. Divine et al. (1986) have argued that the bulk density of the aggregates decreases with increasing grain size. In situ data have not yet provided definitive results on this issue. For modelling purposes, constant values in the range of 0.1 to 1 g/cm^3 are widely used (Landgraf et al., 1999; Fulle et al., 2004; Crifo et al., 2004; Green et al., 2004).

2.3 Scattering of Light

The product of the geometric albedo p and the phase function $j(\alpha)$ relates the cross section of a dust particle to the intensity scattered by it. The phase angle α is the angle between the directions to the observer and to the source of the incident radiation as seen from the scattering particle. The geometric albedo of an object is defined as the ratio of the intensities reflected backwards (α = 0) by the object and by a Lambert scattering disc of the same geometric cross section (Hanner et al., 1981). The phase function $j(\alpha)$ describes the ratio between the intensities scattered to the phase angle α and to the backward direction. In the following, the normalisation $j(\alpha = 0) = 1$ (Müller, 1999) is used, which is different from the one given by Divine (1981).

The term "specific intensity" (I) is used in the following to describe power emitted or received per unit solid angle per unit area perpendicular to the beam direction, whereas "intensity" (J) is in units of power per unit (perpendicular) area.

Scattering by a Lambert Surface

A Lambert surface scatters an equal specific intensity I_L to all directions. A detector of area $\mathrm{d}A$ at a distance r from the Lambert surface appears under the solid angle $\mathrm{d}\Omega = \mathrm{d}A/r^2$. A Lambert surface of area $\mathrm{d}a$ occupies the solid angle $\mathrm{d}\omega = \mathrm{d}a\cos\theta/r^2$ seen from the detector, where θ is the angle between the direction to the observer and the normal of the Lambert surface. Since the specific intensity received by the detector is equal to the specific intensity emitted by the surface, I_L, the power received by the detector is $P_\mathrm{rec,L} = I_\mathrm{L}\,\mathrm{d}A\,\mathrm{d}\omega = I_\mathrm{L}\,\mathrm{d}A\,\mathrm{d}a\cos\theta/r^2$. The measured intensity $J_\mathrm{rec,L} = P_\mathrm{rec,L}/\mathrm{d}A$ therefore depends on $\cos\theta$.

The total power P_em emitted by a Lambert surface $\mathrm{d}a$ to the hemisphere $\Omega_{1/2}$ is given

by

$$\begin{aligned} P_{\rm em} &= \int_{\Omega_{1/2}} I_{\rm L}\,{\rm d}a\,\cos\theta\,{\rm d}\Omega \\ &= 2\pi\,I_{\rm L}\,{\rm d}a\int_0^{\pi/2}\cos\theta\sin\theta\,{\rm d}\theta \\ &= \pi\,I_{\rm L}\,{\rm d}a. \end{aligned} \tag{2.1}$$

If the surface is illuminated with parallel, normally incident light of the intensity $J_{\rm inc}$, the incident power is $P_{\rm inc} = J_{\rm inc}\,{\rm d}a$, which is equal to the emitted power $P_{\rm em}$ if the surface is white. Hence

$$I_{\rm L} = J_{\rm inc}/\pi. \tag{2.2}$$

The intensity received from a white Lambert surface by an observer looking face-on at the surface is

$$J_{\rm rec,L}(\theta = 0) = \frac{J_{\rm inc}}{\pi}\frac{{\rm d}a}{r^2}. \tag{2.3}$$

Scattering by an Arbitrary Body

An arbitrary body "d" (e. g. a dust particle) of the cross section ${\rm d}a$ as seen from the source of the incident light, receives the intensity $J_{\rm inc}$, whereas an observer at the phase angle α = 0 receives the intensity $J_{\rm rec,d}$ (0) from that body. By definition, the geometric albedo p of this body is

$$p = \frac{J_{\rm rec,d}(0)}{J_{\rm rec,L}(0)} = \frac{J_{\rm rec,d}(0)}{J_{\rm inc}}\frac{\pi r^2}{{\rm d}a}. \tag{2.4}$$

And the intensity received by the observer from a body characterised by the geometric albedo p is

$$J_{\rm rec,d(0)} = p\,\frac{{\rm d}a}{r^2}\,\frac{J_{\rm inc}}{\pi}. \tag{2.5}$$

From the point of view of the scattering body, $P_{\rm refl}$ = $J_{\rm rec,d}(0)\,{\rm d}A$ is the total power reflected by the surface ${\rm d}a$ to the solid angle ${\rm d}\Omega$ = ${\rm d}A/r^2$ under the angle α = 0 with the direction of the incident light. If the body is symmetric about the direction of the incident light, an observer at the phase angle α from this direction receives the intensity $J_{\rm rec,d}(\alpha)$ = $j(\alpha)J_{\rm rec,d}$ (0), where $j(\alpha)$ is the phase function. The power scattered to the solid angle ${\rm d}\Omega$ = ${\rm d}A/r^2$ under the phase angle α is

$$P_{\rm sca}(\alpha) = J_{\rm rec,d}(\alpha)\,{\rm d}A = j(\alpha)\,p\,\frac{{\rm d}a\,{\rm d}A}{r^2}\,\frac{J_{\rm inc}}{\pi}\,. \tag{2.6}$$

Measured Geometric Albedo and Phase Function of Dust

Divine et al. (1986) deduce from Earth-based observations that dust from different comets displays similar optical properties. The colour of the scattered light is neutral to slightly red at wavelengths between 0.36 μm and 2.2 μm (Divine et al., 1986). Laboratory measurements and theoretical studies indicate that the geometric albedo is a function of the

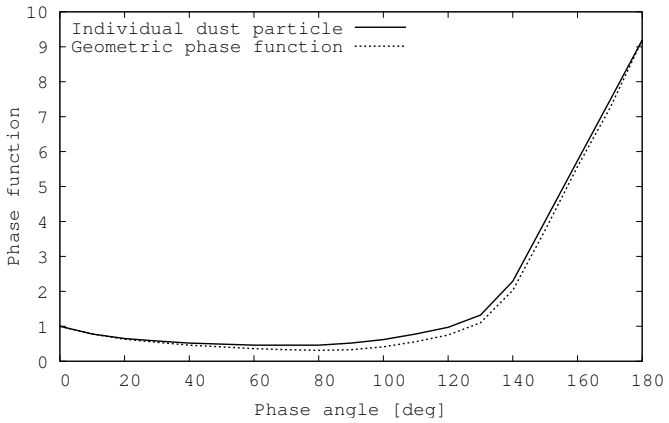

Figure 2.1: Dust phase functions. Solid line: Phase function of an individual dust particle as given in Divine (1981), normalised to j (α = 0) = 1 instead of $\int_{4\pi} j(\alpha)\, d\Omega$ = 1 in the original paper. Dashed line: Geometric phase function $j_{\mathrm{geo}}(\alpha)$ introduced by Müller (1999) and explained in Section 2.6.

particle size (McDonnell et al., 1991). Earth-based observations of cometary dust are not suitable to investigate this matter because they only provide average data for the ensemble of particles along a line of sight.

To derive the dust phase function from astronomical observations, a given object must be observed at different phase angles, i. e. at different times for Earth-based observations. Since the total cross section of dust in the field of view (FOV) is not constant with time, an appropriate normalisation is needed, for which two methods are used (Divine et al., 1986). The first is based on the assumption that the dust-to-gas ratio remains constant over time (Millis et al., 1982; Meech and Jewitt, 1987; Schleicher et al., 1998). The normalisation is achieved via gas production rates measured simultaneously with the $Af\rho$ parameter defined in Section 2.6. The second method, preferable but more laborious, consists in normalising the scattered intensity by means of the simultaneously measured thermal infrared emission from the same volume (Ney, 1974; Ney and Merrill, 1976; Ney, 1982; Tokunaga et al., 1986; Hanner and Newburn, 1989; Gehrz and Ney, 1992). The emerging phase function of cometary dust is characterised by a distinct forward and a gentle back-scattering peak with a plateau in between (Kolokolova et al., 2004). Divine (1981) derived from data given in Ney (1974), Ney and Merrill (1976), and Ney (1982) the phase function shown in Figure 2.1 (solid line).

Like the phase function, the geometric albedo of dust is derived from the simultaneous observation of the scattered visible and the thermally emitted infrared light, either directly at α = 0 or at an arbitrary phase angle and assuming a given phase function. Hanner and Newburn (1989) obtain p = 0.05 at a wavelength of 1.2 μm, while Divine et al. (1986) give $p = 0.03 \pm 0.01$ at 500 nm. From the generally low albedo, Kolokolova et al. (2004) infer that there is no significant population of cold, bright (and possibly icy) grains that would contribute to the scattered light but not to the thermal emission. There is some indication that the dust geometric albedo is higher for comets beyond 3 AU (Hanner and Newburn, 1989), which may point in the same direction.

2.4 Radiation Pressure

with The ratio of the solar gravity to the radiation pressure force, β, depends only on material properties of the dust grains, not on their distance from the Sun:

$$\beta = \frac{3\,L_\odot}{16\,\pi c\,G M_\odot}\frac{Q_{\rm pr}}{\rho s}. \tag{2.7}$$

$L_\odot$ and $M_\odot$ are the luminosity and mass of the Sun, c is the speed of light, and G the gravitational constant (values are listed in Appendix E). $Q_{\rm pr}$ is the radiation pressure efficiency of the grain having a bulk density ρ and an effective radius s (Burns et al., 1979; Divine et al., 1986). It represents the absorption and scattering properties of the grain averaged over the solar spectrum. For homogeneous spheres and some other simple shapes, $Q_{\rm pr}$ can be calculated in an exact way from the complex refractive index of the material according to Mie theory (Mie, 1908; Bohren and Huffman, 1983). For more complicated structures, a variety of theoretical and experimental approaches exists to obtain $Q_{\rm pr}$ (Gustafson et al., 2001). While for particle sizes on the order of 0.01 to 1 μm , β depends sensitively on material, shape, structure, surface properties, and size of the particles (Burns et al., 1979), it is about constant for much smaller particles, and proportional to 1/(ρs) for large ones, i. e. in the geometric optics regime (Gustafson, 1994). For sub-millimetre and larger particles, $Q_{\rm pr}$ is approximately constant (Divine et al., 1986).

Since both solar gravity and radiation pressure force are inversely proportional to the heliocentric distance and point radially away from the Sun, radiation pressure can be included in the equation of motion of a particle by introducing a modified gravitational potential substituting the gravitational constant, G, by $\tilde{G} = G(1-\beta)$.

2.5 Infrared Emission

The total power $P_{\rm abs}$ absorbed by a spherical particle of radius s at the heliocentric distance $r_{\rm h}$ (in AU) with the absorption characterised by the function $Q_{\rm abs}(s,\lambda)$ is

$$P_{\rm abs} = \frac{1}{r_{\rm h}^2}\,\pi s^2 \int_0^\infty F_\odot(\lambda)\,Q_{\rm abs}(s,\lambda)\,{\rm d}\lambda, \tag{2.8}$$

where $F_\odot(\lambda)\,{\rm d}\lambda$ is the solar spectrum at 1 AU, giving the intensity crossing unit area in the wavelength interval $(\lambda, \lambda + {\rm d}\lambda)$.

According to Kirchhoff's law, the emission and absorption of a particle are described by the same function $Q_{\rm abs}(s,\lambda)$. The total power $P_{\rm em}$ emitted by a particle of radius s and temperature T is given by

$$P_{\rm em} = 4\pi s^2 \int_0^\infty \pi B(\lambda,T)\,Q_{\rm abs}(s,\lambda)\,{\rm d}\lambda. \tag{2.9}$$

$B_\lambda(\lambda,T)$ is Planck's function, describing the thermal emission of a blackbody of temper-

ature T in the wavelength interval $(\lambda, \lambda + \mathrm{d}\lambda)$:

$$B_\lambda(\lambda, T)\,\mathrm{d}\lambda = \frac{2hc^2}{\lambda^5}\frac{1}{\mathrm{e}^{hc/k_\mathrm{B}\lambda T} - 1}\,\mathrm{d}\lambda. \tag{2.10}$$

$B(\lambda, T)$ is in units of power per unit solid angle, per unit area perpendicular to the beam direction, per wavelength interval. In thermodynamic equilibrium, $P_\mathrm{abs} = P_\mathrm{em}$:

$$\frac{1}{4\,r_\mathrm{h}^2}\int_0^\infty F_\odot(\lambda)\,Q_\mathrm{abs}(s,\lambda)\,\mathrm{d}\lambda = \int_0^\infty \pi\frac{2hc^2}{\lambda^5}\frac{1}{\mathrm{e}^{hc/k_\mathrm{B}\lambda T} - 1}\,Q_\mathrm{abs}(s,\lambda)\,\mathrm{d}\lambda, \tag{2.11}$$

were h and k_B are Planck's and Boltzmann's constants, respectively. From this equation the equilibrium temperature of a particle for given s and r_h can be calculated using a recursive numerical procedure.

Q_abs is related to the Bond albedo A at a given wavelength via $Q_\mathrm{abs} = 1 - A$, where the Bond albedo is defined as the ratio of the total intensity scattered by a grain to the total intensity incident on it (Allen, 1973). The Bond albedo is related to the geometric albedo (Section 2.3) via the phase integral:

$$A = \frac{p}{\pi}\int_{4\pi}\phi(\alpha)\,\mathrm{d}\Omega. \tag{2.12}$$

The dependence of Q_abs on the particle size and the wavelength is governed by the size parameter $x = 2\pi s/\lambda$. In addition, Q_abs is generally influenced by the material, shape, and porosity of the grain, especially for $x \leq 1$, whereas for $x \gg 1$, Q_abs can be treated as independent of x (Bohren and Huffman, 1983).

Assuming that the average Bond albedo at visible wavelengths is given by A, and that the absorption efficiency for infrared light is $Q_\mathrm{abs} = 1$, Equation 2.11 can be approximated by

$$\frac{(1-A)\,I_\odot}{4\,r_\mathrm{h}^2} = \sigma\,T^4, \tag{2.13}$$

where σ is the Stefan-Boltzmann constant and $I_\odot$ the solar flux at 1 AU. The resulting equilibrium temperature is

$$T(r_\mathrm{h}, A) = \left(\frac{I_\odot}{4\,\sigma}\right)^{\frac{1}{4}}(1-A)^{\frac{1}{4}}\frac{1}{\sqrt{r_\mathrm{h}}} = 278.8\,\mathrm{K}\,(1-A)^{\frac{1}{4}}\,\frac{1}{\sqrt{r_\mathrm{h}}}. \tag{2.14}$$

For $A = 0.18$ (corresponding to $p = 0.04$ and the phase function given in Section 2.3), equilibrium temperatures of 265 K at 1 AU and 119 K at 5 AU are obtained. This corresponds to peak emission wavelengths of 19 μm and 43 μm, respectively[1].

The absorption efficiency of small particles is in general a complicated function of the size parameter x and of the particle properties. The diversity of information found in the literature hints at the complexity of the problem. On the observational side, two com-

[1]The relation between the maximum of the spectrum of a blackbody and its temperature is given by Wien's displacement law: $\lambda_\mathrm{max} = b/T$, where the value of Wien's displacement constant b is given in Appendix E.

monly observed spectral properties of cometary comae are attributed to small particles.

(1) The colour temperatures derived from spectra in the range of 3 to 20 μm are higher than the equilibrium temperature for the heliocentric distance concerned. This is interpreted as an indication that the prevailing grain size is below 10 μm (Divine et al., 1986) and that such small particles cannot effectively emit the absorbed energy at wavelengths larger than their sizes. Hence they heat to temperatures corresponding to peak emission wavelengths that are smaller than the particle size (Divine et al., 1986).

(2) Particles of similar size are held responsible for the presence of the silicate emission features observed in spectra around 10 μm and 16 – 35 μm. These are resonance modes, distinct peaks in $Q_{\rm abs}(\lambda)$, occurring only if the particle size is much smaller than the wavelength. The shape and exact spectral position of the emission features can be used to constrain the material, porosity, shape, and crystallisation state of the particles (e. g. Hanner, 2003; Lisse et al., 2006).

2.6 Coma Brightness – Definition of $Af\rho$

The brightness of a cometary coma is proportional to the dust production rate. To compare data obtained under different observational circumstances, it must, however, be ensured that all other parameters affecting the measured intensity are properly accounted for before the dust production rate is inferred. The quantity $Af\rho$ was defined for this purpose by A'Hearn et al. (1984). $Af\rho$ stands for the product of albedo A, filling factor f of grains within the field of view, and the radius ρ of the aperture at the comet. It is measured as follows:

$$Af\rho = 4\frac{\Delta^2 (r_{\rm h}/1{\rm AU})^2}{I_{\rm sun}^{\rm (filter)}} \times \frac{I_{\rm dust}^{\rm (filter)}}{\rho}, \tag{2.15}$$

where $r_{\rm h}$ and Δ are the heliocentric and geocentric distances of the comet during the observation, and ρ is the radius of the circular aperture on which the coma intensity $I_{\rm dust}^{\rm (filter)}$ was measured using a given filter. $I_{\rm sun}^{\rm (filter)}$ is the intensity of the Sun at 1 AU heliocentric distance seen through the same filter. Provided that the dust particles move away from the nucleus on straight trajectories and are not subject to processes altering their scattering behaviour, $Af\rho$ is independent of the employed aperture radius, of the heliocentric and geocentric distances, and – to the extent that the dust can be considered as "grey" (see Section 2.3) – of the spectral band in which the observation was carried out.

For an isotropic coma and discrete dust sizes s_j, Müller (1999) relates $Af\rho$ to the production rates $Q_{{\rm d},j}\,(s_j)$ via the dust emission speeds $v_{{\rm d},j}$ (Section 5.4.9), the geometric albedo p, and the phase function $j(\alpha)$ (Section 2.3):

$$Af\rho = 2\pi\, p\, j(\alpha) \sum_j s_j^2\, \frac{Q_{{\rm d},j}}{v_{{\rm d},j}}. \tag{2.16}$$

The relative magnitudes of the $Q_{{\rm d},j}$ rates are given by the size distribution (Section 2.7).

$Af\rho$ depends on the phase angle of the observation, due both to the scattering properties of a single dust grain (Schleicher et al., 1998) and – unless the coma is isotropic – to projection effects (Müller, 1999). In a non-isotropic coma, the timescale on which

the particles leave a given field of view depends on the angle between the main emission direction and the line of sight, with higher measured $Af\rho$ for a line of sight parallel or close to the main emission direction. Müller (1999) therefore introduced a *geometric* phase function $j_{\mathrm{geo}}(\alpha)$ that is characteristic of the specific pattern of emission of a given nucleus. For a coma where the dust production rate is proportional to the cosine of the local zenith angle of the Sun, the geometric phase function is shown by the dashed line in Figure 2.1. Schleicher et al. (1998) obtained from multiple observations of comet 1P/Halley a phase angle dependence of $Af\rho$ that for small phase angles is slightly steeper than the Divine phase function for a single particle (Figure 2.1, solid line). This supports the introduction of a geometrical correction to the phase function by Müller (1999).

In practice, for many comets $Af\rho$ seems to depend on the aperture size despite its definition (e. g. Schleicher et al., 1998; Schleicher, 2006, and references therein). This implies that the brightness distribution in the coma deviates from the $1/\rho$-profile assumed on the introduction of $Af\rho$. Possible causes for this deviation include changes in the physical properties of the grains as they travel outward (e. g. loss of volatiles or fragmentation), the action of radiation pressure modifying the straight trajectories of small particles inside the field of view, or a long-lasting population of large particles (Schleicher et al., 1998).

2.7 Dust Size Distribution

The size distribution of cometary dust has been inferred from both astronomical images and data measured in situ. While the former yield a *size* distribution, the latter contain information on the *masses* of the particles. For optical images, the determined sizes scale directly with the particle albedo (Section 2.3). The conversion from size to mass requires knowledge of the bulk density of the particles (Section 2.2).

A mass or size distribution can be specified in the form of either a *differential* or a *cumulative* distribution. The cumulative mass distribution $F(m)$ gives information on the fraction of particles that have a mass greater than some mass m_0:

$$n\,(m > m_0) = F(m_0). \tag{2.17}$$

The differential mass distribution $f(m)$ characterises the relative abundance n of particles inside a mass interval $[m_1, m_2]$:

$$n\,(m_1 < m < m_2) = \int_{m_1}^{m_2} f(m)\,\mathrm{d}m = F(m_1) - F(m_2). \tag{2.18}$$

If the mass of a particle can be converted to a size by a relation $s(m)$, a corresponding differential size distribution $g(s)$ exists:

$$\int_{m_1}^{m_2} f(m)\,\mathrm{d}m = \int_{s(m_1)}^{s(m_2)} g\,(s)\,\mathrm{d}s. \tag{2.19}$$

It is generally assumed that – at least in intervals of the total mass range covered by cometary dust – the distribution can be approximated by a power law. In the literature, both the exponents γ of the *cumulative mass distribution* $F(m) \sim m^{-\gamma}$ and α of the *differential size distribution* $g(s) \sim s^{\alpha}$ are commonly used. For a constant bulk density in the concerned size interval, $m(s) \propto s^3$ and $\mathrm{d}m \propto s^2 \mathrm{d}s$. Hence the exponents γ and α are related by

$$\alpha = -3\gamma - 1. \tag{2.20}$$

The mass distribution at the nucleus is different from the one in the coma. To derive one from the other, some knowledge of the (mass-dependent) velocity of the dust grains is needed. The velocity has to be inferred from modelling, because it has not yet been measured. In general, large particles are more abundant in the coma than close to the surface because of their lower emission speeds. The relation between the size distributions in the coma and at the nucleus may be further complicated by fragmentation or evaporation of grains (McDonnell et al., 1987, 1991) and by an inhomogeneous distribution of surface activity (Fulle et al., 1995).

In situ data on the dust mass distribution were obtained by the dust instruments on board the spacecraft VeGa 1 and 2 and Giotto at comet 1P/Halley in 1986 (McDonnell et al., 1987; Divine and Newburn, 1987; McDonnell et al., 1991; Fulle et al., 1995), on board Giotto at comet 26P/Grigg-Skjellerup in 1992 (McDonnell et al., 1993), and on board Stardust at comet 81P/Wild 2 in 2004 (Tuzzolino et al., 2004; Green et al., 2004). The measured quantity is not the mass distribution of dust as released from the nucleus but the cumulative flux or fluence on the concerned instrument. The fluence is defined as the flux integrated over the spacecraft trajectory, it represents therefore an average mass distribution. The flux (or the fluence measured in only sections of the trajectory) showed significant variation with time during both the 1P/Halley and the 81P/Wild 2 fly-bys.

Still no general agreement has been reached on the interpretation of the data with respect to the dust mass distribution at the nucleus, but authors do agree that the mass of dust in the coma is dominated by millimetre-sized and larger particles. The cumulative fluences registered at the various spacecraft show different exponents for large and small particles. The interpretations of this observation are not unanimous. Table 2.1 lists mass- or size-distribution exponents given in the literature.

Table 2.1: Exponents of the cumulative fluence on a spacecraft, $\tilde{\gamma}$, the cumulative mass distribution, γ, and the differential size distribution, α, compiled from the literature. **Bold** values are taken directly from the publications, the remaining values were derived assuming the following relations. To translate $\tilde{\gamma}$ to γ, it is assumed that the speeds of small particles are limited by the speed of the gas and therefore independent of size. Hence $\gamma = \tilde{\gamma}$ for small particles (indicated by "†"). For larger particles, the relation $v \propto m^{-1/6}$ is used, which was derived from a radially symmetric coma model (Divine et al., 1986), resulting in $\gamma = \tilde{\gamma} + 1/6$ for large particles (indicated by "$*$"). The relation between the differential size distribution and the cumulative mass distribution is given by $\alpha = -3\gamma - 1$.

Comet	Instrument(s)	Mass/size interval	$\tilde{\gamma}$	γ	α	Reference
6P/d'Arrest	ESO/Schmidt	$> \mu$m			**−4.15**	Sekanina and Schuster (1978)
1P/Halley	DIDSY&PIA	$10^{-13} \ldots 10^{-8}$ kg		**1.02**	−4.06	McDonnell et al. (1987)
		$10^{-8} \ldots 10^{-6}$ kg		**0.71**	−3.13	
	DIDSY&PIA	$10^{-19} \ldots 2\times10^{-14}$ kg	**0.18**	$0.18^{\dagger}$	−1.54	Divine and Newburn (1987)
		$2\times10^{-14} \ldots 10^{-6}$ kg	**0.94**	1.11^{*}	−4.32	
	VeGa 1	$10^{-19} \ldots 10^{-12}$ kg	**0.26**	$0.26^{\dagger}$	−1.78	
		$10^{-12} \ldots 10^{-9}$ kg	**1.19**	1.36^{*}	−5.07	
	VeGa 2	$10^{-19} \ldots 1.6\times10^{-13}$ kg	**0.26**	$0.26^{\dagger}$	−1.78	
		$1.6\times10^{-13} \ldots 10^{-9}$ kg	**0.90**	1.07^{*}	−4.2	
	DIDSY	> 20 μm			**−3.5 ± 0.2**	Fulle et al. (1995)
26P/G–S	DIDSY/GRE	$10^{-9} \ldots 10^{-7}$ kg	$\mathbf{0.27}^{+0.13}_{-0.20}$	0.44^{*}	−2.3	McDonnell et al. (1993)
81P/Wild 2	DFMI	$10^{-14} \ldots 10^{-9}$ kg	**0.85 ± 0.05**	1.02^{*}	−4.05 ± 0.15	Green et al. (2004)
	Stardust Samples	$10^{-17} \ldots 10^{-3}$ kg	**0.57**	0.74^{*}	−3.21	Hörz et al. (2006)
67P/C–G	TNG	mm … cm			**−3.5**	Fulle et al. (2004)
		μm			**−4.5**	
	VLT	$> 10^{-13}$ kg			**−4.1**	Agarwal et al. (2007)

Chapter 3

Comet 67P/Churyumov-Gerasimenko

Comet 67P/Churyumov-Gerasimenko is the primary target of the Rosetta mission of the European Space Agency. The spacecraft was launched in March 2004 and is scheduled to reach the comet in May 2014 at a heliocentric distance of 4 AU. Rosetta will follow 67P/C–G on its way to the inner solar system, deploying a lander with scientific instruments in November 2014 (around 3 AU). The nominal end of the mission is in December 2015, after the perihelion passage of 67P/C–G in August 2015.

In this chapter, published data characterising comet 67P/C–G are summarised. The values given here serve as input to the model described in Chapter 5 and employed in Chapter 6 to constrain the emission of mm- to cm-sized particles by 67P/C–G.

3.1 Discovery and Orbital Evolution

Comet 67P/Churyumov-Gerasimenko is a Jupiter family comet with an orbital period of 6.56 years and the orbital elements listed in Table 3.1. It was discovered in 1969 by K. I. Churyumov and S. I. Gerasimenko. Until 1840, the perihelion distance of the comet was at 4 AU. A close encounter with Jupiter shifted the perihelion distance to 3 AU. The distance decreased to 2.77 AU until 1959, when a second close encounter with Jupiter moved 67P/C–G into its present orbit. The perihelion distance in 2002 was 1.29 AU and will be 1.24 AU in 2015 (Marsden, 1970).

Table 3.1: Orbital elements of comet 67P/C–G for the epoch 23.0 August 2004 in the coordinate system given by the ecliptic and mean equinox of J2000. The values were obtained from JPL (`http://ssd.jpl.nasa.gov/horizons.cgi`).

Semi-major axis (AU)	3.50
Eccentricity	0.63
Inclination (degrees)	7.13
Longitude of ascending node (degrees)	50.92
Argument of perihelion (degrees)	11.37
Time of perihelion passage (UT)	2002 Aug 18.24

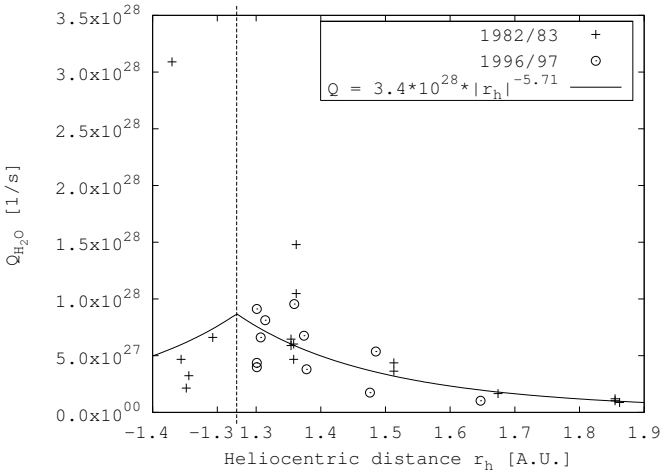

Figure 3.1: H_2O production rate as a function of heliocentric distance, inferred from spectroscopic observations during different apparitions of the comet. The solid line is a power-law fit to the data.

3.2 Nucleus Properties

The effective radius of the nucleus of 67P/C–G is the range of 1.7 to 3.2 km (Mueller, 1992; Lowry et al., 2003; Tancredi et al., 2000; Kelley et al., 2005; Tancredi et al., 2006; Lamy et al., 2006, 2007). Lamy et al. (2006, 2007) expect the nucleus to be an irregular body with axis ratios a/b = 1.26 and a/c = 1.5 to 1.6. They find a nucleus geometric albedo in the R-band between 0.045 and 0.06, a rotational period of 12.4 to 12.7 h, and a bulk density of 370 kg/m^3.

3.3 Gas and Dust Production

The dominant species of gas emitted by comet 67P/C–G are H_2O and CO. Figure 3.1 shows the H_2O production rate inferred from spectroscopic observations as a function of heliocentric distance (Hanner et al., 1985; Feldman et al., 2004; Mäkinen, 2004; Crovisier et al., 2002) and a power-law fit to the data. For the CO-production rate, an upper limit of 10^{27} molecules/s at 3 AU has been derived from radio observations (Bockelée-Morvan et al., 2004). On the basis of the observed gas production rates, the emission speeds of dust particles from the coma, given by Equation 5.48, were derived by means of the hydrodynamic coma model outlined in Appendix C.

$Af\rho$ values for 67P/C–G were measured during the apparitions in 1982/83, 1995/06, and 2002/03 (Storrs et al., 1992; Osip et al., 1992; A'Hearn et al., 1995; Kidger, 2003; Lamy et al., 2003; Weiler et al., 2004; Schulz et al., 2004a; Feldman et al., 2004; Schleicher, 2006)[1]. Figure 3.2 shows $Af\rho$ as a function of the heliocentric distance. Both $Af\rho$ and the H_2O production rate reach their maxima around 30 days after perihelion.

Like for other comets, a dependence of $Af\rho$ on the employed aperture size has been observed for 67/C–G (Schleicher, 2006). This may account for at least part of the considerable scattering of the data shown in Figure 3.2. Beyond 3 AU, the nucleus appeared as a point source in all observations known to the author with two exceptions. Kelley et al.

[1]The data from these publications are summarised in the data base at `http://berlinadmin.dlr.de/Missions/corot/caesp/comet_db.shtml`. The site also includes data obtained by amateur astronomers.

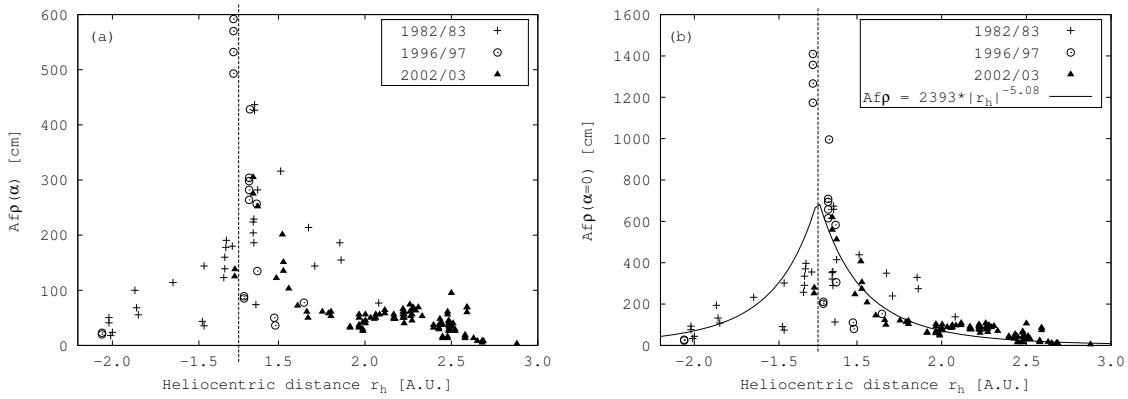

Figure 3.2: $Af\rho$ as a function of heliocentric distance $r_{\rm h}$ for three apparitions of comet 67P/C–G. **a)** Measured values. **b)** Measured values corrected for the phase-angle dependence of $Af\rho$ by division through the geometric phase function shown in Figure 2.1. The solid line is a power-law fit to the data. The increased $Af\rho$-values around $r_{\rm h}$= 2.5 AU in Panel (a) can be attributed to a distinct minimum in phase angle, which is evident from a comparison of Panels (a) and (b): After division by the geometric phase function, the peak is attenuated but still present.

(2006) found that their nucleus brightness measured in July 2004 is incompatible with the nucleus radius of about 2 km obtained by Lamy et al. (2006, 2007). They attribute the excess brightness to either a coma of young particles or a slowly dispersing population of larger particles from the last perihelion passage. C. Tubiana (private communication) observed that in May/June 2006 the brightness profile of the nucleus deviated form that of a point source. From the absence of an observable coma it is generally inferred that the comet is not active.

3.4 Coma Features, Dust Tail, Antitail and Trail

The coma of 67P/C–G displayed distinct azimuthal brightness variations during both the 1996/97 and the 2002/03 apparitions (Schleicher, 2006; Schulz et al., 2004a,b; Weiler et al., 2004). An example image is shown in Figure 3.3. These features have been interpreted as border lines of coma fans produced by active areas at different latitudes on the rotating nucleus (H. Böhnhardt, private communication). Constraints for the orientation of the rotation axis of the nucleus have been derived from the observed coma features by Weiler et al. (2004) and Schleicher (2006).

Between perihelion in August 2002 and at least April 2006, the tail of 67P/C–G was characterised by a thin, bright spike close to the projected comet orbit in the direction trailing the nucleus. Different interpretations of this phenomenon are discussed in Agarwal et al. (2007) with the conclusion that it most probably is a distinct antitail due to the low inclination of the comet orbit with respect to the ecliptic.

The dust trail of 67P/C–G was first observed with IRAS in 1983 (Sykes et al., 1986a,b), having a length of 1.2° in mean anomaly and a width of 50000 km (Sykes and Walker, 1992). The first observation of the 67P/C–G trail in visible light was performed by M. Ishiguro (private communication).

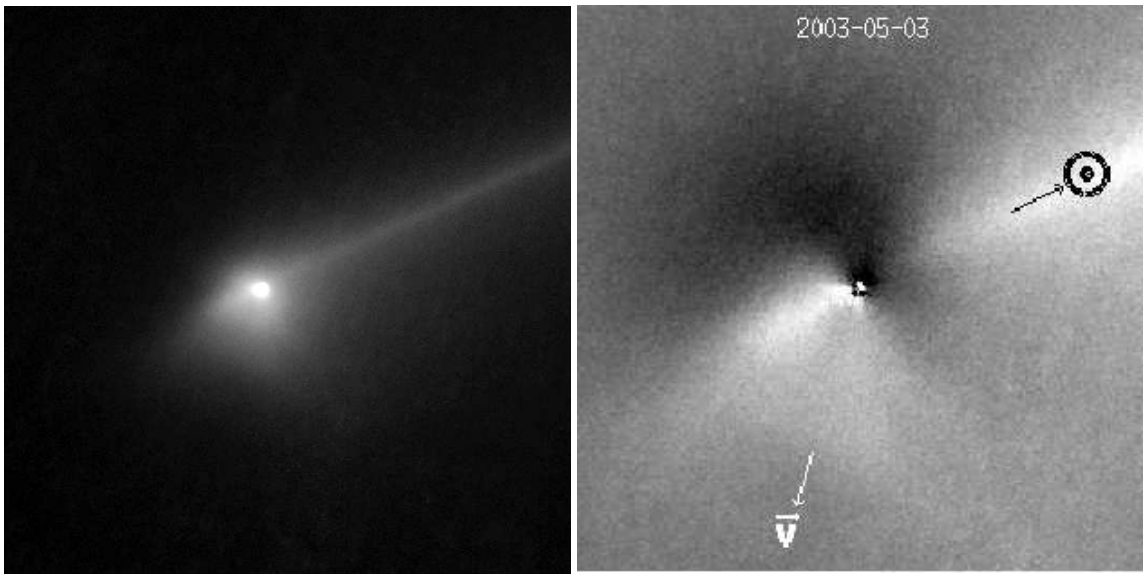

Figure 3.3: Left: Broadband R image of comet 67P/C–G on 3 May 2003 obtained with FORS1 at ESO/VLT/U1 (Schulz et al., 2004a,b). Right: Same image, but structurally enhanced by subtracting the azimuthally averaged coma profile from the measured brightness distribution. Both images are by courtesy of R. Schulz.

Chapter 4

Observations of the 67P/C–G Trail

This work is based on the analysis of three observations of the dust trail of comet 67P/C–G, one in visible light obtained in 2004, and two at mid-infrared wavelengths made in 2005 and 2006. Geometrical parameters of these observations are listed in Table 4.1. In this chapter, the processing applied to each of the data sets is described. Calibrated profiles of the surface brightness in the trail are derived. In Chapter 6, the measurements will be interpreted utilising the trail model described in Chapter 5.

4.1 Optical Observation

4.1.1 Data Acquisition

67P/C–G was observed in April 2004 with the Wide Field Imager (WFI) at the ESO/MPG 2.2m telescope on La Silla (Chile). The total integration time was 7.50 h of which 0.75 h were done on 2 April, the remaining time was split equally over the three consecutive nights of 19 – 21 April.[1] The data set includes 50 images of 540 s exposure time each. To maximise sensitivity, 3×3 on-chip pixel binning was used, resulting in a pixel size of $0.71''$. The camera has eight Charge Coupled Devices (CCDs). Each image is therefore a mosaic of eight frames covering a total FOV of $34'\times33'$. No filter was employed. The data processing was done with IRAF[2].

4.1.2 Processing of Individual Exposures

An exemplary raw-image is shown in Figure 4.1a. The first processing step was to subtract a bias image. The bias is an additive pattern introduced by the readout electronics

[1] Images obtained during additional 2.25 h on 18 April were contaminated by stray light from a star of 4^{th} magnitude close to the instrument field of view. These were not used for the following analysis.

[2] The Image Reduction and Analysis Facility is a general purpose software system for the reduction and analysis of astronomical data. IRAF is written and supported by the IRAF programming group at the National Optical Astronomy Observatories (NOAO) in Tucson, Arizona. NOAO is operated by the Association of Universities for Research in Astronomy (AURA), Inc. under cooperative agreement with the National Science Foundation. Both software and documentation may be obtained from the website `http://iraf.noao.edu/`.

Table 4.1: Geometrical parameters of the three observations of the dust trail of comet 67P/C–G described in Sections 4.1 and 4.2. MA = mean anomaly, PA = position angle. The "solar elongation angle" is the angle between the directions to the Sun and to the comet, seen by the observer. The "orbit plane angle" is the angle between observer and comet orbital plane, measured from the centre of the comet nucleus; positive values indicate that the observer is above the comet orbital plane, in the direction of the orbital momentum vector of the comet. The "viewing angle" is the angle between the line of sight and the comet velocity vector; values $< 90°$ indicate that the comet moves away from the observer. The "neckline emission date" is defined as the date when the comet nucleus was at a true anomaly of $\tau_{\rm obs} - 180°$. With the exception of the orbit section lengths and the viewing angle, all values were obtained from the JPL Horizons System (`http://ssd.jpl.nasa.gov/horizons.cgi`).

Telescope	ESO/MPG 2.2m	Spitzer	Spitzer
Instrument	WFI	MIPS24	MIPS24
Date of observation[†]	2 Apr, 19–21 Apr 2004	28/29 Aug 2005	8/9 Apr 2006
Heliocentric distance	4.69 AU	5.69 AU	5.66 AU
Distance from observer	3.69 AU	5.72 AU	5.36 AU
Nucleus right ascension α	$14^{\rm h}10^{\rm m}38\overset{\rm s}{.}79$	$15^{\rm h}00^{\rm m}50\overset{\rm s}{.}73$	$17^{\rm h}06^{\rm m}46\overset{\rm s}{.}87$
Nucleus declination δ	$-10°13'03\overset{''}{.}6$	$-18°04'54\overset{''}{.}6$	$-24°57'24\overset{''}{.}5$
Nucleus $\mathrm{d}\alpha/\mathrm{d}t \times \cos\delta$	$-26.61''$/h	$8.83''$/h	$1.16''$/h
Nucleus $\mathrm{d}\delta/\mathrm{d}t$	$7.83''$/h	$-3.53''$/h	$-1.49''$/h
Orbit section covered (proj.)	$2'\ldots-33'$	$18'\ldots-28'$	$9'\ldots-33'$
Orbit section covered (MA)	$0.1°\ldots-1.0°$	$1.0°\ldots-1.6°$	$0.5°\ldots-1.7°$
PA of neg. velocity vector	296.9°	293.5°	281.6°
PA of Sun-comet vector	253.1°	106.2°	274.9°
Phase angle	1.0°	10.3°	10.0°
Solar elongation angle	175.3°	83.3°	102.5°
Orbit plane angle	−0.7°	1.3°	−1.2°
Viewing angle	54°	94°	110°
Ecliptic lat. (obs. centred)	2.8°	−0.9°	−2.1°
True anomaly at obs. ($\tau_{\rm obs}$)	150.8°	176.1°	185.9°
Neckline emission date ($t_{\rm nl}$)	15 Jul 2001	14 Aug 2002	25 Aug 2002
$t_{\rm nl}$ relative to perihelion	−34 d	−4 d	+7 d
Heliocentric distance at $t_{\rm nl}$	1.36 AU	1.29 AU	1.29 AU

[†]The values given in this table are for 20 Apr 2004, 29 Aug 2005, and 9 Apr 2006, 00:00:00.0 UT.

of the camera. It is independent of the exposure time and therefore measured by an exposure of 0 s duration and the same on-chip binning factor as the science exposures. To reduce noise, a master-bias was created by median-averaging over ten bias exposures. The master-bias was then subtracted from each science exposure.

The eight CCDs of the WFI are characterised by different gain factors for converting electrons to ADU (Analogue Digital Units). The general recommendation for WFI images (e. g. Erben et al., 2005) is that the removal of the instrumental signature should be

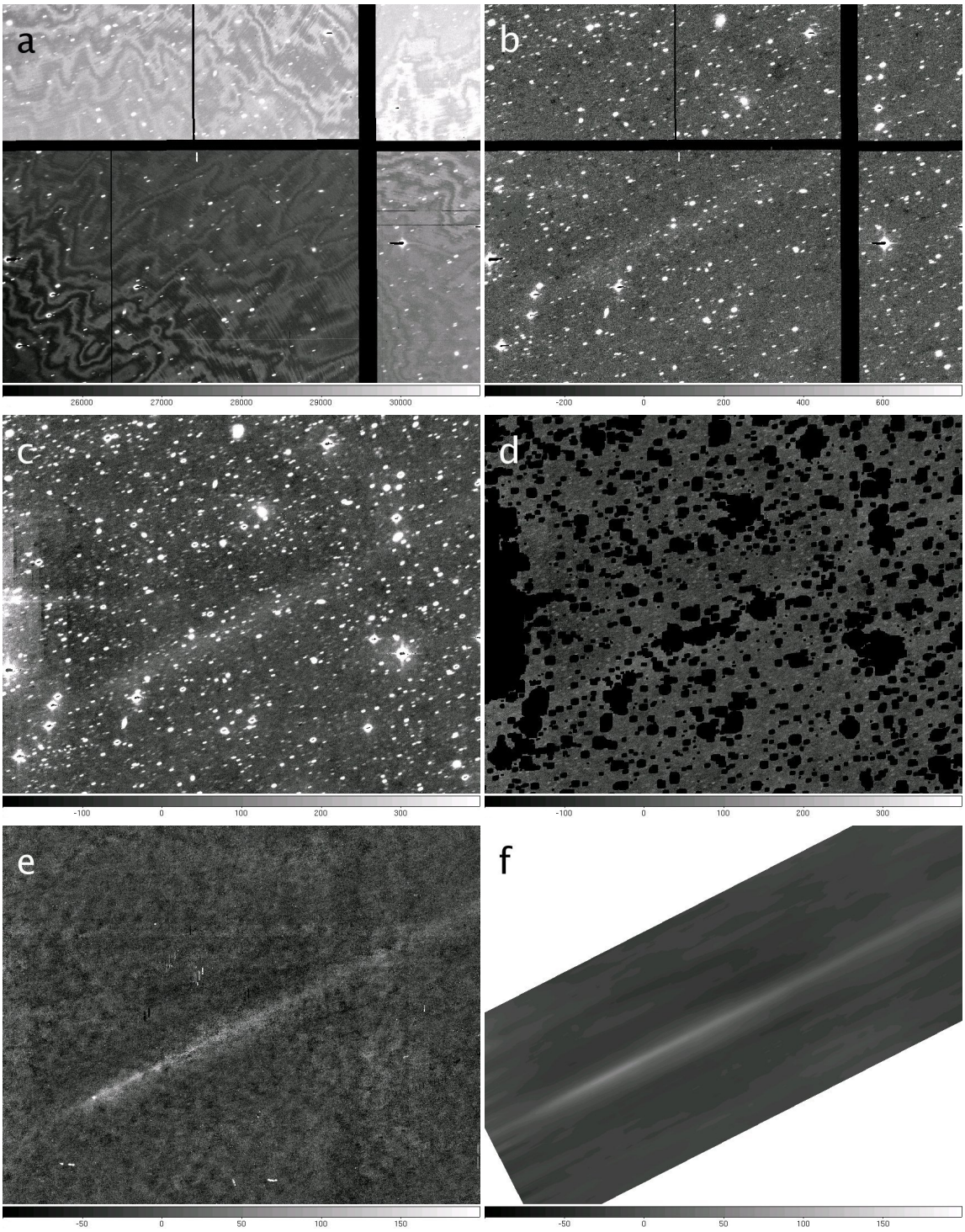

Figure 4.1: Image section of $10' \times 8'$ during successive processing stages. The nucleus is in the lower left quadrant. **a)** Raw image, showing fringing and different CCD gains. **b)** Image after flat-fielding, removal of fringing and gain correction. **c)** Images taken on 19 April average-combined in the rest frame of the stars. **d)** Same image as (c) after object masking. **e)** All images average-combined in the co-moving frame with object masking. **f)** Same image as (e) after removal of nucleus and spatial filtering. Note the different brightness ranges indicated below the images.

done individually for each CCD and the processed images afterwards be combined into a mosaic, adjusting their brightness levels through division by the gain factors of the individual CCDs. For the present data the gain factors given in the WFI Handbook[3] were not sufficiently accurate to ensure uniform sky-level in the resulting mosaic, nor was the attempted derivation of the relative gain from the data. To ensure a uniform background level the mosaics of the eight frames of one exposure were assembled first. Then a single flatfield (see below) was created for the whole mosaic, and the individual mosaics were divided by this flatfield. Since the original images and the flatfield are scaled by the same gain factors, these cancel in the flatfielded image.

The raw images were characterised by strong fringing, an interference artefact arising in blue-optimised thin-layered CCDs when observing in red wavelengths (Erben et al., 2005). While the amplitude of the fringing depends on time, the shape of the pattern is considered stable[4]. The recommended way to remove the fringing pattern is to measure its amplitude in some well defined parts of the image, scale the fringing pattern image (obtainable either from ESO or extracted from the data) accordingly, and subtract the scaled fringing image. The result for the present data set was not satisfactory. The amplitude of the fringing relative to the background level generally became stronger towards morning, possibly because of changing spectral characteristics of the sky. For a limited time interval, however, it was found that the fringing amplitude could be approximated as proportional to the background level. Like the gain correction, the removal of the fringing pattern therefore was included in the flatfielding, which is described in the following.

For flatfielding neither twilight nor dome flatfield exposures were used, because the science images were obtained without filter and the spectral properties of the night sky are different from those of the twilight sky or lamp. Instead, superflats were built from the science data. This was possible because due to jittering, stellar objects were in different positions on the CCDs in successive exposures. To obtain a superflat, the mosaics were normalised through division by their modes[5] and then median-averaged. Bright objects were thus excluded from the combined image while instrument-specific features (including fringing and gain) remained. Many of the images contained highly saturated objects with huge haloes, covering areas that overlap in the different images taken in the same night. These could only have been eliminated by median-averaging over images obtained during different nights. However, the observed time-dependence of the relative fringing amplitude implied that a flatfield obtained from averaging over a larger time interval removed the fringing less completely. Since the haloes are predominantly far from the trail, while the incomplete fringing removal affects the whole image, the emphasis was put on avoiding the latter. An optimally smooth background after flatfielding was achieved by median-combining five consecutive exposures into one superflat (Figure 4.1b).

[3]The Wide-field Imager Handbook, Issue 2.0, was released by the European Southern Observatory as Document No. 2P2-MAN-ESO-90100-0001 on 4 May 2005.

[4]`http://www.ls.eso.org/lasilla/sciops/2p2/E2p2M/WFI/CalPlan/fringing/` and WFI Handbook

[5]In the following, the terms “mean”, “median = midpoint”, and “mode” are used in accordance with their definitions in IRAF: The mean is given by $(\sum_{i=1}^{N} x_i)/N$, where x_i are the values of individual pixels. The midpoint and mode are obtained from interpolation of a histogram of the data. The midpoint is defined as the value with half of the pixels below it and half above. The mode is defined as the maximum of the data histogram.

After flatfielding, the mean sky level – approximated by the image mode – was subtracted from each image. To account for the dependence of the atmospheric absorption on the zenith angle θ of the observed object, the images were corrected for the so-called airmass. The intensity received by the observer is related to the incoming intensity by

$$I_{\rm rec}(\theta) = I_{\rm inc}\, 10^{-K\,X(\theta)/2.5}, \tag{4.1}$$

where $X \approx \sec\theta$ is the airmass, and K is the location-dependent extinction coefficient of the atmosphere. The airmass represents the length of the light path through the atmosphere relative to the one at zenith, hence $X(\theta = 0) = 1$. The intensity measured at airmass X is corrected to some reference airmass X_0 by

$$I_{\rm corr} = I_{\rm rec}(X) 10^{K(X-X_0)/2.5}. \tag{4.2}$$

A mean extinction coefficient for La Silla of K = 0.15 mag/airmass was used.

In the following, the data obtained at this stage will be called the "corrected single images". They were subsequently processed in two different manners in order to, first, obtain the final image of the trail and, second, derive an approximate flux calibration using field stars.

4.1.3 Object Masking and Co-Addition

The final trail image was obtained by averaging over all corrected single images in the rest frame of the comet. Because of the relative motion of the comet and the background objects, the latter appeared in the combined image as short, dashed lines often considerably brighter than the trail. In order to exclude such objects from the averaging procedure, object masking was applied.

To create an objectmask, all images of one night were average-combined in the rest frame of the stars (Figure 4.1c). The nucleus appeared in the resulting image as a dotted line. The signal-to-noise ratio (SNR) of the stars and galaxies was increased by this procedure whereas that of the nucleus was reduced. The object mask for a given night was created with the IRAF routine `objmasks`. It masks all pixels above a given threshold with a sufficient number of neighbours above the same threshold. A lower threshold results in a smoother background of the final mosaic. The lowest possible threshold was given by the condition that the comet nucleus and its bright dust environment must not be masked. The optimal threshold was found to be five times the local mean variance of the sky. Saturated or otherwise bad pixels and the gaps between adjacent CCDs were masked as well.

The mask obtained for the averaged image was subsequently "attached" to each individual exposure. The average-combined image in the rest frame of the comet has a reasonably smooth background, and the trail is easily visible (Figures 4.1e and 4.3a). A histogram of the brightness distribution of the background is shown in Figure 4.2. Fitting a Gaussian to the brightness distribution yields a variance of σ_0 = 34.5 ADU.

However, the low mean SNR precludes a quantitative analysis of this image. SNR can be improved by applying a spatial averaging filter which replaces each pixel by the average of its $m \times n$ neighbours (IRAF routine `boxcar`). By averaging over an area a,

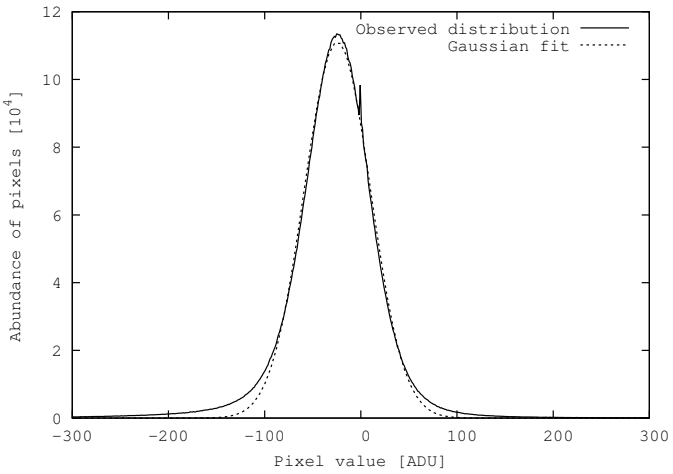

Figure 4.2: Histogram of the image of which Figure 4.1e is a section (solid line). The bin width of the histogram is 1.2 ADU. The dashed line is the result of fitting a Gaussian function, $g(x) = g_0 \exp\left(-(x-x_0)^2/(2\sigma_0^2)\right)$, to the data. The centre of the peak is at x_0 = −24.4 ADU and the variance is σ_0 = 34.5 ADU.

the background noise σ is reduced by the factor $(a/a_0)^{1/2}$, where a_0 is the area of one pixel and $\sigma_0 = \sigma(a_0)$:

$$\sigma(a) = \sigma_0 \sqrt{\frac{a}{a_0}}. \tag{4.3}$$

The price to pay is a loss of spatial resolution. The size of the averaging window should therefore be smaller than the characteristic dimension of the object. Since the trail is very extended in the direction parallel to the orbit while narrow perpendicular to it, a rectangular window much larger in the parallel direction than in the perpendicular one was used.

To properly apply the filter, the image was first rotated by 26.5° clockwise, and the nucleus was replaced by interpolating between the surrounding pixels. A filtering window of 200 pixels (140″) parallel and 10 pixels (7″) perpendicular to the trail axis was used, increasing SNR per pixel by a factor of 45. The resulting image is shown in Fig. 4.3b.

4.1.4 Flux Calibration

Flux calibration was done on the basis of the USNO-B1.0 catalogue (Monet et al., 2003). Like for the derivation of object masks, SNR was increased by averaging over all corrected single images of a given night in the rest frame of the stars. In the combined images, aperture photometry of a set of "solar-type" (definition below) field stars in the FOVs of the images was done. It was assumed that the scattering by cometary dust does not significantly alter the spectral properties of light from the Sun (Section 2.3).

The USNO-B1.0 catalogue contains up to five magnitudes for each object: R1, B1, R2, B2, and I2, where "1" and "2" refer to their origin from POSS1 and POSS2[6] plates, respectively. The standard deviation of the magnitudes given in the catalogue is 0.25 mag (Monet et al., 2003). The 1σ-uncertainty of the difference of two magnitudes is therefore $\sqrt{2}\times$ 0.25 mag = 0.35 mag.

[6]The first Palomar Observatory Sky Survey (POSS1) was conducted on the Oschin Schmidt Telescope at Palomar Observatory (California) in 1950–57 in the red and blue wavelength bands (Minkowski and Abell, 1963). The POSS2 plates were exposed in 1975-2002 in blue, red, and near-infrared on the U.K. Schmidt Telescope at Siding Spring Observatory in Australia for the southern sky and on the Oschin Schmidt Telescope at Palomar for the northern hemisphere (Reid et al., 1991).

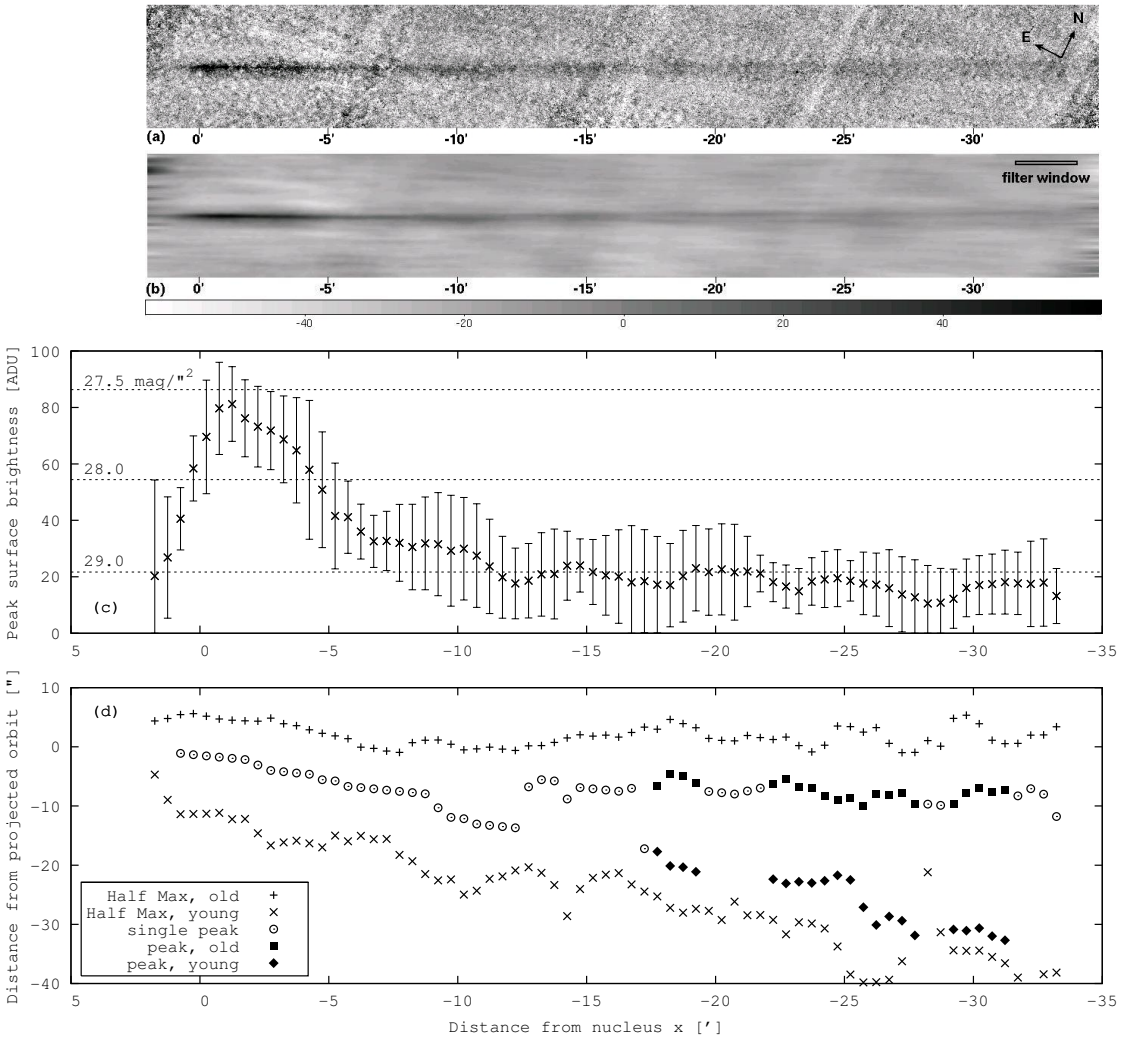

Figure 4.3: WFI image of comet 67P/C–G obtained in April 2004. The image size is $35' \times 4.7'$, the distance from the nucleus is indicated at the lower margins, and the brightness range in ADU is shown by the colourbar below Panel (b). **a)** Unfiltered image rotated by 26.5° clockwise. The inclined stripes are remnants of the overscan regions between individual CCDs (Figure 4.1a). **b)** The same image, after replacing each pixel by the average over a neighbourhood of 200 pixels ($140''$) parallel and 10 pixels ($7''$) perpendicular to the trail axis. The size of the filtering window is indicated in the upper right corner. **c)** Peak surface brightness as a function of distance from the nucleus. The errorbars represent the variation of the background derived for each data point from a profile perpendicular to the orbit (examples in Figure 4.4). The corresponding surface brightness in R-filter (Section 4.1.4) is indicated by dashed lines. The measure profile is too low by 20 to 40% due to the flatfield (Section 4.1.6 and Appendix B). **d)** FWHM of the trail and position of the peak(s) as functions of distance from the nucleus. "+" and "x" show the distances from the orbit where the surface brightness is half of the peak brightness on either side of the nucleus. It was assumed that the projected orbit is inclined against the x-axes in Panels (a) and (b) by an angle of 0.4° (Table 4.1). "+" and "x" indicate the old trail and particles from the last apparition, respectively (see text). Open circles show the peak position when only one peak is observed. Otherwise, squares and diamonds indicate the positions of the peaks attributed to old and young particles, respectively. The "old" particle peak is not aligned with the projected orbit, possibly as a result of inaccurate orientation towards north of the original image.

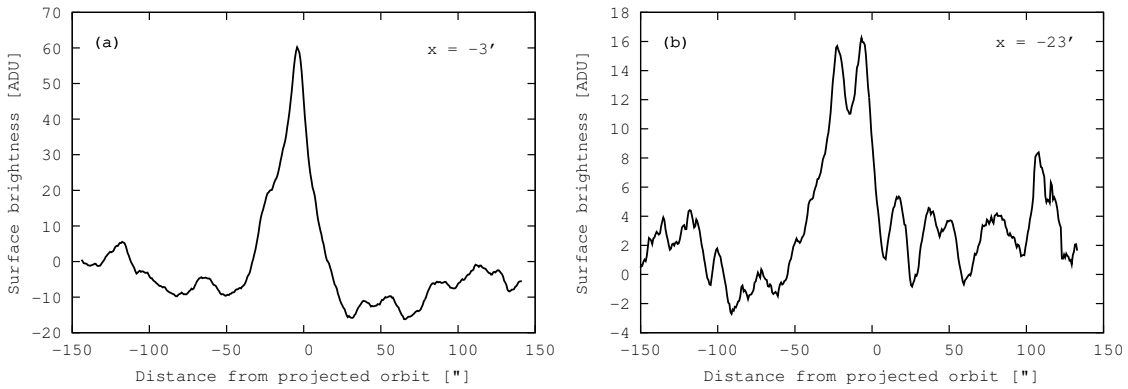

Figure 4.4: Profiles through the image shown in Figure 4.3b perpendicular to the projected orbit. **a)** Profile at a distance of 3′ behind the nucleus. **b)** Profile at 23′ behind the nucleus, showing the splitting of old trail and neckline.

Stars were considered as "solar type" when their B−R, B−I, and R−I filter colours in the USNO-B1.0 catalogue were compatible with the colours of a G2V (i. e. solar-type) star in the Cousins filter system: B−R=1, B−I=1.3, and R−I=0.3 (Fitzgerald, 1970)[7]. Therefrom the following selection criteria are derived:

$$\begin{aligned} 0.65 &< \text{B1}-\text{R1} < 1.35\,, \\ 0.65 &< \text{B2}-\text{R2} < 1.35\,, \\ 0.95 &< \text{B2}-\text{I2} < 1.65\,, \\ -0.05 &< \text{R2}-\text{I2} < 0.65\,. \end{aligned}$$

A star was considered to be of "solar type" if at least three of these criteria were satisfied. Only stars with R-magnitudes fainter than 17.7 could be used, because brighter ones were saturated in the raw data. The sets of suitable stars consisted of 18, 35, 34, and 14 stars for the first, second, third, and fourth night, respectively. During the first and the fourth night, more stars were saturated because of a higher mean sky flux.

For the selected stars, j, the integral flux I_j (in ADU) in the combined image (Figure 4.1c) was measured using the IRAF routine `imexam`. To this purpose, the flux I_c from a circular aperture of radius r around the star was measured, where r was three times the Full-Width Half-Maximum (FWHM) of the star. To assess the backgound contribution, the flux I_a from a circular annulus of width d_a around the object was calculated. The inner edge of the annulus was separated from the circle by a specified buffer distance d_b. After scaling to the same area, the flux from the annulus was subtracted from the flux measured in the circular aperture, giving the flux from the object:

$$I = I_\mathrm{c} - \frac{A_\mathrm{c}}{A_\mathrm{a}} I_\mathrm{a}, \tag{4.4}$$

where A_c and A_a are the areas of the circle and the annulus, respectively. The mean aperture radius used by IRAF was r = 9 pixels with a variance of 2 pixels, and d_a = d_b = 3 pixels, corresponding to A_c = A_a = 254 pixels.

[7] Summarised at `http://www-int.stsci.edu/~inr/intrins.html`

By plotting the catalogue R-magnitude $M_{\rm cat}(j)$ versus $-2.5\,\log_{10}(I_j)$ and fitting a linear relation

$$M_{\rm cat}(j) = M_0 - 2.5\log_{10}(I_j) \tag{4.5}$$

to the data, the calibration offset M_0 was deduced. This procedure was exercised independently for the four nights and for the two R-magnitudes given in the catalogue. The derived values of M_0 were consistent within the regression errors with one exception, so for further calculations the value derived from the largest possible sample of data, M_0 = (32.34 $\pm$ 0.02) mag, was used (Figure 4.5). The stars used for calibration are listed in Appendix A. The R-magnitude of an object of flux $I_{\rm obj}$, measured in ADU is then given by

$$M_{\rm obj}(j) = M_0 - 2.5\log_{10}\,(I_{\rm obj}). \tag{4.6}$$

The surface brightness of an extended object is obtained by using the flux from one arcsec^2 as $I_{\rm obj}$.

Calibrating an observation done without filter in the R-band, is justified as long as the spectral properties of object and calibration stars are the same. Then the fluxes measured with and without filter are different by a constant factor. The corresponding magnitudes are different by an additive constant that is included in the calibration magnitude M_0.

For comparison with simulated images, the R-magnitude must be translated into flux

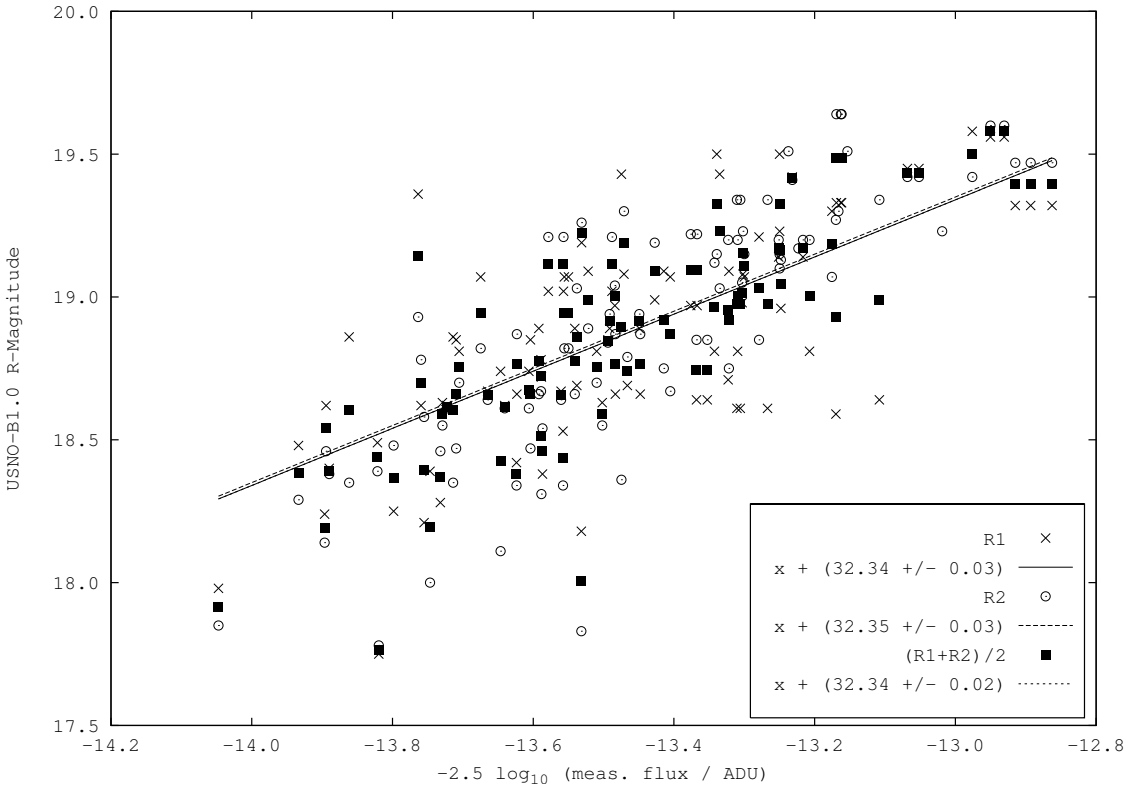

Figure 4.5: R-magnitudes from the USNO-B1.0 catalogue versus magnitudes measured in the images, expressed as $-2.5\,\log_{10}(I)$, where I is the total flux from the object in ADU. The lines are linear fits to the data for R1 and R2 separately and for their mean value.

per unit solid angle. This is achieved by assuming that the apparent R-magnitude of the Sun $M_{\rm sun}$ = −27.14 mag corresponds to a flux of $I_\odot^{\rm SI}$ = 1367 W/m^2 measured without filter and outside the atmosphere. The superscript "SI" indicates that the quantity is measured W/m^2 instead of ADU. The flux in ADU corresponding to $M_{\rm sun}$ is $I_{\rm sun} = \exp[(M_0 - M_{\rm sun})/2.5] = 6.19 \times 10^{23}$ ADU. Therefrom follows the conversion factor

$$c = \frac{I_\odot^{\rm SI}}{I_{\rm sun}} = 2.21 \times 10^{-21}\,{\rm Wm^{-2}ADU^{-1}}. \tag{4.7}$$

The obtained flux is the one that would have been measured outside the atmosphere.

4.1.5 Calibration Accuracy

In this section, the uncertainty of the calibration magnitude M_0 is investigated in some more detail. From Equation 4.5 follows

$$\Delta M_0 = \Delta M_{\rm cat} + \Delta M_{\rm meas}, \tag{4.8}$$

with

$$\Delta M_{\rm meas} = \Delta[2.5\log_{10}(I)] = \frac{2.5}{\ln 10}\frac{d}{dI}\ln(I)\Delta I = \frac{2.5}{\ln 10}\frac{\Delta I}{I} = 1.1\frac{\Delta I}{I}. \tag{4.9}$$

$\Delta M_{\rm cat}$ = 0.25 mag is given from the accuracy of the USNO catalogue. ΔI is assessed from the procedure of aperture photometry. From Equation 4.4 follows

$$\Delta I = \Delta I_{\rm c} + \frac{A_{\rm c}}{A_{\rm a}}\Delta I_{\rm a}. \tag{4.10}$$

$\Delta I_{\rm a}$ and $\Delta I_{\rm c}$ are estimated from the background noise. The noise level in a single exposure is given by the variance σ_0 of the Gaussian fitted to the background pixel distribution. Referring to Fig. 4.2, which shows the variance for an image combined of 50 single exposures to be σ = 34.5 ADU, it is deduced that the variance in a single image was $\sigma_0 = \sqrt{50-1}\times 34.5$ ADU = 241.5 ADU. An image combined of 15 exposures – like those on which the aperture photometry was performed – then has a background variance of $\sigma^{15} = \sigma_0/\sqrt{14}$ = 64.5 ADU. A sum over A pixels has an uncertainty of $\Delta I = \sqrt{A}\sigma^{15}$. For a single calibration star

$$\begin{aligned}\Delta I &= \sqrt{A_{\rm c}}\,\sigma^{15} + \frac{A_{\rm c}}{A_{\rm a}}\sqrt{A_{\rm a}}\,\sigma^{15} \\ &= \sigma^{15}(\sqrt{A_{\rm c}} + \frac{A_{\rm c}}{\sqrt{A_{\rm a}}}).\end{aligned}$$

With $A_{\rm c} = A_{\rm a}$ = 254 pixels follows ΔI = 2058 ADU. A representative measured magnitude of $-2.5\,\log_{10}(I) = -13.4$ (Fig. 4.5) corresponds to a flux of I = 230 000 ADU. Insertion in Equation 4.9 gives $\Delta M_{\rm meas}$ = 0.01 mag for a single star, which is negligible compared to the uncertainty of the catalogue values $\Delta M_{\rm cat}$ = 0.25 mag. Since the procedure was applied to a sample of about 200 objects, the final uncertainty reduces

to $\Delta M_0 = \sqrt{200}$ 0.26 mag = 0.02 mag, which is consistent with the uncertainty obtained from the linear regression in Fig. 4.5.

An additional source of error may be the high exposure levels of the calibration stars, suggesting that the relation between flux and count level (in ADU) may not have been entirely linear. The maximum deviation from linearity is about 1% for high exposure levels (WFI Handbook). The maximum calibration error arising therefrom is estimated as follows. Assuming that the measured flux $I_{\rm mes}$ (in ADU) of a calibration star was underestimated by 1%, the true flux would have been $I_{\rm true} = 1.01\ I_{\rm mes}$. The true calibration magnitude would have been $M_0^{\rm true} = M_0^{\rm meas} + 2.5 \log_{10}(1.01) = M_0^{\rm mes} + 0.01$ mag. Since the trail was fainter than the calibration stars, it was far from saturation and not affected by the nonlinearity of the CCD. Therefore the trail brightness derived from the uncorrected calibration star fluxes would be too bright by 0.01 mag.

Figure 4.3 c shows that the statistical uncertainty of the calibration is negligible compared with the uncertainty arising from the background variation, which is on the order of $\pm$20 ADU, and with the systematic error addressed in the following section and in Appendix B.

4.1.6 Error Introduced by Flatfield

Figure 4.3 c shows that the surface brightness of the trail was much lower than the statistical variation of the background σ = 34.5 ADU. The superflats were constructed by median-averaging over five consecutively taken exposures. The purpose of the median-averaging was to remove bright objects from the flatfield. In each exposure, a given object was located at a different position on the CCD, and a given pixel in five consecutive exposures contained a specified object at maximum once. The pixel containing the object was discarded by the median filter, and the resulting image was free of bright objects.

This method fails if the object is less bright than the statistical fluctuation of the background. The object-containing pixel will then not be systematically brighter than the other four, resulting in a non-vanishing probability that the median of the five pixels will be the value of the pixel bearing the object. For a very faint object, the chances of having it in the median pixel approach 20%, which is the probability for one out of five identically distributed pixels to assume the median value. This means that up to 20% of the pixels in the concerned regions of the superflat must be expected to bear trail information. This information is lost from the original image on division by the superflat, and the resulting surface brightness will be approximately 20% too low on average. Because of the employed jittering pattern, there is some overlap of the trail positions in different images, resulting in an expected loss of surface brightness of up to 40%.

For a quantitative comparison with simulated images, the details of the flatfielding process will be included into the simulation (Appendix B). The simulated image then is expected to contain the same artefacts as the WFI. An accurate estimate of the loss can only be given for a specific *original* image. In Appendix B, the loss is estimated for a simulated image that after flatfielding matches the observed image well. Comparison of the originally simulated image and the image after flatfielding and spatial filtering shows that both processes in combination lead to losses in surface brightness of 20% to 40%, where most of the loss is attributable to the flatfielding.

4.1.7 Summary of Optical Observation

The length of the orbit section covered is 35′, corresponding to 1.1° in mean anomaly. Fig. 4.3 c shows an intensity profile along the trail axis, characterised by a distinct peak around the nucleus and a rather uniform brightness distribution beyond 5′ from the nucleus. The measured surface brightness in R-filter is 27.6 ± 0.3 mag near the nucleus and 29.0 ± 0.5 mag at nucleus distances exceeding 10′. These values are expected to be too low by 20% to 40% due to a systematic error.

Taking a closer look at the filtered image displayed in Figure 4.3b, a splitting of the trail is seen beyond 17′ from the nucleus. The gap between the two branches widens with increasing distance from the nucleus (Figure 4.3d). It was ascertained that the splitting does not result from combining images taken in different nights: It remained when only data acquired in a single night were used. A possible change of the orientation of the CCD during a night would have been noticed when combining images with offsets to match stars. The predicted position angle of the trail did not change significantly over the period of observation, either. Hence the splitting is most likely real. Figure 4.3d shows the positions of the two peaks as function of the distance from the nucleus. The average enclosed angle is $0.8° \pm 0.2°$. In Section 4.3 and in Chapter 6, the lower and upper branches will be interpreted as due to particles emitted during the last apparition of the comet (2002/03) and during previous apparitions, respectively.

The “old” particle trail in Figure 4.3d is not aligned with the projected orbit, which is contrary expectations (Chapter 6). The reason for the mis-alignment is probably that no astrometric correction was done for the images. Hence neither the orientation towards north was optimised nor were distortions removed from the FOV. The relative angle between old and young trail should, however, not be significantly affected by this.

4.2 Infrared Observations

Two mid-infrared observations of comet 67P/C–G and its projected orbit at 24 μm were carried out with the Multiband Imaging Photometer (MIPS; Rieke et al., 2004) on board the Spitzer Space Telescope[8] (Werner et al., 2004) in August 2005 and April 2006. The heliocentric distance of the comet was 5.7 AU during both observations, once before and once after its aphelion passage on 25 November 2005. In the following, properties of the data acquisition and processing that are common to both observations are described, including a summary of the software packages used. Then the data reduction steps are described that were individual to either of the two observations, the difference mainly arising from the fact that for the 2006 data a shadow observation was available while for the 2005 it was not.

4.2.1 Data Acquisition and Basic Processing

Each observation was implemented as a cluster in photometry mode. A set of neighbouring pointing positions along the trail was specified. For each pointing position, a sequence of exposures (*Data Collection Events* or DCEs) was taken at eight scan mirror positions and repeated with a small offset of the spacecraft. Around each pointing position, the total field of view covered was $8.25' \times 8.25'$, while a single DCE covered about $5.25' \times 5.25'$. The directions of the scan mirror and spacecraft motions were perpendicular. The first DCE at each spacecraft position had a shorter exposure time and was depressed in response. These images were not used for further analyses, leaving 14 valid exposures at each pointing position.

From each exposure, two images were down-linked from the telescope: the *first difference* image, corresponding to an exposure of about 0.5 s, and the *slope* image, representing the flux averaged over the entire exposure time. The images were flatfielded and calibrated in units of MJy/sr by an automated pipeline at the Spitzer Science Center (SSC). A *Basic Calibrated Data* (BCD) image generated by the SSC pipeline is normally derived from the slope image. If, however, a pixel in the slope image is close to saturation, its value is replaced by that in the first difference image. Thereby more reliable flux data for bright sources are obtained. The flatfielded and calibrated slope and first difference images are also available from the SSC. The calibrated slope images from 2005 and the BCD images from 2006 serve as basis for the further processing and eventual mosaicking described in Sections 4.2.3 and 4.2.4.

To better separate the cometary signal from the background interstellar medium, and – to a limited extent – also from stars and galaxies, a shadow observation was carried out for each observation. A shadow is an exact repetition of the primary (with the same exposure times, pointing coordinates etc.) at a later time, after the comet has left the field of view. By subtracting the shadow from the primary, information on the moving targets in both images is gained. For technical reasons, the shadow observation for the 2005 image was not done before April 2007 and could not be evaluated in this thesis. The 2005 data in the form presented here are therefore of inferior quality compared with the 2006 data, for

[8]The Spitzer Space Telescope is operated by the Jet Propulsion Laboratory, California Institute of Technology under a contract with NASA.

which the shadow was taken a week after the primary observation.

After the processing and mosaicking described in Sections 4.2.3 and 4.2.4, the brightness profile along the trail in each mosaic was obtained from evaluation of perpendicular profiles analysed at different distances from the nucleus, giving the trail width and brightness as a function of distance from the nucleus.

The obtained surface brightness needs to be colour-corrected to account for the slope of the spectrum of dust within the spectral band of MIPS at 24 μm. The flux has been calibrated relative to calibrator stars having a different spectrum from the dust in this image. To derive the true monochromatic flux density at the weighted average wavelength, λ = 23.675 μm, the measured values are divided by a colour correction factor that depends on the dust spectrum. Assuming a geometric albedo of 4% in the entire visible wavelength range and an absorption efficiency of 1 in the infrared (Section 2.5). The equilibrium temperature at $r_{\rm h}$= 5.7 AU is T = 111 K (Equation 2.14). The colour correction factor for a blackbody spectrum of this temperature is 0.947 (MIPS Data Handbook).

4.2.2 Employed Software and Documentation

Documentation concerning the telescope, its instruments and data products is available from the website of the SSC[9] and includes the Spitzer Observer's Manual, Version 7.1, issued on 8 December 2006 and the MIPS Data Handbook, Version 3.2.1, issued on 6 February 2006. From the same source, software packages for the planning of observations and data analysis are available.

The *Spitzer Planning Observations Tool* (SPOT) 16.0 is described in the respective User's Guide issued on 11 April 2007. Apart from planning an observation and creating the required Astronomical Observation Request (AOR), SPOT also includes an option to predict the background contributions by zodiacal light, interstellar medium, and cosmic infrared background for a given area of the sky and observation date. The underlying model is based on data obtained with IRAS and with the *Cosmic Background Explorer* (COBE) and takes into account the dependence of the zodiacal light background on the position of the telescope.

The *Mosaicking and Point Source Extraction* (MOPEX) software (Makovoz and Khan, 2005) is used to interpolate images to a common grid (either celestial or co-moving for a solar system object). Outliers are detected, such as hits of cosmic rays and galactic protons and objects that move with respect to the specified reference frame. The latter works only if the rate of motion of an object is high enough that it is in less than a given fraction of the images at the same sky position. If images are combined in the co-moving frame of the comet, stars should be detected by MOPEX as "moving objects". In the two data sets discussed in the following sections, however, the relative motion of comet and stars was not sufficient to detect stars as moving objects (Table 4.1). The interpolated images are combined by MOPEX into a single mosaic. Point sources in the field of view are detected by help of the APEX *Spitzer Astronomical Point Source EXtraction* software, which can also be used to generate residual (point-source subtracted) images.

The tool ISPY[10] is an interface to the JPL database of small solar system bodies that

[9] `http://ssc.spitzer.caltech.edu`

[10] `http://ssd.jpl.nasa.gov/x/fov.html`

serves to identify such objects in a specified field of view. The objects are detected in a two-step procedure. First, for all objects in the database it is estimated whether or not they are expected in the field of view from their orbital elements. Then the precise positions of the selected objects are computed taking into account planetary perturbations. If the orbital elements of an object are subject to sufficient variability, this object will not be identified in the first step. Hence, an observed moving object may well be included in the database although it was not identified by ISPY. An example is comet 67P/C–G, which was not identified when running ISPY for the parameters of the 2006 Spitzer observation (Section 4.2.4).

4.2.3 Observation in August 2005

During the observation carried out on 28-29 August 2005, 67P/C–G was at a heliocentric distance of 5.69 AU and at a distance from Spitzer of 5.72 AU. The comet orbit was mapped on a length of 46′ projected to the image plane, of which 28′ were in the direction trailing the nucleus. The set of evaluated data consists of 252 images of 30 s exposure time and each covering a field of view of $5.25' \times 5.25'$. Nine pointing positions were specified along the comet orbit, each of which was covered twice, going from east to west and back again. The offsets between the pointing positions were chosen such that each section of the orbit – unless close to the edges of the covered area – was exposed at least 28 times, corresponding to 14 minutes in total. In the overlap areas between adjacent spacecraft positions, a coverage of 42 exposures (21 minutes) was achieved. The images used in the following were processed with version 14.4.0 of the MIPS pipeline.

Saturation of Slope Images

Because of the long exposure time and the bright background, the slope images (Figure 4.6b) were close to saturation. A considerable fraction of the pixels in the BCD images generated by the automated pipeline had therefore been derived from the first difference images (Figure 4.6a). The result corresponded to images of 0.5 s exposure time instead of 30 s with accordingly higher noise level. Since the cometary emission is very faint, the low SNR first difference images were not suitable for its analysis. However, most of the pixels in the slope images were not hard saturated. As part of the calibration pipeline, the images were also corrected for the nonlinearity of the CCD response at high exposure levels. Therefore the basic calibrated slope images were used for the following evaluation.

Bias Image and Zodiacal Light

The slope images were characterised by (1) a brightness gradient roughly from south-west to north-east, and (2) by a more intricate pattern of brightness variation that was common to all images (Figure 4.6b). The amplitude of the pattern (2) diminished for increasing DCE number. Reach et al. (2007) remove both artifacts by subtracting a bias image from each exposure, obtained by median-averaging over all exposures of a given DCE number. For the present data set, the different background levels in exposures of the same DCE

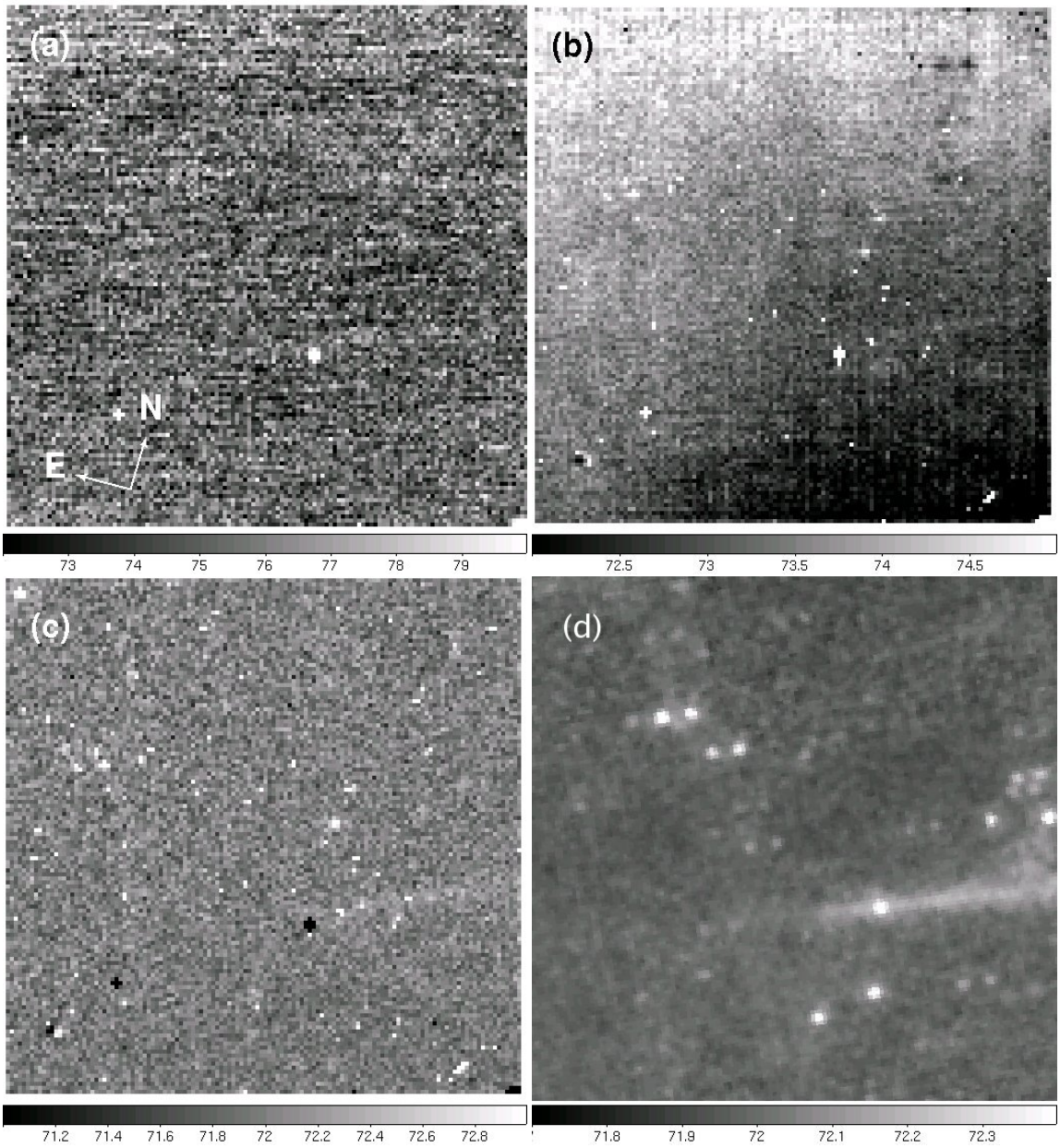

Figure 4.6: Processing stages for a single exposure of the Spitzer 2005 data. The size of the displayed FOV is $5.25' \times 5.25'$. The ranges of surface brightness in MJy/sr are indicated by the colourbars below the images. The nucleus is in the lower right quadrant. **a)** BCD image with most pixels derived from the first difference image and therefore corresponding to an exposure of 0.5 s. **b)** Slope image, corresponding to the full 30 s exposure time. **c)** Slope image after subtraction of the scan-mirror-position dependent gradient and bias image. **d)** Mosaic of all images (corresponding to an exposure time of 14 minutes) in the rest frame of the comet after interpolation to a common grid and outlier rejection.

number precluded the generation of a median image in one step. To nevertheless apply the technique recommended by Reach et al. (2007) there were two possible ways. Either, a constant representing the average background of an image (i. e. the mode or median)

could have been subtracted from each image and the bias images subsequently obtained as recommended by Reach et al. (2007). The alternative was to approximate the surface $f(x, y)$ corresponding to the gradient (1) in an appropriate way and subtract it from each image before extracting the the pattern (2) as the median image of all exposures of a given DCE number. If the gradient (1) is constant, both methods are equivalent. Otherwise, the surface $f(x, y)$ must be approximated by a higher order function. Since the nature of the surface was not a priori known, the second method was adopted. Thereby the direction and possible spatial variation of the gradient could be examined and conclusions be drawn regarding its origin.

The surface $f(x, y)$ was obtained by least-squares fitting the midpoint m_i of each image as a function of the pointing coordinates (x_i, y_i) in decimal degrees, assuming that the pattern (2) affects all derived median values in the same way. For a bi-linear function

$$f(x, y) = ax + by + c \tag{4.11}$$

the parameter values obtained by the least-squares fit are a = (3.22 $\pm$ 0.06) MJy/sr/$^\circ$, b = (11.23 $\pm$ 0.14) MJy/sr/$^\circ$, and c = ($-$450 $\pm$ 10) MJy/sr. The root mean square of the residuals

$$\Delta m_{\mathrm{rms}} = \sqrt{\frac{1}{N}\sum_i (m_i - f(x_i, y_i))^2} \tag{4.12}$$

is Δm_{rms} = 0.48 MJy/sr. Fitting a second-order polynomial surface, the achieved root mean square of the residuals (Δm_{rms} = 0.43 MJy/sr) was on the same order of magnitude as that obtained by the linear fit. Therefore the approximation by the plane surface given in Equation 4.11 was adopted. Since both the pattern (2) and the flux from the trail are additive, the value of the constant c is of no consequence to the results. It was chosen such that the average flux in the images remained unchanged by the subtraction of the surface, i. e. $c = -522$.

The gradient to the surface $f(x, y)$ is given by the vector $(\partial f/\partial x,\, \partial f/\partial y) = (a, b)$, which points to north-east with an azimuthal angle of $\arctan(a/b)$ = 16.0° $\pm$ 0.5° measured counterclockwise from north in the geocentric equatorial system. The magnitude of the gradient is given by $\sqrt{a^2 + b^2}$ = 11.7 MJy/sr/$^\circ$. The direction of the gradient is roughly perpendicular to lines of constant ecliptic latitude and parallel to the scan direction of the telescope. This indicates that the gradient (1) may primarily be an instrumental effect correlated with the position of the scan mirror. According to the MIPS Data Handbook, such gradients are systematically seen in MIPS data and are attributed to changes in the light scattered into the camera as a function of the scan mirror position.

However, a correlation between the image median and the pointing coordinates is also observed when considering only images taken at the same scan mirror position (characterised by the same DCE number). The brightness increases by about 0.8 MJy/sr from the easternmost to the westernmost images. This correlates well in amplitude and direction with the zodiacal light background predicted by SPOT. The contribution of the interstellar medium to the background is predicted to be fainter by an order of magnitude. The magnitude of the zodiacal light variation in turn is an order of magnitude smaller than the gradient attributed to the scan mirror motion. Since the brightness variations due to

the zodiacal light and to the scan mirror position could both be approximated as plane surfaces[11], their sum was represented by the surface $f(x, y)$.

After subtraction of the surface from the individual exposures, the pattern (2) was extracted separately for each scan mirror position by median-averaging images of the corresponding DCE number. Only exposures to the east of the comet nucleus were used in order to avoid the inclusion of trail information into the bias images (Section 4.1.6). The trail east (moving ahead) of the nucleus is below the detection limit. One of the seven bias images was eventually subtracted from each individual exposure.

Interpolation and Co-Addition

The bias-subtracted images (Figure 4.6c) were shifted to the rest frame of the comet according to the JPL ephemeris of 67P/C–G[12]. The shifted images were interpolated to a common grid using MOPEX with outlier rejection to remove artefacts due to cosmic rays and galactic protons. The interpolated images were average-combined with IRAF (Figure 4.6d). The resulting mosaic and the derived peak surface brightness and trail FWHM as functions of the nucleus distance are shown in Figure 4.7[13].

[11]The zodiacal light component is time-dependent because of the motion of the spacecraft. The predicted change of the zodiacal light between the beginning of the first and the end of the second scan leg is 0.15 MJy/sr. Therefore it would have been more accurate to subtract the model zodiacal light component as function of time. The time-dependence of the zodiacal light will also have to be taken into account when evaluating the shadow, which was obtained from a different position on the orbit of Spitzer.

[12]`http://ssd.jpl.nasa.gov/horizons.cgi`

[13]Since no shadow was available, it was attempted to remove background point sources from the image enabling a clearer detection of the trail profile. Object masking as applied to the optical data (Section 4.1.3) could not be used because of the small relative motion of comet and stars and because of the short interval during which the observations were taken. Particularly in the western part of the image, stars appeared as single sources also in the co-moving frame. Instead, the software APEX was used to detect and subtract point sources. It was found that the density of detected point sources was less on the trail than in the rest of the image. The residual image would have been biased and the trail brightness been overestimated. The further analysis was therefore done for the image containing all point sources.

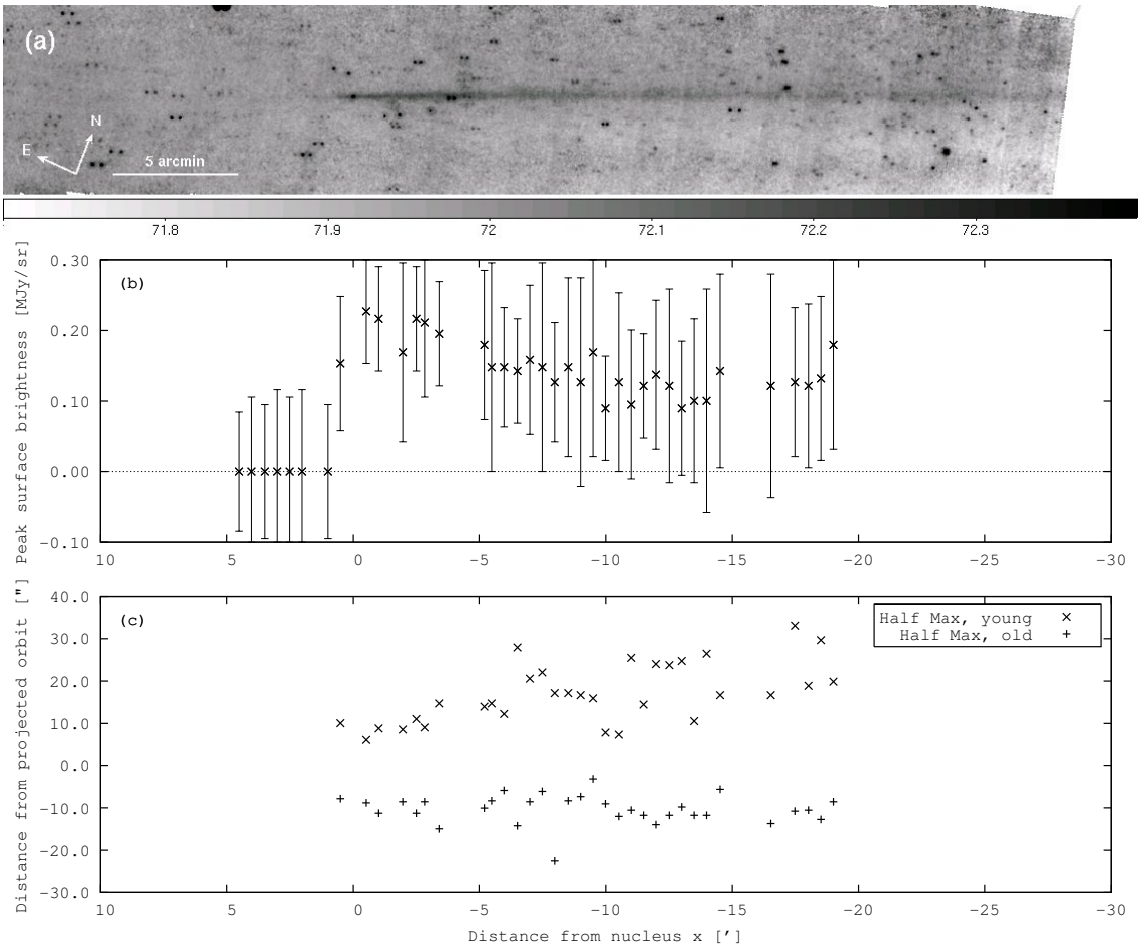

Figure 4.7: a) Mosaic of the images taken on 28-29 August 2005 with MIPS at 24 μm. The surface brightness is in MJy/sr. **b)** Colour-corrected peak surface brightness along the projected orbit as a function of distance from the nucleus, derived from the mosaic (a) after 3x3-boxcar-smoothing. The error bars were derived from the estimated variation of the background. **c)** FWHM of the trail as a function of distance from the nucleus, measured in the mosaic (a) after 3x3-boxcar-smoothing. Shown is the distance from the projected orbit where the surface brightness is half of the peak brightness. The data points in Panels (b) and (c) were derived from perpendicular profiles analogous to those shown in Figure 4.4. The positions of the evaluated perpendicular profiles were chosen in order to avoid bright objects in the mosaic (a). Beyond 20′ from the nucleus, the trail is visible in the mosaic (a), but the low SNR precluded a clear distinction between the trail and other sources in the perpendicular profiles. Values from this region are not shown in Panels (b) and (c), and they are not taken into account for the interpretation of the data in Chapter 6.

4.2.4 Observation in April 2006

The second mid-infrared observation of the 67P/C–G trail took place on 8-9 April 2006, at 5.66 AU from the Sun and 5.26 AU from Spitzer. A shadow observation of the same region of the sky and with the same instrumental settings followed on 14-15 April 2006. The projected length of the covered orbit section is 42′, of which 33′ in the trailing direction. Eight pointing positions were specified, going three times from east to west and back. The four eastern pointing positions were covered only five times. The resulting data set consists of 672 images of 10 s exposure time and a field of view of $5.25' \times 5.25'$. The total exposure time for a given area of sky along the orbit varies between 9.8 and 19.8 minutes.

Because of the – in comparison with the 2005 observation – shorter exposure time of the individual frames and the lower background flux, the slope images were not saturated and served as bases for the BCD images. For further processing, the BCD images produced from Version 13.2.0 of the MIPS pipeline were used.

Co-Addition and Shadow Subtraction

The BCD images were interpolated to a common grid in the moving frame of the comet and average-combined rejecting cosmic ray hits and bad pixels. No background subtraction was applied to the 2006 data. Instead, the shadow images were treated in exactly the same manner, and the resulting mosaic was subtracted from the primary (Figure 4.8).

Because of the small motion of the comet relative to background stars during the three hours' interval covered by the observation, stars appear also in the moving-frame as slightly smeared out point sources. Not all fixed objects were completely removed by the shadow subtraction because of imperfect matching of the frames. These objects appear half white and half black in the difference image.

The average background brightness in the primary is higher than in the shadow because of the changing zodiacal light contribution due to the motion of the telescope. The change in zodiacal light brightness between primary and shadow predicted by SPOT is 3.23 MJy/sr, which is compatible with the measured value given by the average surface brightness of the background in Figure 4.8d. The peak surface brightness and width of the trail are shown in Figure 4.9.

Moving Objects

Sources that are not at all affected by the subtraction are moving targets. They appear either black or white in the difference image (Figure 4.8c), depending on whether they are present in the primary or in the shadow. Some of the moving objects are highlighted in Figure 4.8c and discussed in the following.

Due to the scanning sequence, moving objects appear differently in different parts of the mosaic, according to the time intervals between the exposure sequences taken at a given sky position. The western edge of the FOV was covered by three pairs of closely following exposure sequences with a longer time interval between the pairs. Moving targets in this section of the FOV appear as three equidistant point sources. In the central part of the FOV, the six exposure sequences were carried out with roughly constant time

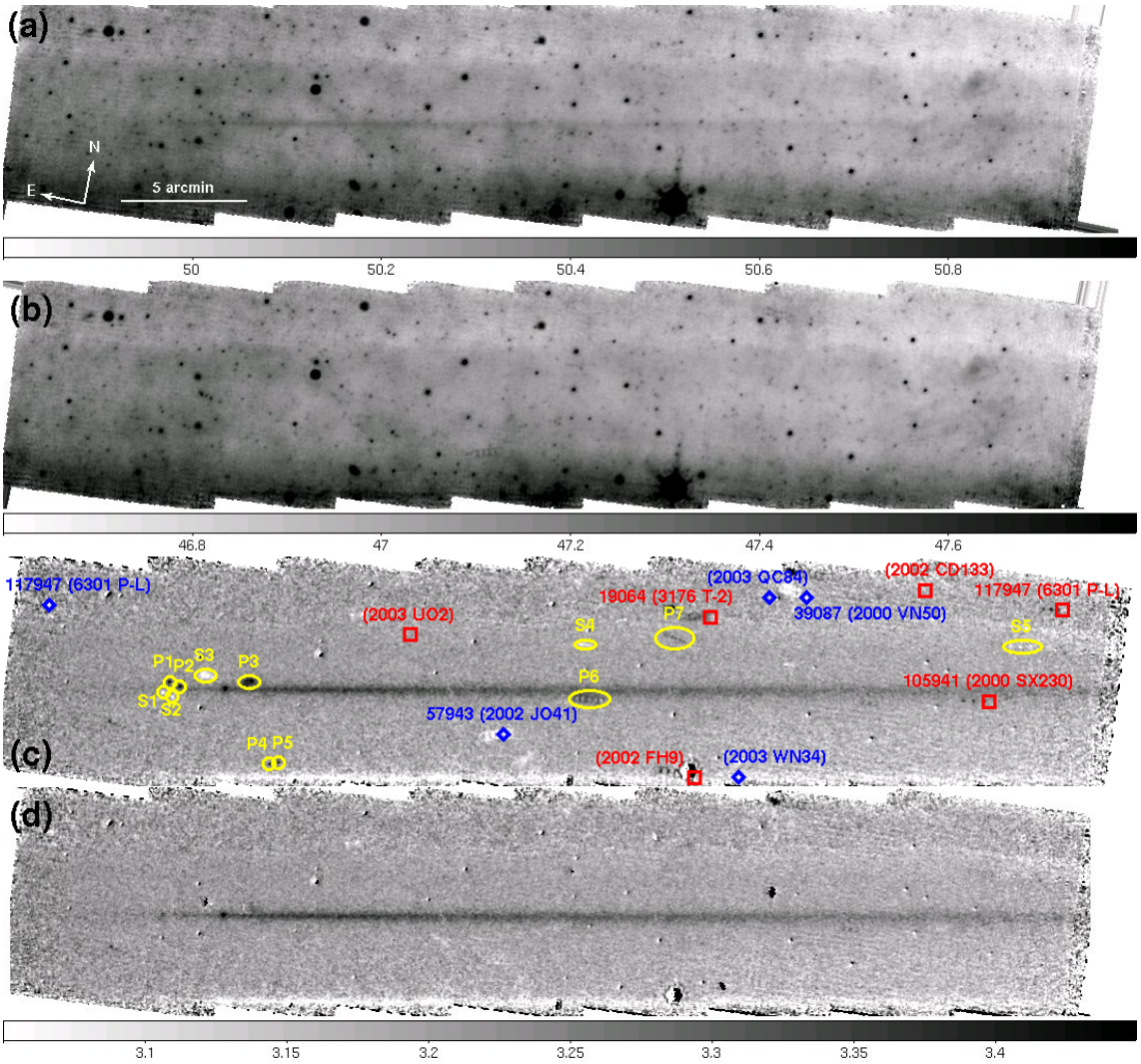

Figure 4.8: a) Mosaics of the images taken in April 2006 with MIPS at 24 μm. The surface brightness indicated by the colourbars below the images is in units of MJy/sr. **a)** Mosaic of the primary observation, the trail is in the centre. **b)** Mosaic of the shadow data, exposed six days later, showing the same section of the sky. The trail is visible close to the lower margin of the mosaic. **c)** Difference of primary and shadow with several moving objects not removed by the automatic outlier detection included in MOPEX. Moving objects from the primary observation are black, those from the shadow are white. The positions of identified known asteroids in primary and shadow are labelled with red boxes and blue diamonds, respectively. Unidentified moving objects discussed in the text are marked with yellow ellipses. **d)** Difference image of primary and shadow after masking of the moving objects marked in Panel (c).

intervals in between. A moving target appears as a sequence of six seemingly individual sources. In the eastern part of the mosaic, moving objects appear as a sequence of three sources, of which two are brighter than the third, because these were exposed twice as often.

The outlier detection routine included in MOPEX identifies and masks a moving object if it is present at a given position on the sky in less that a pre-defined fraction of the

images. The probability that a moving target is identified depends therefore on the apparent speed of the target and – due to the scanning sequence – on its position in the FOV. In the western part of the FOV, each of the three images of a moving target is present in one third of the exposures, in the central part in one sixth, and in the eastern part in one third for the two central images of a moving target and in one sixth for the first and last one, with a smooth transition between these scenarios. Some moving objects in the central part of the mosaic (Figure 4.8c) appear as rings rather than as point sources. A probable reason is that only the first order peak of the point spread function (PSF) was masked by the outlier rejection routine, while the remaining rings are the second order of the PSF.

Since a couple of moving objects are close to the nucleus and projected orbit of 67P/C–G it was investigated whether any of these could be a fragment of the comet. Such a fragment would be co-moving with the comet.

The moving objects identified by ISPY are all asteroids, labelled red and blue in Figure 4.8c, depending on whether they occur in the primary or in the shadow. 67P/C–G was not identified by ISPY because of the strong variability of its orbital elements. Since this is a characteristic of all comets, the precise ephemerides of all comets in the JPL database for the time of observation were obtained without ISPY. With the exception of 67P/C–G, none were in the FOV. For asteroids this procedure was not repeated because of the comparatively large number of known asteroids.

Some of the moving objects not identified by ISPY are labelled yellow in Figure 4.8c. None of these can be considered a candidate for a fragment 67P/C–G. Separate inspection of frames taken at different times shows that P1 and P2 are the same object, a third appearance of this object (from the first exposure) is to the west of P2 in the original data but was removed in the mosaic by the outlier-rejection procedure. The same holds for S1 and S2, and P4 and P5, respectively. S3 and P3 are each tracks of moving objects with low apparent speeds. The objects labelled S4, P6, and P7, located in the central part of the image, each appear as a sequence of six images, while S5 – close to the western edge of the FOV – appears three times. Since all these objects have a non-zero apparent speed relative to the comet, they cannot be fragments of it. All moving objects marked in Figure 4.8c were masked manually and excluded from co-addition. The resulting mosaic is shown in Figure 4.8d.

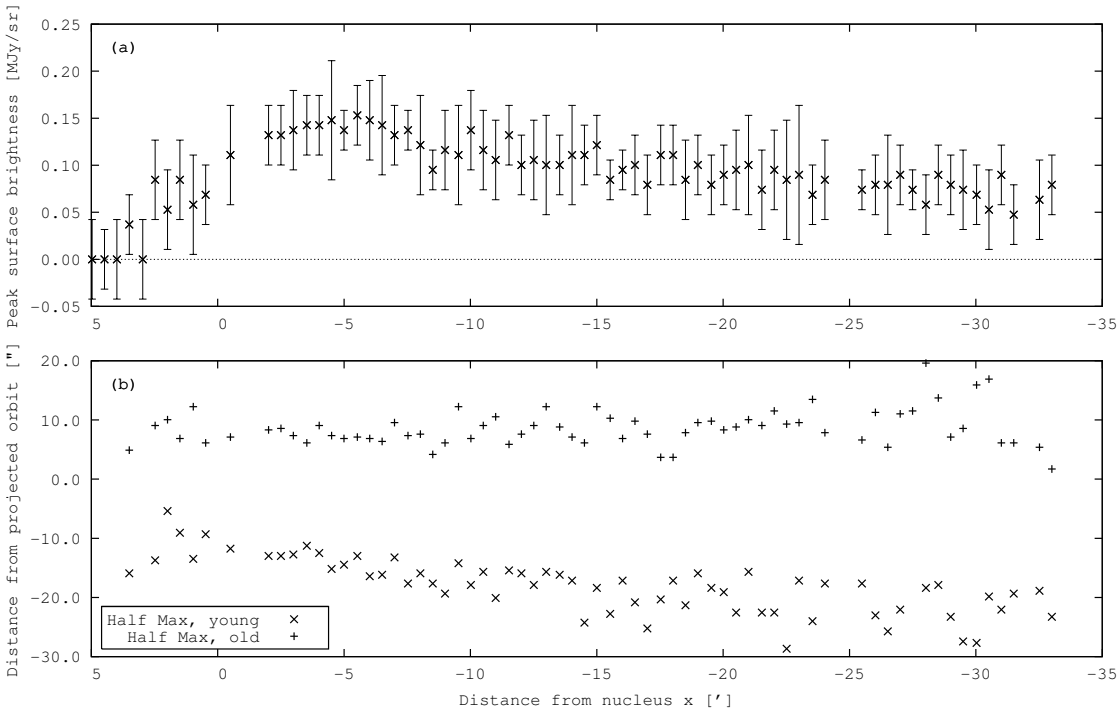

Figure 4.9: Brightness profile and FWHM of the trail, derived from the image shown in Figure 4.8d. **a)** Colour-corrected peak surface brightness along the projected orbit as a function of distance from the nucleus. The error bars are derived from the estimated variation of the background. **b)** FWHM of the trail as a function of distance from the nucleus. "+" and "x" mark the distances from the projected orbit where the surface brightness is half of the peak brightness.

4.3 Discussion of Observations

Comparison of Figures 4.7c, d and 4.9a, b shows that the surface brightness of the trail was lower in April 2006 than in August 2005 while its FWHM remained approximately constant. The measured surface brightness is independent of the distance Δ between the telescope and the trail, because the amount of particles per unit solid angle is proportional to Δ^2, while the radiation received from a single particle is proportional to Δ^{-2}. Since the heliocentric distances were similar, the blackbody equilibrium temperature would also be similar. On 29 August 2005, 2° in mean anomaly corresponded to 35.3′ projected, compared with 38.0′ projected on 9 April 2006. Hence the column density of dust did not change significantly between the two observations. The observed decrease in brightness cannot therefore be attributed to changes in the observation geometry but must be explained from particle dynamics, which is discussed in Chapter 6.

In all three images, the distance of the half maximum from the projected orbit is almost constant on one side of the trail and increases with distance from the nucleus on the other side. The constant side is marked by "+" in the plots, the other by "x". The "x"-side appears in projection on the southern side of the trail for the WFI and the Spitzer 2006 images, on the northern side in the Spitzer 2005 image. Defining the "upper" side of an orbit as the one out of which the positive angular momentum vector points, the observer was below the orbital plane of the comet during the 2004 and 2006 observations (orbit plane angles $-0.7°$ and $-1.2°$, see Table 4.1) and above the plane in 2005 (orbit plane angle 1.3°). Assuming that all dust remains close to the comet orbital plane, the particles on the "x"-side are outside the orbit if seen from the inner solar system. They must therefore be subject to stronger radiation pressure than those remaining close to the orbit. Simulations presented in Chapter 6 will confirm that particles on the "+"-side are larger ones remaining close to the orbit even after several orbital revolutions, while smaller particles (subject to stronger radiation pressure) emitted during the 2002/03 perihelion passage are found on the "x"-side.

Chapter 5

Simulation of Trail Images

To interpret the observations described in the previous chapter, a numerical procedure was implemented to generate simulated images of the cometary trail – in the general sense defined in Section 2.1, i. e. including both the old trail and the tail and neckline. After a short introduction (Section 5.1), the mathematical method is described in Sections 5.2 and 5.3. The parameters of the physical model of the comet and the emitted dust are discussed in Section 5.4.

5.1 Motivation

The position of a dust particle in a cometary trail is a function of the emission time and velocity, and of the radiation pressure coefficient β (Section 2.4). In the following it is assumed that the emission speeds of dust from the nucleus are isotropic, and that dust trajectories are determined by solar gravitation and radiation pressure only.

A "dust shell" describes the ensemble of locations occupied by dust particles characterised by a certain radiation pressure coefficient β, and released at the time t_e from the comet in all directions with the emission speed v_e. The time evolution of the shape and size of a shell is described by Müller et al. (2001). During a short interval after emission, the shell can be approximated by a sphere the centre of which is off-set from the comet due to radiation pressure (Finson and Probstein, 1968). The position $\mathbf{r}$ of a particle in the shell is given by

$$\mathbf{r}(t, \beta, \mathbf{v}_\mathrm{e}) = \mathbf{r}(t, \beta, 0) + (t - t_\mathrm{e}) * \mathbf{v}_\mathrm{e}, \tag{5.1}$$

where $\mathbf{v}_\mathrm{e}$ is the emission velocity of the particle and $\mathbf{r}(t, \beta, 0)$ is the position at the time t of an auxiliary particle having the same β and t_e but zero ejection speed. The auxiliary particle does therefore not belong to the ensemble of shell particles. On longer timescales, the shell is distorted into an ellipsoid by tidal forces (Kimura and Liu, 1977). Equation 5.1 was therefore generalised by Fertig and Schwehm (1984) to

$$\mathbf{r}(t, \beta, \mathbf{v}_\mathrm{e}) = \mathbf{r}(t, \beta, 0) + \mathbf{\Phi}(t, t_\mathrm{e}) * \mathbf{v}_\mathrm{e}. \tag{5.2}$$

Analytical expressions for the elements of the matrix $\mathbf{\Phi}$ were derived by Massonne (1985, 1987) from Keplerian dynamics. When the shell becomes more elongated, also the de-

scription by an ellipsoid ceases to be valid. Large particles are then found on a tube bending around the comet orbit, while small particles have been dispersed by radiation pressure. To approximate particle positions on the elongated shell, a local linearisation was introduced by Müller et al. (2001). For this purpose, the tube is cut into slices roughly perpendicular to its central axis. The auxiliary particle used in Equations 5.1 and 5.2 is replaced by a reference particle in the centre of the slice (Kondrateva and Reznikov, 1985; Müller et al., 2001), characterised by the same β and $t_{\rm e}$ as the shell, but different $v_{\rm e}$. The position of a particle on the slice i is expressed as

$$\mathbf{r}(t,\beta,\mathbf{v}_{\rm e}) = \mathbf{r}_{\rm ref}^{(i)}(t) + \mathbf{\Phi}^{(i)}(t,t_{\rm e},\beta,\mathbf{v}_{\rm ref}^{(i)}) * (\mathbf{v}_{\rm e} - \mathbf{v}_{\rm ref}^{(i)}), \tag{5.3}$$

where $\mathbf{r}_{\rm ref}^{(i)}$ is the position of the reference particle at the observing time and $\mathbf{v}_{\rm ref}^{(i)}$ is its ejection velocity. For Keplerian motion, the elements of the matrix $\mathbf{\Phi}^{(i)}$ can be calculated analytically in analogy to those given by Massonne (1985, 1987) for the matrix in Equation 5.2.

To take into account planetary perturbations the positions of the reference particles and the matrix elements must be obtained by numerical integration of the equation of motion of the nucleus and of its Jacobian matrix, respectively. This method was used by Müller et al. (2003) to successfully predict the 2001 Leonid meteor shower. Since the numerical integration has to be performed only for a small set of reference trajectories and the related matrices, this method consumes less computational time than a Monte Carlo approach requiring the numerical integration of the equation of motion of every single particle. In the present work, the analytical expressions based on the orbital elements of the comet are used. (See discussion in Section 5.4.3.)

Müller et al. (2001) have shown that the position of a particle along the shell is controlled by its orbital period. Decomposing the particle emission velocity relative to the comet into its components parallel and perpendicular to the comet velocity vector, $\mathbf{v}_{\rm e} = \mathbf{v}_{\rm e,\parallel} + \mathbf{v}_{\rm e,\perp}$, the specific orbital energy E/m of the particle is

$$\begin{aligned}
\frac{E}{m} &= \frac{1}{2}(\mathbf{v}_{\rm nucl} + \mathbf{v}_{\rm e,\parallel} + \mathbf{v}_{\rm e,\perp})^2 - \frac{GM_\odot(1-\beta)}{r} \\
&= \frac{E_{\rm nucl}}{m_{\rm nucl}} + \mathbf{v}_{\rm nucl}\mathbf{v}_{\rm e,\parallel} + \frac{1}{2}(\mathbf{v}_{\rm e,\parallel}^2 + \mathbf{v}_{\rm e,\perp}^2) + \frac{GM_\odot\beta}{r} \\
&= -\frac{GM_\odot}{2a} \propto \frac{1}{T^{3/2}}.
\end{aligned} \tag{5.4}$$

The last line gives the relation between the orbital energy, the semi-major axis a and the orbital period T of the particle. Equation 5.4 shows that to first order the orbital period of the particle – and therefore also its position along the shell – depends only on the component of the ejection velocity that was parallel to the orbital velocity of the comet at the ejection time. For this reason, reference particles are used that were emitted parallel or anti-parallel to the direction of the heliocentric velocity of the comet.

The slices of the tube are chosen to correspond to pixel columns in the image. For every pixel-column $x = x_i$, a reference particle (characterised by β and emitted at $t_{\rm e}$) is determined that is located at x_i at the observing time t. For this column, the elements

of the matrix $\mathbf{\Phi}^{(i)}$ are then calculated. By inverting Equation 5.3, the emission direction of a particle observed at a given point in column i is obtained. Repeating this operation for the four corners of a given pixel, the corresponding fraction of solid angle in the space of emission directions is calculated. From the – in general direction-dependent – dust production rate follows the amount of dust observed in this pixel. By applying the described procedure to all pixels in all columns, the image of one particle shell is obtained. The final image is constructed as the sum of images of shells emitted at various times t_e and characterised by various radiation pressure parameters β and emission speeds v_e.

5.2 Mathematical Method

5.2.1 Coordinate Systems

The coordinate system used to describe the image has its origin at the comet nucleus, and (x, y, z) form a right-handed, orthogonal system. The z-axis is along the line of sight, pointing away from the observer. The x-axis is parallel to the Earth's equatorial plane, and x increases with right ascension (RA), from right (west) to left (east) for an observer looking at the sky. The y-axis completes the orthogonal system, pointing northward in projection. It is assumed that the x-y-plane corresponds to the image plane, which introduces a distortion for larger fields of view.

A second comet-centred coordinate system is the *Cometocentric Bipolar System* (CBS) (Massonne, 1987). It is spanned by the orthogonal vectors (ξ,χ,ζ), where the ζ-axis is along the line Sun-comet, pointing away from the Sun. The ξ-axis is in the orbital plane of the comet, perpendicular to ζ, and pointing in the direction of motion. χ completes the right-handed system.

5.2.2 Reference Trajectories

A set of reference particles is defined that have the same β and t_e as the shell to be depicted, but not the same emission speed. All reference particles have been emitted in the direction of the heliocentric velocity vector of the comet $\mathbf{e}_{\mathrm{v,nucl}}(t_\mathrm{e})$, with varying absolute speeds. One reference particle J is needed for each pixel-column x_j in the image. To find the corresponding emission speeds $v_{\parallel,j}(x_j)$, an auxiliary set of particles i with emission speeds $v_{\parallel,i}$ is defined and the particle positions x_i in the image calculated. The speeds of the reference particles $v_{\parallel,j}(x_j)$ are found by interpolation of the relation $x_i(v_{\parallel,i})$. The orbital elements of each reference particle j are calculated from its heliocentric state vector at emission and β. The coordinates (x_j, y_j, z_j) of the reference particles at the time of observation are denoted by the vectors $\mathbf{r}_{0,j}$.

5.2.3 Linearisation

The position $\mathbf{r}(t_\mathrm{obs})$ of a particle with emission velocity $\mathbf{v}_\mathrm{e} = v_{\parallel,j}\mathbf{e}_{\mathrm{v,nucl}} + \Delta\mathbf{v}$ is linearised around $\mathbf{r}_{0,j}$ for not too large $\Delta\mathbf{v}$:

$$\mathbf{r}(t_\mathrm{obs}) = \mathbf{r}_{0,j}(t_\mathrm{obs}) + \mathbf{\Psi_j}\Delta\mathbf{v}. \tag{5.5}$$

The transformation matrix $\mathbf{\Psi_j}$ depends on the trajectory of the reference particle and on the dates of emission and observation. $\mathbf{\Psi_j}$ is defined such that $\Delta\mathbf{v}$ is given in the CBS-frame, whereas the positions $\mathbf{r}$ are in image coordinates.

If the particle trajectories are considered as Keplerian orbits with the gravitational potential modified by the factor $\Delta\mu = (1 - \beta)$, the elements of the matrix are obtained in analogy to Massonne (1987). In the latter work the nucleus is used as reference object, whereas in the present case, dust particles are the reference objects. The full transformation formula is as follows (Massonne, 1987, pp. 127-128):

$$\mathbf{r}^{\,\mathrm{CBS}}(t) = \underbrace{\frac{1}{\delta\tau/\delta t|_{t_\mathrm{e}}} \begin{pmatrix} \Phi_{22} & 0 & \Phi_{21} \\ 0 & \Phi_{33} & 0 \\ \Phi_{12} & 0 & \Phi_{11} \end{pmatrix} \mathbf{v}_\mathrm{e}^{\mathrm{CBS}}(t_\mathrm{e})}_{\mathrm{I}} + \underbrace{a(1-e^2)\frac{\Delta\mu}{\mu} \begin{pmatrix} \psi_2 \\ 0 \\ \psi_1 \end{pmatrix}}_{\mathrm{II}}. \qquad (5.6)$$

Part II describes the change in trajectory due to the different strength of radiation pressure for the nucleus and a dust particle. In the present approach, β is the same for the reference particle and the shell particles. Hence part II is always zero. In part I, $\delta\tau/\delta t|_{t_\mathrm{e}}$ is the time derivative of the true anomaly of the reference object at the time of emission:

$$\delta\tau/\delta t|_{t_\mathrm{e}} = \sqrt{\frac{\mu\,(1-\beta)}{a^3(1-e^2)^3}}\,(1 + e\cos\tau_\mathrm{e})^2. \qquad (5.7)$$

$\mu = GM_\odot = 1.33\times10^{20}$ m^3/s^2 is the gravitational potential of the Sun, and a, e, and τ are the semi-major axis, eccentricity and true anomaly of the reference object, respectively. β is the radiation pressure coefficient of the reference object (i. e. $\beta = 0$ in the situation described by Massonne). The matrix elements Φ_{mn} are functions of t_obs, t_e, τ_obs, τ_e, a, and e. $\mathbf{r}^{\,\mathrm{CBS}}(t)$ and $\mathbf{v}_\mathrm{e}^{\mathrm{CBS}}(t_\mathrm{e})$ are in CBS-coordinates centred on the reference object at the times t and t_e, respectively.

The $\Delta\mathbf{v}$ of Equation 5.5 is equivalent to $\mathbf{v}_\mathrm{e}^{\mathrm{CBS}}(t_\mathrm{e})$ of Equation 5.6. It follows that

$$\mathbf{\Psi_j} = \frac{1}{\delta\tau_j/\delta t|_{t_\mathrm{e}}}\,\mathbf{T_j^{cbs-im}}(t_\mathrm{obs}) \begin{pmatrix} \Phi_{22} & 0 & \Phi_{21} \\ 0 & \Phi_{33} & 0 \\ \Phi_{12} & 0 & \Phi_{11} \end{pmatrix}, \qquad (5.8)$$

where $\mathbf{T_j^{cbs-im}}(t_\mathrm{obs})$ is the matrix to transform reference-particle centred CBS-coordinates to image coordinates relative to the reference particle. The orbital elements in $\mathbf{\Psi_j}$ and $\delta\tau_j/\delta t|_{t_\mathrm{e}}$ are those of the reference particle, τ_j, a_j, and e_j.

5.2.4 Reference Frame in Ejection Velocity Space

A reference frame in the space of ejection velocities is defined with unit vectors $\mathbf{u}_j$, $\mathbf{v}_j$, $\mathbf{w}_j$ such that

$$\begin{aligned} \lambda\,\mathbf{e}_z &= \mathbf{\Psi_j}\,\mathbf{u}_j && (5.9)\\ \nu\,\mathbf{e}_y + \mu\,\mathbf{e}_z &= \mathbf{\Psi_j}\,\mathbf{v}_j && (5.10)\\ |\mathbf{u}_j| = |\mathbf{v}_j| &= 1 && (5.11)\\ \mathbf{u}_j\mathbf{v}_j &= 0 && (5.12)\\ \mathbf{w}_j &= \mathbf{u}_j \times \mathbf{v}_j. && (5.13) \end{aligned}$$

A particle emitted with $\Delta\mathbf{v} = \mathbf{u}_j$ will be located on the same line of sight as the reference particle, i. e. $x = x_{0,j}$ and $y = y_{0,j}$. For $\Delta\mathbf{v} = \mathbf{v}_j$, the particle will have $x = x_{0,j}$, but $y \neq y_{0,j}$. To be consistent with the definition of $\mathbf{\Psi_j}$, the unit vectors $\mathbf{u}_j$, $\mathbf{v}_j$, $\mathbf{w}_j$ need to be given in the CBS-frame at the time t_e. By $\Delta\mathbf{v} = \rho\mathbf{u}_j + \sigma\mathbf{v}_j$, a plane in the $\Delta\mathbf{v}$-space is defined that contains all possible $\Delta\mathbf{v}$ for particles to lie in the image column characterised by $x = x_{0,j}$. If

$$\mathbf{T_j^{uvw-cbs}}(t_\mathrm{e}) = \begin{pmatrix} u_{j,1}^\mathrm{cbs} & v_{j,1}^\mathrm{cbs} & w_{j,1}^\mathrm{cbs} \\ u_{j,2}^\mathrm{cbs} & v_{j,2}^\mathrm{cbs} & w_{j,2}^\mathrm{cbs} \\ u_{j,3}^\mathrm{cbs} & v_{j,3}^\mathrm{cbs} & w_{j,3}^\mathrm{cbs} \end{pmatrix} \qquad (5.14)$$

is the matrix to transform coordinates from the (u,v,w)-system to the CBS frame, the matrix $\tilde{\mathbf{\Psi}}_\mathbf{j} = \mathbf{\Psi_j}\mathbf{T_j^{uvw-cbs}}$ by definition takes the form

$$\tilde{\mathbf{\Psi}}_\mathbf{j} = \mathbf{\Psi_j}\mathbf{T_j^{uvw-cbs}} = \begin{pmatrix} 0 & 0 & c_1 \\ 0 & \nu & c_2 \\ \lambda & \mu & c_3 \end{pmatrix}, \qquad (5.15)$$

where the vector $\mathbf{c} = \mathbf{\Psi_j}\mathbf{w}_j$ has been defined. $\mathbf{c}$, λ, μ, and ν depend on j, but the index is omitted here for the sake of legibility.

5.2.5 Mapping Emission Direction to Position in Image

Any vector $\mathbf{v}$ can be expressed as a sum of the unit vectors $\mathbf{u}_j$, $\mathbf{v}_j$, $\mathbf{w}_j$:

$$\mathbf{v} = v\sin\theta\sin\phi\,\mathbf{u}_j + v\sin\theta\cos\phi\,\mathbf{v}_j + v\cos\theta\,\mathbf{w}_j, \qquad (5.16)$$

where $\theta \in [0,\pi]$ and $\phi \in [0,2\pi]$. Hence, $\Delta\mathbf{v}$ is

$$\begin{aligned} \Delta\mathbf{v} &= \mathbf{v}_\mathrm{e} - v_{\parallel,j}\,\mathbf{e}_\mathrm{v,nucl} \\ &= v_\mathrm{e}\sin\theta\sin\phi\,\mathbf{u}_j + v_\mathrm{e}\sin\theta\cos\phi\,\mathbf{v}_j + v_\mathrm{e}\cos\theta\,\mathbf{w}_j - v_{\parallel,j}\mathbf{e}_\mathrm{v,nucl}. \qquad (5.17) \end{aligned}$$

Taking into account Equations 5.9 - 5.13, Equation 5.8 reads

$$\begin{aligned}\mathbf{r} &= \mathbf{r}_{0,j} + \mathbf{\Psi_j}\Delta\mathbf{v} \\ &= \mathbf{r}_{0,j} + v_\mathrm{e}\,(\sin\theta\sin\phi\,\underbrace{\mathbf{\Psi_j}\mathbf{u}_j}_{\lambda\,\mathbf{e}_z} + \sin\theta\cos\phi\,\underbrace{\mathbf{\Psi_j}\mathbf{v}_j}_{\nu\,\mathbf{e}_y+\mu\,\mathbf{e}_z} + \cos\theta\,\underbrace{\mathbf{\Psi_j}\mathbf{w}_j}_{\mathbf{c}}) - v_{\parallel,j}\,\underbrace{\mathbf{\Psi_j}\mathbf{e}_{\mathrm{v,nucl}}}_{\sigma}\end{aligned} \tag{5.18}$$

or component-wise

$$x = x_{0,j} + v_\mathrm{e}\,c_1\cos\theta - v_{\parallel,j}\,\sigma_1 \tag{5.19}$$

$$y = \underbrace{y_{0,j} + v_\mathrm{e}\,c_2\cos\theta - v_{\parallel,j}\,\sigma_2}_{\tilde{y}_j(\theta)} + \underbrace{v_\mathrm{e}\,\nu\sin\theta}_{\Delta y_{\max}(\theta)}\cos\phi. \tag{5.20}$$

These equations relate the direction of emission of a particle to its position in the image. They can be inverted to give $\theta(x)$ and $\phi(x, y)$:

$$\cos\theta = \frac{v_{\parallel,j}\,\sigma_1 + (x - x_{0,j})}{v_\mathrm{e}\,c_1} \tag{5.21}$$

$$\cos\phi = \frac{y - \tilde{y}_j(\theta(x))}{\Delta y_{\max}(\theta(x))}. \tag{5.22}$$

For fixed θ, the full ring-segment in a pixel-column covers all values of $\phi \in [-\pi, \pi]$. The borders of the projected shell are characterised by $\phi = \pi$ and $\phi = 0$, respectively. Hence, the two parts of a shell (front and back) in the given pixel are described by the two angles $\phi(\theta)$ and $-\phi(\theta)$. The sign of $\sin\phi$ does not change within a given side of the shell.

5.2.6 Parameters of the Map

To exploit Equations 5.21 and 5.22, the parameters ν, c_1, c_2, σ_1, and σ_2 need to be evaluated. First, the inverse matrix $\mathbf{\Psi_j}^{-1}$ is calculated. The column vectors in $\mathbf{\Psi_j}^{-1}$ are denoted as $\mathbf{\Psi}^{-1}_{j(i)}$ with i = 1 . . . 3 such that

$$\mathbf{\Psi_j}^{-1} = (\mathbf{\Psi}^{-1}_{j(1)}, \mathbf{\Psi}^{-1}_{j(2)}, \mathbf{\Psi}^{-1}_{j(3)}) = \begin{pmatrix} \Psi^{-1}_{j1,(1)} & \Psi^{-1}_{j1,(2)} & \Psi^{-1}_{j1,(3)} \\ \Psi^{-1}_{j2,(1)} & \Psi^{-1}_{j2,(2)} & \Psi^{-1}_{j2,(3)} \\ \Psi^{-1}_{j3,(1)} & \Psi^{-1}_{j3,(2)} & \Psi^{-1}_{j3,(3)} \end{pmatrix}. \tag{5.23}$$

Equation 5.9 yields that $\mathbf{u}_j = \lambda\mathbf{\Psi}^{-1}_{j(3)}$. With $|\mathbf{u}_j| = 1$ (Equation 5.11) follows

$$\lambda = \frac{1}{\sqrt{(\Psi^{-1}_{j1,(3)})^2 + (\Psi^{-1}_{j2,(3)})^2 + (\Psi^{-1}_{j3,(3)})^2}}. \tag{5.24}$$

Equation 5.10 gives

$$\mathbf{v}_j = \nu\,\mathbf{\Psi}^{-1}_{j(2)} + \mu\,\mathbf{\Psi}^{-1}_{j(3)}. \tag{5.25}$$

Multiplication with $\mathbf{u}_j$ results in

$$0 = \mathbf{u}_j \, \mathbf{v}_j = \lambda \, \nu \, \mathbf{\Psi}^{-1}_{j(2)} \, \mathbf{\Psi}^{-1}_{j(3)} + \lambda \, \mu \, \underbrace{(\mathbf{\Psi}^{-1}_{j(3)})^2}_{1/\lambda^2}, \tag{5.26}$$

which can be solved for $\mu/\nu \, (\lambda, \mathbf{\Psi}^{-1}_{\mathbf{j}})$. Re-insertion into Equation 5.25 gives the vector $\mathbf{v}_j/\nu$, from which ν is obtained due to the normalisation of $\mathbf{v}_j$. Then it is straightforward to calculate $\mathbf{w}_j = \mathbf{u}_j \times \mathbf{v}_j$, $\mathbf{c} = \mathbf{\Psi_j} \mathbf{w}_j$, and $\sigma = \mathbf{\Psi_j} \, \mathbf{e}_{\mathrm{v,nucl}}$.

5.3 Number Density of Particles in a Pixel

5.3.1 General Solution

The aim of this section is to calculate the number density of particles in a given pixel confined by the coordinates (x_1, y_1) and (x_2, y_2). The distribution of particles released to a unit solid angle is given by

$$\frac{\mathrm{d}N}{\mathrm{d}\Omega}(\phi,\theta) = \frac{\mathrm{d}N(\phi,\theta)}{\mathrm{d}\phi\,\mathrm{d}\cos\theta}, \tag{5.27}$$

where $\theta(x)$ and $\phi(x,y)$ are the comet-centred angles defined in Equations 5.21 and 5.22. The amount of dust N in this pixel is obtained by

$$\begin{aligned} N &= \int_{x_1}^{x_2}\int_{y_1}^{y_2} \frac{\mathrm{d}N}{\mathrm{d}x\,\mathrm{d}y}\mathrm{d}y\,\mathrm{d}x \\ &= \left| \int_{\cos\theta_1(x_1)}^{\cos\theta_2(x_2)} \mathrm{d}\cos\theta \int_{\phi_1(y_1,\cos\theta)}^{\phi_2(y_2,\cos\theta)} \mathrm{d}\phi\, \frac{\mathrm{d}N}{\mathrm{d}\Omega}(\phi,\cos\theta) \right| + \left| \int_{\cos\theta_1(x_1)}^{\cos\theta_2(x_2)} \mathrm{d}\cos\theta \int_{-\phi_2(y_1,\cos\theta)}^{-\phi_1(y_2,\cos\theta)} \mathrm{d}\phi\, \frac{\mathrm{d}N}{\mathrm{d}\Omega}(\phi,\cos\theta) \right| \\ &= |N_1| + |N_2|\,. \end{aligned} \tag{5.28}$$

The first integral represents the number density in the side of the shell with $0 < \phi < \pi$ while the second integral represents the side with negative ϕ. Therefore, N_1 and N_2 cannot compensate each other.

If a horizontal boundary of the pixel is inside the projected shell, the corresponding limit of the inner integrals in Equation 5.28 is given by Equation 5.22. This is in the following referred to as a "normal" integration limit. If the edge of the projected shell is inside the pixel, the limit $\pm\phi_i\,(y_j, \cos\theta)$ of the inner integral must be set to ϕ = 0 or $\phi = \pi$ as appropriate (henceforth called an "anomalous" integration limit). Introducing $z = \cos\theta$, the inner integration limits in Equation 5.28 are described by

$$\phi(y,z) = \begin{cases} \phi_{\mathrm{nm}}(y,z) & |\cos(\phi_{\mathrm{nm}})| < 1 \\ \\ \phi_{\mathrm{an}} & \text{else} \end{cases} \tag{5.29}$$

with $\phi_{\mathrm{nm}}(y,z)$ given by Equation 5.22, and $\phi_{\mathrm{an}} \in \{0,\pi\}$. The careful evaluation of contributions from the edges of the projected shell is critical, because a significant fraction of the dust can be concentrated in these pixels due to the shallow angle between the line of sight and the surface of the shell.

As an example, the integral N_1 is given for the situation depicted in Figure 5.1. Intro-

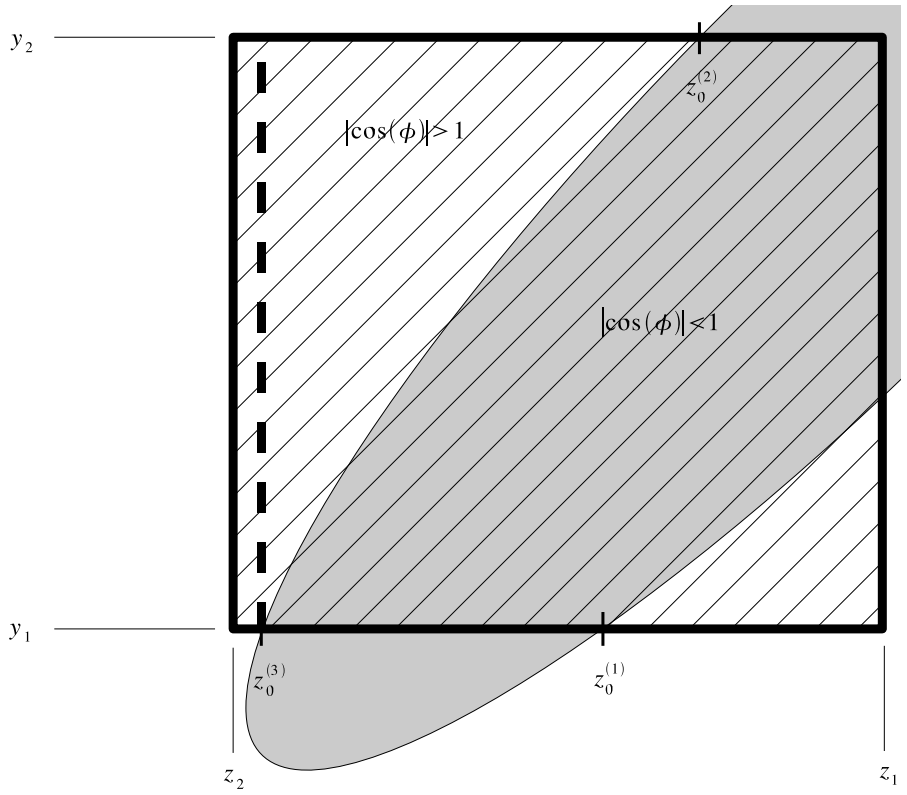

Figure 5.1: Example for a pixel (hatched area) containing part of the edges of a shell (area covered by shell is grey). The $z_0^{(i)}$ are defined by $z_0^{(i)} = z(|\cos\phi| = 1, y_j)$. The integration limits for this pixel are as follows: on the upper pixel boundary, $\phi = \phi_{\rm nm}(y_2, z)$ for $z \in [z_1, z_0^{(2)}]$, while $\phi = \phi_{\rm an}(y_2)$ for the rest. On the lower pixel boundary, $\phi = \phi_{\rm nm}(y_1, z)$ for $z \in [z_0^{(1)}, z_0^{(3)}]$, and $\phi = \phi_{\rm an}(y_1)$ for $z \in [z_1, z_0^{(1)}]$. For $z \in [z_0^{(3)}, z_2]$, neither boundary contributes. Hence this section does not have to be considered at all. This effectively corresponds to a shortening of the pixel, indicated by the dashed vertical line.

ducing $dN/d\Omega = f(\phi, z)$ and its antiderivative $F(\phi, z)$, the integral N_1 is

$$\begin{aligned} N_1 &= \int_{z_1}^{z_2} \mathrm{d}z \int_{\phi_1(y_1,z)}^{\phi_2(y_2,z)} \mathrm{d}\phi\, f(\phi, z) \\ &= \int_{z_1}^{z_2} \mathrm{d}z\, [F(\phi_2(y_2, z), z) - F(\phi_1(y_1, z), z)] \\ &= \int_{z_1}^{z_0^{(2)}} \mathrm{d}z F(\phi_{\rm nm}(y_2, z), z) + \int_{z_0^{(2)}}^{z_0^{(3)}} \mathrm{d}z F(\phi_{\rm an}(y_2, z_2), z) \\ &\quad - \int_{z_1}^{z_0^{(1)}} \mathrm{d}z F(\phi_{\rm an}(y_1, z_1), z) - \int_{z_0^{(1)}}^{z_0^{(3)}} \mathrm{d}z F(\phi_{\rm nm}(y_1, z), z). \end{aligned} \tag{5.30}$$

For each horizontal pixel boundary, five scenarios of intersection with the edge of the shell can be distinguished. These are depicted in Figure 5.2.

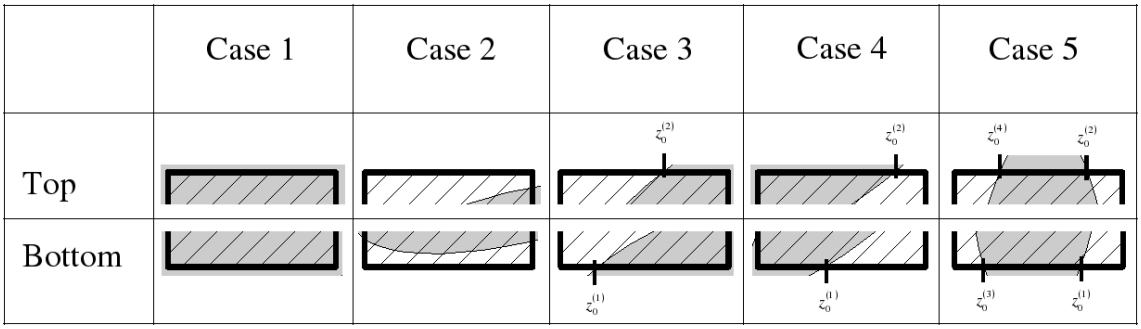

Figure 5.2: Different possibilities of pixel boundaries intersecting the edge of a shell. The area covered by the shell is grey. The upper and lower rows show situations for the upper and lower pixel boundaries, respectively. Different "cases" occur independently for the upper and lower pixel boundary. **1**: Both corners are covered by the shell. **2**: Both corners are outside the shell. If this scenario is given on both pixel boundaries, the pixel is either empty ($\phi_1 = \phi_2$) or the shell is thinner than the height of the pixel ($\phi_{1/2} = \pi$ and $\phi_{2/1} = 0$). This situation occurs for shells that are collapsed to a neckline (Section 2.1.) **3**: The right corner is inside, the left corner outside the shell. **4**: The inverse of case 3. **5**: Both corners are outside the shell, but there are two shell intersections in between. The possible sixth case (inverse of 5) cannot occur because shells are convex. In all cases, if there is only one intersection, the intersection point is labelled $z_0^{(1)}$ on the lower pixel boundary and $z_0^{(2)}$ on the upper one. If there is a second intersection, the leftmost intersection point is labelled $z_0^{(3)}$ on the lower and $z_0^{(4)}$ on the upper boundary.

5.3.2 Isotropic Dust Emission

Isotropic emission is described by $f = \mathrm{d}N/\mathrm{d}\Omega = Q/4\pi$. In this instance, the integral in Equation 5.28 can be solved analytically. For symmetry reasons, the contributions from the front and back sides of the shell are identical, and Equation 5.28 simplifies to $N^{(\mathrm{iso})} = 2\,N_1^{(\mathrm{iso})}$ with

$$N_1^{(\mathrm{iso})} = \int_{z_1}^{z_2} \mathrm{d}z \int_{\phi(y_1,z)}^{\phi(y_2,z)} \mathrm{d}\phi \, \frac{\mathrm{d}N}{\mathrm{d}\Omega}(\phi, z) = \frac{Q}{4\pi} \int_{z_1}^{z_2} \mathrm{d}z \, [\phi(y_2, z) - \phi(y_1, z)] = N_{1a}^{(\mathrm{iso})} - N_{1b}^{(\mathrm{iso})}, \quad (5.31)$$

where $z_1 = z(x_1)$, $z_2 = z(x_2)$, and "a" and "b" refer to the upper and lower pixel boundary ($y = y_2$ and $y = y_1$), respectively.

Normal integration limits. If the part of the upper pixel boundary that is inside the shell is limited by z_α and z_β (in the example given in Equation 5.30 $z_\alpha = z_1$ and $z_\beta = z_0^{(2)}$), the

corresponding normal part of the integral $N_{1a}^{(\mathrm{iso})}$ is given by

$$\begin{aligned}
N_{1a}^{(\mathrm{iso})} &= \frac{Q}{4\pi}\int_{z_\alpha}^{z_\beta} \mathrm{d}z\ \phi_{\mathrm{nm}}(y_2, z) \\
&= \frac{Q}{4\pi}\int_{z_\alpha}^{z_\beta} \mathrm{d}z\ \arccos\left(\frac{y_2 - \tilde{y}_j(\theta(x))}{\Delta y_{\max}(\theta(x))}\right) \\
&= \frac{Q}{4\pi}\int_{z_\alpha}^{z_\beta} \mathrm{d}z\ \arccos\left(\frac{A_2 + Bz}{\sqrt{1-z^2}}\right) \\
&= \frac{Q}{4\pi}\Bigg[z\arccos\left(\frac{A_2 + Bz}{\sqrt{1-z^2}}\right) \\
&\quad -\frac{1}{2}\arctan\left(\frac{A_2^2 + A_2Bz - 1 - p_{2,2}}{(A_2 - B)\sqrt{p_{1,2}}}\right) \\
&\quad +\frac{1}{2}\arctan\left(\frac{A_2^2 + A_2Bz - 1 + p_{2,2}}{(A_2 + B)\sqrt{p_{1,2}}}\right) \\
&\quad -\frac{A_2}{\sqrt{1+B^2}}\ \arctan\left(\frac{p_{2,2}}{\sqrt{1+B^2}\sqrt{p_{1,2}}}\right)\Bigg]_{z_\alpha}^{z_\beta},
\end{aligned} \tag{5.32}$$

with

$$A_2 = \frac{y_2 - y_{j,0} + v_{\parallel,j}\sigma_2}{v_{\mathrm{e}}\nu} \tag{5.33}$$

$$B = -\frac{c_2}{\nu} \tag{5.34}$$

$$p_{1,2} = 1 - z^2 - (A_2 + Bz)^2 \tag{5.35}$$

$$p_{2,2} = z + B^2 z + A_2 B. \tag{5.36}$$

The second index "2" indicates that A_2, $p_{1,2}$, and $p_{2,2}$ depend on the upper pixel boundary ($y = y_2$).

If the edge of the shell intersects the pixel boundary, one or both of z_α and z_β in Equation 5.32 are given by an intersection point rather than by a pixel corner. As discussed at the end of Section 5.2.5, for the value of z in question follows $\cos\phi_{1/2} = \pm 1$, and some simplifications can be introduced into Equation 5.32. To avoid numerical errors at the intersection points, it is advisable to introduce these simplifications explicitely into the

computer code.

$$\frac{A_2 + Bz_{\alpha/\beta}}{\sqrt{1 - z_{\alpha/\beta}^2}} = \pm 1 = k_{\cos}, \tag{5.37}$$

$$p_{1,2} = 0, \tag{5.38}$$

$$p_{2,2} = z_{\alpha/\beta} + k_{\cos} B \sin\theta, \tag{5.39}$$

$$\arctan(\frac{G}{\sqrt{p_{1,2}}}) = \frac{\pi}{2}\,\mathrm{sign}(G). \tag{5.40}$$

The expression $G/\sqrt{p_{1,2}}$ refers to any of the three arguments of the $\arctan$ in the last three lines of Equation 5.32. The simplified expression for the concerned term in $N_{1a,\alpha/\beta}^{(\mathrm{iso})}$ then reads

$$\begin{aligned} N_{1a,\alpha/\beta}^{(\mathrm{iso})} = \frac{Q}{4\pi} \Big[& k z_{\alpha/\beta} \\ & - \frac{\pi}{4}\,\mathrm{sign}\left(\frac{A_2^2 + A_2 B z_{\alpha/\beta} - 1 - p_2}{(A_2 - B)}\right) \\ & + \frac{\pi}{4}\,\mathrm{sign}\left(\frac{A_2^2 + A_2 B z_{\alpha/\beta} - 1 + p_2}{(A_2 + B)}\right) \\ & - \frac{A_2}{\sqrt{1 + B^2}}\,\frac{\pi}{2}\,\mathrm{sign}\,(p_2)\Big]. \end{aligned} \tag{5.41}$$

The solution of $N_{1b}^{(\mathrm{iso})}$ is analogous to $N_{1a}^{(\mathrm{iso})}$, replacing y_2 by y_1, and in general with different values for z_α and z_β. In the example given in Equation 5.30 the lower boundary would be characterised by $z_\alpha = z_0^{(1)}$ and $z_\beta = z_0^{(3)}$.

Anomalous integration limits. For those sections of a pixel boundary that are outside the shell (limited by z_γ and z_δ), the inner integration limit in Equation 5.31 simplifies to $\phi(y_i, z) = \phi_{\mathrm{an}} = k_i$, where the index "$i$" refers to the upper and lower pixel boundary (y_2 or y_1), and the value of k_i is either 0 or π. In the example given in Equation 5.30, $z_\gamma = z_0^{(2)}$ and $z_\delta = z_0^{(3)}$ for the upper, and $z_\gamma = z_1$ and $z_\delta = z_0^{(1)}$ for the lower pixel boundary. The anomalous part of the integral $N_{1a/b}^{(\mathrm{iso})}$ in Equation 5.31 reads then

$$\begin{aligned} N_{1a}^{(\mathrm{iso})} &= \frac{Q}{4\pi} \int_{z_\gamma}^{z_\delta} \mathrm{d}z\ \phi_{\mathrm{an}}(y_2, z) \\ &= \frac{Q}{4\pi} k_2 \left[z_\delta - z_\gamma\right]. \end{aligned}$$

As for normal boundaries, the solution for the lower pixel boundary, $N_{1b}^{(\mathrm{iso})}$, is analogous to $N_{1a}^{(\mathrm{iso})}$, replacing y_2 by y_1, and having different values for z_γ and z_δ.

5.4 Model Parameters

5.4.1 Image Geometry

The size of the field of view and the resolution of the simulated image can be specified in accordance with the observation with which the simulation is to be compared. The FOV to simulate the WFI image was $34.2' \times 17.1'$ with a pixel size of $4.28''$. The Spitzer images were each simulated with a FOV of $40' \times 20'$ and a resolution of $4.8''$/pixel.

5.4.2 Received Intensity

To simulate the WFI image, the light back-scattered by the dust is assumed to have the same spectral properties as sunlight. In terms of Equation 2.6, the intensity incident on the particle is given by $J_{\rm inc} = I_\odot / r_{\rm h}^2$, with the solar flux at 1 AU $I_\odot$ = 1367 W/m^2, and the heliocentric distance of the particle $r_{\rm h}$ in AU. The scattering area of the particle is given by $\mathrm{d}a = \pi s^2$. The geometric optics approximation is applicable, because for dynamical reasons the particles in the field of view are expected to be much larger than visible wavelengths (Chapter 6). The distance between particle and observer is $r = \Delta$ (in m). The intensity received by the detector from all particles N of sizes s_i in one pixel is therefore

$$J_{\rm rec} = p\, j(\alpha) \frac{I_\odot}{r_{\rm h}^2} \frac{1}{\Delta^2} \sum_i N(s_i) s_i^2. \tag{5.42}$$

The conversion factor c between W/m^2 and ADU of the WFI image is given in Equation 4.7: $c = 2.21 \times 10^{-21}$ W/m^2/ADU.

The Spitzer images are simulated using the monochromatic flux of a blackbody of the equilibrium temperature given by the heliocentric distance at the weighted average wavelength of MIPS24 (23.675 μm). This is consistent with the observations because the measured flux was converted to the equivalent monochromatic flux density at this wavelength by the colour-correction factor for the given blackbody temperature. The assumption that the particles have equilibrium temperature is justified because the particles in the fields of view are expected to be larger than the wavelength (Chapter 6). The intensity per unit frequency interval $J_{\rm rec}^{\rm IR}$ received by a detector at a distance Δ from the N particles of size s_i in a given pixel is described by

$$J_{\rm rec}^{\rm IR} = \frac{\pi}{\Delta^2} B_\nu(\nu, T) \sum_i N(s_i) s_i^2, \tag{5.43}$$

where $\pi s^2 / \Delta^2$ is the solid angle covered by one particle as seen from the detector, and $B_\nu(\nu, T)$ is Planck's function in frequency space

$$B_\nu(\nu, T)\, \mathrm{d}\nu = \frac{2h\nu^3}{c^2} \frac{1}{\mathrm{e}^{h\nu/kT} - 1} \mathrm{d}\nu. \tag{5.44}$$

The flux $J_{\rm rec}^{\rm IR}$ (Equation 5.43) is converted to units of MJy/sr by the factor $10^{20}/\mathrm{d}\omega$ (pixel), where $\mathrm{d}\omega$ (pixel) is the solid angle covered by the pixel and 1 Jy = 10^{-26} W m^{-2} Hz^{-1}.

5.4.3 Orbital Properties and Dynamical Model

The orbital elements of comet 67P/C–G are listed in Section 3.1. The positions of reference dust particles in the model (Section 5.2) are calculated from Keplerian dynamics with modified gravitational potentials to account for radiation pressure. Trail particles emitted after the close encounter of 67P/C–G with Jupiter in 1959 form a narrowly confined stream to date, while older particles were scattered into orbits very different from that of the comet (J. Vaubaillon, private communication). It is therefore assumed that the trail observed along the projected orbit of 67P/C–G consists of particles emitted after 1959 and that the dynamics of these particles *relative to the comet* can be approximated by Keplerian dynamics. The model is not used to calculate an ephemeris of either comet or dust, which cannot be done without taking into account planetary perturbations.

5.4.4 Nucleus Properties

The shape, size, and density of the nucleus are relevant for the employed model of dust emission speeds. The speeds given in Section 5.4.9 were obtained for a spherical nucleus having a radius r_{N} = 2 km and a geometric albedo of 4%. The mass of the nucleus has been estimated to m_{N} = 8 $\times$ 10^{12} kg by Lamy et al. (2006, 2007), which gives an escape speed at the surface of

$$v_{\mathrm{esc}} = \sqrt{2\frac{G\,m_{\mathrm{N}}}{r_{\mathrm{N}}}} = 0.73\,\mathrm{m/s}, \tag{5.45}$$

At 20 km distance from the nucleus centre – where dust grains have decoupled from the accelerating gas – the escape speed is 0.23 m/s.

5.4.5 Comet Activity

The emission of dust from the comet is assumed to be isotropic, concerning both the amount of dust particles produced and their speeds. It is assumed that the comet is active only within 3 AU – where water ice sublimates – corresponding to a time span of 600 days around perihelion during each apparition. Dust emitted during the all seven apparitions since the last close encounter with Jupiter in 1959 is included in the simulation. The dust activity of the comet is assumed not to change between apparitions. The time step to generate dust shells is set to 1 day. The dependence of the dust production rates on heliocentric distance is defined in such a way that the corresponding $Af\rho$ follows the same power law as the observed $Af\rho$. The absolute dust production rate is a variable parameter in order to reproduce the observed trail brightness. The properties of dust particles are not assumed to change after their emission from the nucleus.

5.4.6 Albedo

The geometric albedo of dust is assumed to be independent of wavelength and particle size. Its value is initially set to 4% to generate simulated images. From comparison of the dust production rates needed to reproduce the optical and infrared images, respectively, the albedo is inferred, because the brightness of dust at optical wavelengths is proportional

to the albedo, while the thermal emission is to first order independent of the albedo. (The change in temperature is negligible for albedo variations of a few percent.)

5.4.7 Radiation Pressure

Since only large particles are expected in the FOVs of the images, both $Q_{\rm pr}$ and the bulk density ρ are treated as independent of the particle size s. The radiation pressure coefficient is expressed as

$$\beta(s) = f_\beta \, k_\beta / s. \tag{5.46}$$

f_β is a variable parameter, while k_β = 6.5 $\times$ 10^{-7} corresponds to the β-value given by Gustafson et al. (2001) for astronomical silicate at a mass of 10^{-8} kg, multiplied with the corresponding particle radius for a density of 100 kg/m^3. Since both the material and the density of the particles are a priori unknown, the factor f_β was introduced and is constrained from the reproducibility of the images. Table 5.1 shows the β-values corresponding to f_β = 1 for the dust size classes used in Chapter 6.

Table 5.1: Beta values corresponding to a scaling factor f_β = 1 for the discrete particle sizes employed to generate the images discussed in Chapter 6. The first column contains the index of the size class.

Class index	Size [m]	β ($f_\beta = 1$)
10	1.4×10^{-5}	5.1×10^{-2}
11	3.0×10^{-5}	2.3×10^{-2}
12	6.4×10^{-5}	1.0×10^{-2}
13	1.4×10^{-4}	4.7×10^{-3}
14	3.0×10^{-4}	2.2×10^{-3}
15	6.4×10^{-4}	1.0×10^{-3}
16	1.4×10^{-3}	4.7×10^{-4}
17	3.0×10^{-3}	2.2×10^{-4}
18	6.4×10^{-3}	1.0×10^{-4}
19	1.4×10^{-2}	4.7×10^{-5}
20	3.0×10^{-2}	2.2×10^{-5}

5.4.8 Dust Size Distribution

The differential size distribution of dust particles larger than 10 μm is described by a power law with the variable exponent $-4.3 < \alpha < -3.3$. The size distribution of dust lifted from the nucleus surface is not assumed to change with time, with the exception that the size of the largest liftable grains depends on the heliocentric distance.

For "historical" reasons, the size distribution is specified via a cumulative mass distribution of the shape introduced by Divine and Newburn (1987):

$$F(m) = F_0 \left(\frac{(1+x)^{b-1}}{x^b} \right)^{ac} \text{ with } x = \left(\frac{m}{m_{\rm t}} \right)^{1/c}. \tag{5.47}$$

This function is characterised by different exponents $\gamma = ab$ for light and $\gamma = a$ for heavy particles. m_t is the mass at which the transition between the two exponents takes place, and c determines the sharpness of the transition. By setting $m_\mathrm{t} = 3\,\mu$mit is ensured that all particles expected in the FOVs are in the branch with the exponent $-a$. The exponent for small particles is fixed to $ab = 0.26$, and $c = 2$. The last two parameters are not relevant for the results, because small particles are not expected in the FOV and because the total amount of emitted large dust particles is inferred from the observed surface brightness of the trail. The parameter a is related to the exponent of the differential size distribution via Equation 2.20: $a = -(1+\alpha)/3$.

To represent the size range of dust particles, discrete classes are defined, each containing particles of one mass decade. All particles within a given class are assumed to have the same representative size, the maximum size being 3 cm. The representative sizes depend slightly on the chosen exponent of the size distribution, because they are calculated via the mean mass in the concerned mass interval (Müller, 1999). Exemplary representative sizes used to generate the images in Chapter 6 are listed in Table 5.1.

5.4.9 Dust Emission Speeds

The nucleus is assumed to be a point mass from which the dust particles stream radially away. The initial speeds depend on the particle size and density, and on the heliocentric distance of the comet. The employed emission speeds were derived from the terminal speeds of dust grains in an isotropic hydrodynamic coma model (Müller, 1999), briefly described in Appendix C. The terminal speeds are defined as the speeds of the particles after decoupling from the accelerating gas in the coma. The values obtained with the hydrodynamic coma model for a gas production rate of $Q_\mathrm{gas} = 10^{28}$ molecules/s at perihelion can be approximated by the analytical expression

$$v\left(s,\rho,r_\mathrm{h}\right) = v_0 \left(\frac{s}{s_0}\right)^{-d} \left(\frac{\rho}{\rho_0}\right)^{-d} \left(\frac{r_\mathrm{h}}{r_\mathrm{p}}\right)^{-b(s)}, \tag{5.48}$$

with $v_0 = 3.9$ m/s, $s_0 = 1$ mm, $\rho_0 = 1000$ kg/m^3, and the perihelion distance $r_\mathrm{p} = 1.29$ AU. The value $d = 0.5$ is consistent with earlier models (Divine et al., 1986; Fulle et al., 1995). Since particles with the same cross-section-to-mass ratio reach approximately the same terminal speeds, the ρ-dependence is characterised by the same exponent d as the size dependence. The size-dependent exponent $b(s)$ was introduced to account for deviations from the power law for particles smaller than about 10 μm and larger that about 1 mm. The speeds of small particles are limited by the speed of the gas, which is most relevant close to perihelion. The speeds of large particles deviate from the $\sqrt{1/s}$-dependence due to the stronger relative influence of the gravity of the nucleus, most noticeably at large heliocentric distance. The function $b(s)$ is approximated by a third-order polynomial:

$$b(s) = c_1\,x^3 + c_2\,x^2 + c_3\,x + c_4, \tag{5.49}$$

where $x = \log_{10}\left(s/s_0\right)$, $c_1 = 0.063$, $c_2 = 0.42$, $c_3 = 0.92$, and $c_4 = 2.9$. Physically, the scaling with heliocentric distance is rather one with the assumed decrease in gas production

(Chapter 3).

The bulk density ρ of particles is a free parameter in the model. Instead of varying ρ directly, a scaling factor f_v for the emission speeds is introduced into Equation 5.48, such that the speeds in the simulations are described by

$$v\,(s, \rho{=}100\,\mathrm{kg/m^3}, r_\mathrm{h}) = 12.3\,f_v \left(\frac{s}{s_0}\right)^{-d} \left(\frac{r_\mathrm{h}}{r_\mathrm{p}}\right)^{-b(s)} . \tag{5.50}$$

If Equation 5.50 yields a value v exceeding the speed of the gas in the isotropic coma model at perihelion, it is set to v = v_gas = 750 m/s. The decrease in gas speed with heliocentric distance is small compared with that of the dust speeds and is not taken into account. If the value given by Equation 5.48 is below the escape speed v_esc = 0.23 m/s at the decoupling distance of 20 km from the nucleus centre, the particle is not considered.

5.4.10 Dust Production Rates

The production rate of dust is treated as a variable parameter, derived from the condition that the simulated surface brightness in the trail must reproduce the observed one. Auxiliary production rates $Q_{j,\mathrm{aux}}$ for particles of size s_j are calculated in such a way that the observed $Af\rho\,(r_\mathrm{h})$ is matched for the employed size distribution. Then a scaling factor f_p is introduced to match the simulated to the observed brightness. The dust production rates needed to reproduce the observation are obtained by multiplying the original production rate with the factor f_p. The production rate derived from the optical image is for the initially assumed geometric albedo of 4%. By comparison of the production rates derived from the optical and infrared images, the geometric albedo of the particles is re-evaluated.

The auxiliary production rates $Q_{j,\mathrm{aux}}$ are obtained as follows. If dust of all sizes is liftable from the ground, the production rate $Q_{j,\mathrm{aux}}$ of dust of size s_j is proportional to the relative abundance n_j of such particles in the ground, which is given by the dust size distribution. In general, $Q_{j,\mathrm{aux}} \propto l_j n_j$ where $0 < l_j < 1$ describes the fraction of particles of size s_j liftable from the surface. In the present model, l_j is either 1 or 0 (Section 5.4.9).

The production rate $Q_{j,\mathrm{aux}}$ of dust of the size s_j at a given heliocentric distance is calculated from the observed $Af\rho$-parameter, the particle speed $v\,(s, \rho, r_\mathrm{h})$, the phase angle at the time of observation, the dust geometric albedo, and the relative abundance of particles of class j. From Equation 2.16 an auxiliary $Af\rho$-value is calculated:

$$Af\rho_\mathrm{aux} = 2\pi\,p\,j(\alpha) \sum_j s_j^2\,\frac{n_j\,l_j}{v_j}. \tag{5.51}$$

The auxiliary production rates $Q_{j,\mathrm{aux}}$ are obtained from scaling with the measured value of $Af\rho$:

$$Q_{j,\mathrm{aux}} = n_j\,l_j \frac{Af\rho}{Af\rho_\mathrm{aux}} = n_j\,l_j \frac{Af\rho}{2\pi\,p\,j(\alpha) \sum_j s_j^2\,n_j\,l_j/v_j}. \tag{5.52}$$

In summary, the dust production rates are calculated with two auxiliary steps. They are first adjusted to the $Af\rho$-values measured in the coma (Figure 3.2) and then to the measured surface brightness of the trail.

5.4.11 Summary of Variable Parameters

For the simulations presented in the following chapter, five parameters are variable, and possible values are derived from adjusting the simulated to the observed images:

- The particle emission speeds are given by Equation 5.50, and the scaling factor f_v is varied. From the range of values of f_v found appropriate, the bulk density of the dust grains is inferred (Equation 5.48).
- The radiation pressure coefficient β is described by Equation 5.46 with the variable parameter f_β. With knowledge of the bulk density gained from the emission speeds, the radiation pressure efficiency $Q_{\rm pr}$ can be constrained.
- The size distribution of particles larger than 3 μm is described by a power law with the variable exponent α.
- The dust production rates are set to auxiliary values ensuring that the heliocentric dependence of the dust production rates is in accordance with the power law derived from the observed $Af\rho$. Variable is the scaling factor $f_{\rm p}$, connecting the auxiliary production rates to those needed to reproduce the image.
- The geometric albedo of the dust is set to an initial value of 4%. The measured albedo is derived from the ratio of the scaling factors $f_{\rm p}$ required to reproduce the visible and the infrared observations.

Chapter 6

Results – Comparison of Observation and Simulation

In this chapter, simulated images of the trail of comet 67P/C–G are discussed that were obtained with the model described in Chapter 5. From comparison with the observations presented in Chapter 4, parameters of the model are constrained. The variable parameters are the emission speeds of dust particles, the radiation pressure efficiency, the exponent of the dust size distribution, the geometric albedo of the particles, and the dust production rates (see Section 5.4). Observations and simulations are compared by evaluating (a) the peak surface intensity, (b) the FWHM of the trail – both as functions of distance from the nucleus – and (c) profiles perpendicular to the trail at four positions along the orbit.

The chapter is organised as follows. The spatial distribution of particles of different ages and sizes is discussed exemplarily for one set of parameters in Section 6.1. The impact of separately varying the speed, radiation pressure and size distribution parameters – f_v, f_β, and α – is assessed in Section 6.2. Possible values for these parameters are derived in Section 6.3. From the scaling factors f_p needed to reproduce the optical and infrared observations, the particle albedo is constrained in Section 6.4. The size distribution exponent α and the scaling factors f_p are translated into dust production rates in Section 6.5, and the corresponding $Af\rho$ during emission is compared with published observational data.

6.1 Particle Ages – Trail and Neckline

In Chapter 4 it was found that during all three observations, dust was not only seen along the projected orbit but also outside it. The latter was interpreted as particles having higher β, i. e. being smaller and younger than those found close to the orbit. In the optical image, a splitting of the profile was observed at distances beyond $17'$ from the nucleus (Figure 4.3d).

To get an overview of the spatial distribution of particle ages and sizes, simulated images have been generated for sub-populations of dust grains with the parameters f_v = 1, f_β = 3, and $\alpha = -3.9$. These values were chosen with knowledge of the results discussed in the subsequent sections, but for the geometrical discussion in this section their precise

values are not relevant.

The top panels in Figures 6.1 to 6.3 show simulated images for the dates and geometrical conditions of the three observations. The remaining three panels of each figure display dust emitted between 1962 and 1996 (the old trail), dust emitted around a comet true anomaly of -180° before the observation (the neckline), and dust emitted during the remaining time of the 2002/03 apparition. Profiles perpendicular to the projected orbit are depicted in Figure 6.4 for the three dust populations discriminated in Figures 6.1 to 6.3 and for their sum.

The simulated images (Figures 6.1 to 6.3) exhibit a splitting of the dust near the orbit as seen in the WFI data. The grains emitted before the 2002/03 apparition (Panels b) are concentrated close to the projected orbit of the comet. Panels (c) show that the narrow central parts of the second peaks are due to particles emitted at a true anomaly of -180° before the observation, hence these peaks are the neckline at the concerned observation dates. Particles emitted at other times during the 2002/03 apparition are more widely distributed behind the orbit (viewed in three dimensions), causing the shallower profile on the young-particle side of the trail. Figure 6.4 confirms that the northern peaks (positive distance from the projected orbit) in the WFI and Spitzer 2006 images are formed by particles stemming from apparitions before 2002, while the southern peak is due to particles emitted in 2002. In the Spitzer 2005 image this is reversed, because the observer was located below the comet orbital plane in 2004 and 2006, and above it in 2005 (Table 4.1). The separation between old trail and neckline at $30'$ behind the nucleus is $25''$ in 2004, $39''$ in 2005, and $19''$ in 2006 (Figure 6.4). The corresponding differences in position angle are $(-0.8 \pm 0.14)^\circ$ in 2004, $(+1.24 \pm 0.15)^\circ$ in 2005, and $(-0.60 \pm 0.15)^\circ$ in 2006, where the uncertainty results from the pixel scale employed for the simulations. In the 2005 simulation, the old trail encloses an angle of $(0.25 \pm 0.15)^\circ$ with the projected velocity vector. The position angle of the projected velocity vector predicted from the simulation is consistent with the JPL ephemeris and with the observation. There is no obvious geometrical reason that image distortions are more severe for the 2005 observation than for the 2004 and 2006 images (Table 4.1). Hence the angle between the old trail and the projected velocity vector in the simulation for 2005 remains unexplained.

In the observational data, the splitting of old trail and neckline is seen in the WFI image (Figure 4.3d), but not in the Spitzer images. For 2006, this can be due to the lower resolution of the Spitzer image ($2.5''$/pixel and a PSF with FWHM of about $6''$ for the MIPS24 instrument compared with $0.7''$/pixel and seeing on the order of $1''$ for WFI). In the 2005 Spitzer image, trail and neckline are separated by $39''$ at $30'$ distance from the nucleus. This separation is resolvable with MIPS24. But because of the missing shadow observation, the data quality is too poor at present to decide whether or not the splitting has been observed. This may change once the shadow data are evaluated.

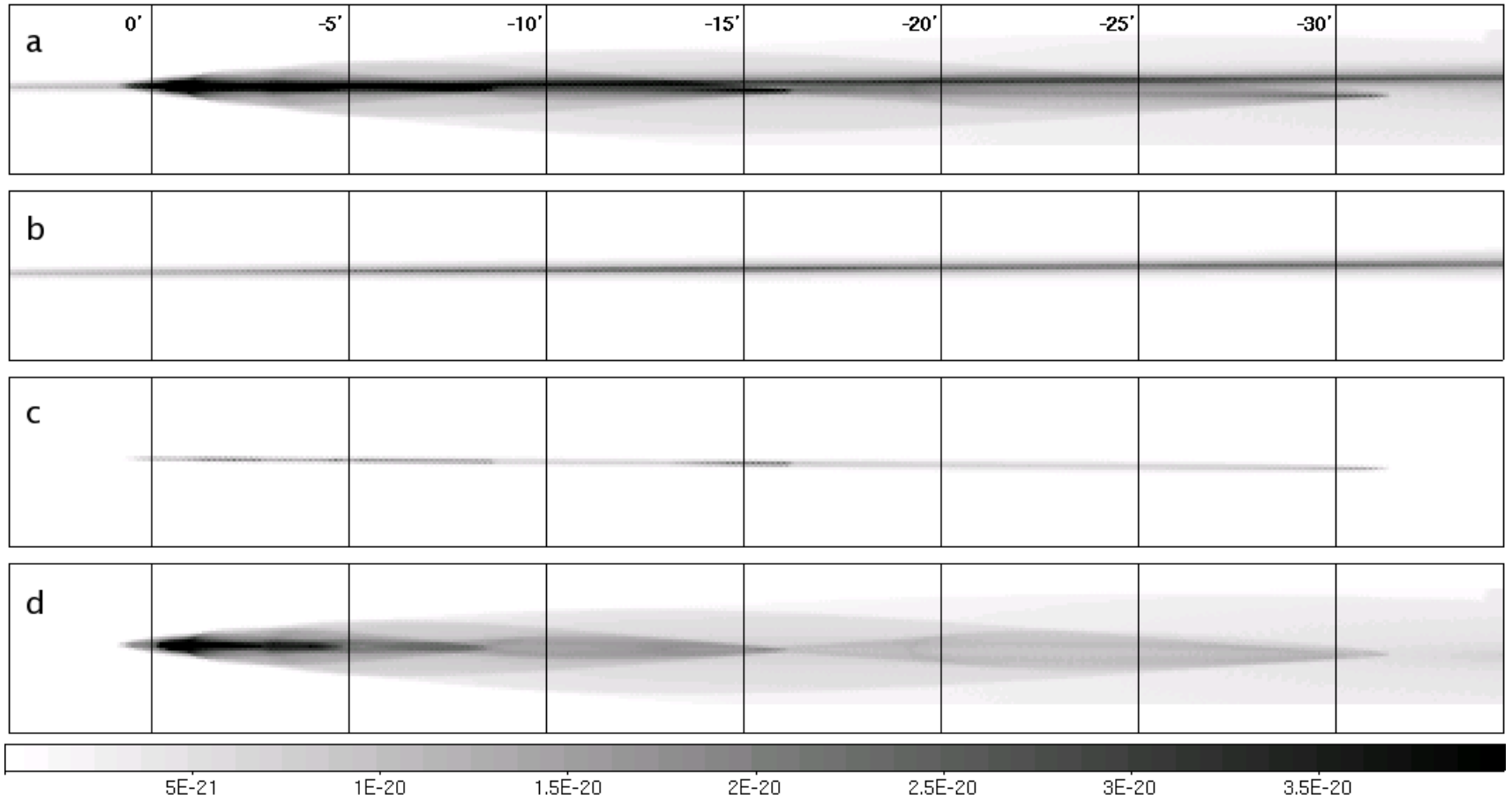

Figure 6.1: Simulated images with $\alpha = -3.9$, $f_\beta = 3$, and $f_v = 1$ for the date and geometrical conditions of the WFI 2004 observation (Section 4.1) before flatfielding and spatial averaging. The projected velocity vector of the comet encloses an angle of 0.4° with the x-axis. The vertical lines indicate the distance from the nucleus, and the intensity scale is linear but not matched to the observation. **a)** Dust emitted during the last seven perihelion passages. **b)** The old trail: dust emitted during the six apparitions before the last one in 2002/03 and after the Jupiter encounter 1959. **c)** The neckline: dust emitted during a time interval of ± 10 days around the date when the comet was at a true anomaly of $-180°$ before the observation (Table 4.1). **d)** Dust emitted during the 2002/03 apparition without the neckline contribution.

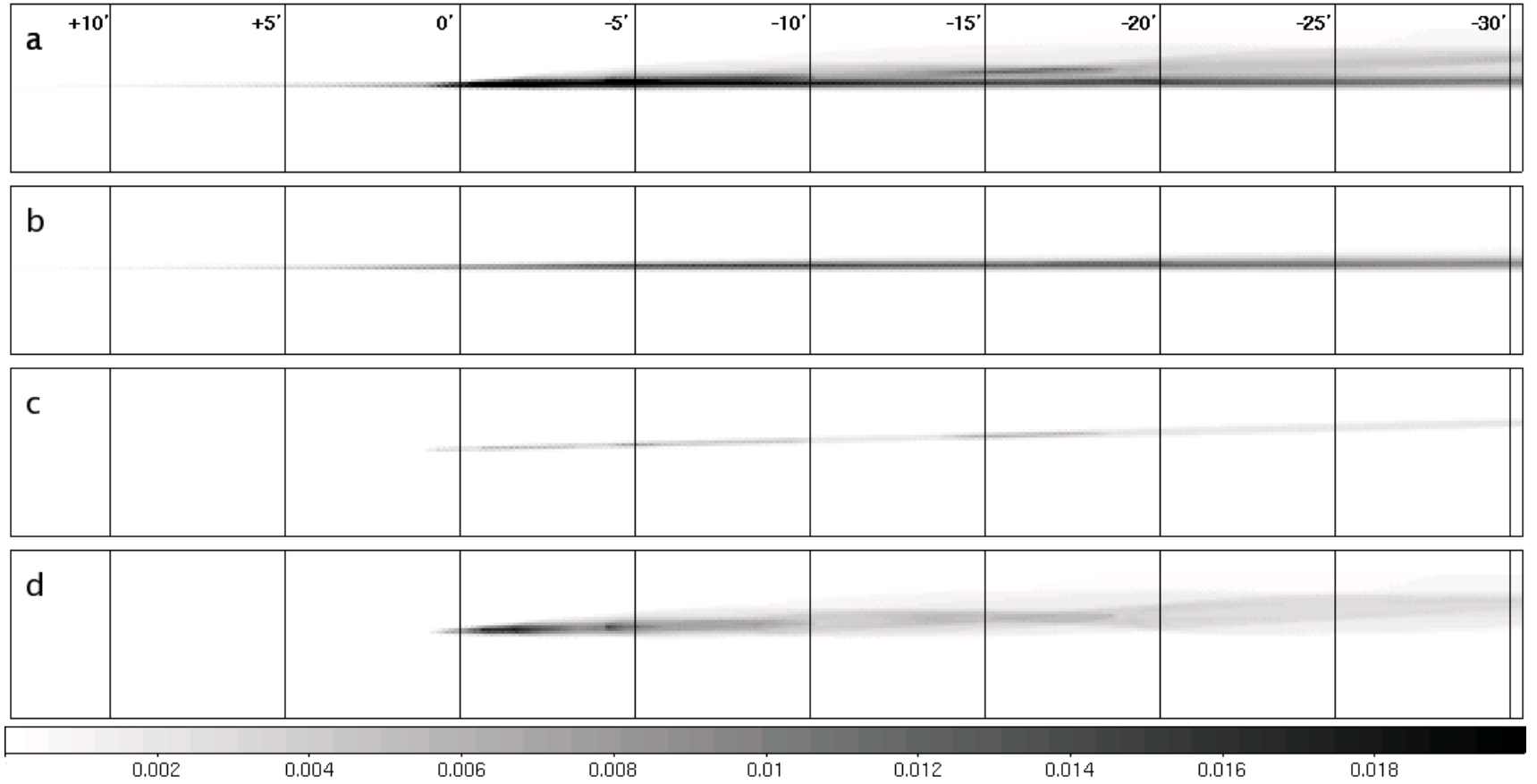

Figure 6.2: Simulated images with $\alpha = -3.9$, $f_\beta = 3$, and $f_v = 1$ for the date and geometrical conditions of the Spitzer 2005 observation (Section 4.2.3). The x-axis is aligned with the projected velocity vector of the comet. The vertical lines indicate the distance from the nucleus, and the intensity scale is linear but not matched to the observation. **a)** Dust emitted during the last seven perihelion passages. **b)** The old trail: dust emitted during the six apparitions before the last one in 2002/03 and after the Jupiter encounter 1959. **c)** The neckline: dust emitted during a time interval of ± 10 days around the date when the comet was at a true anomaly of -180° before the observation (Table 4.1). **d)** Dust emitted during the 2002/03 apparition without the neckline contribution.

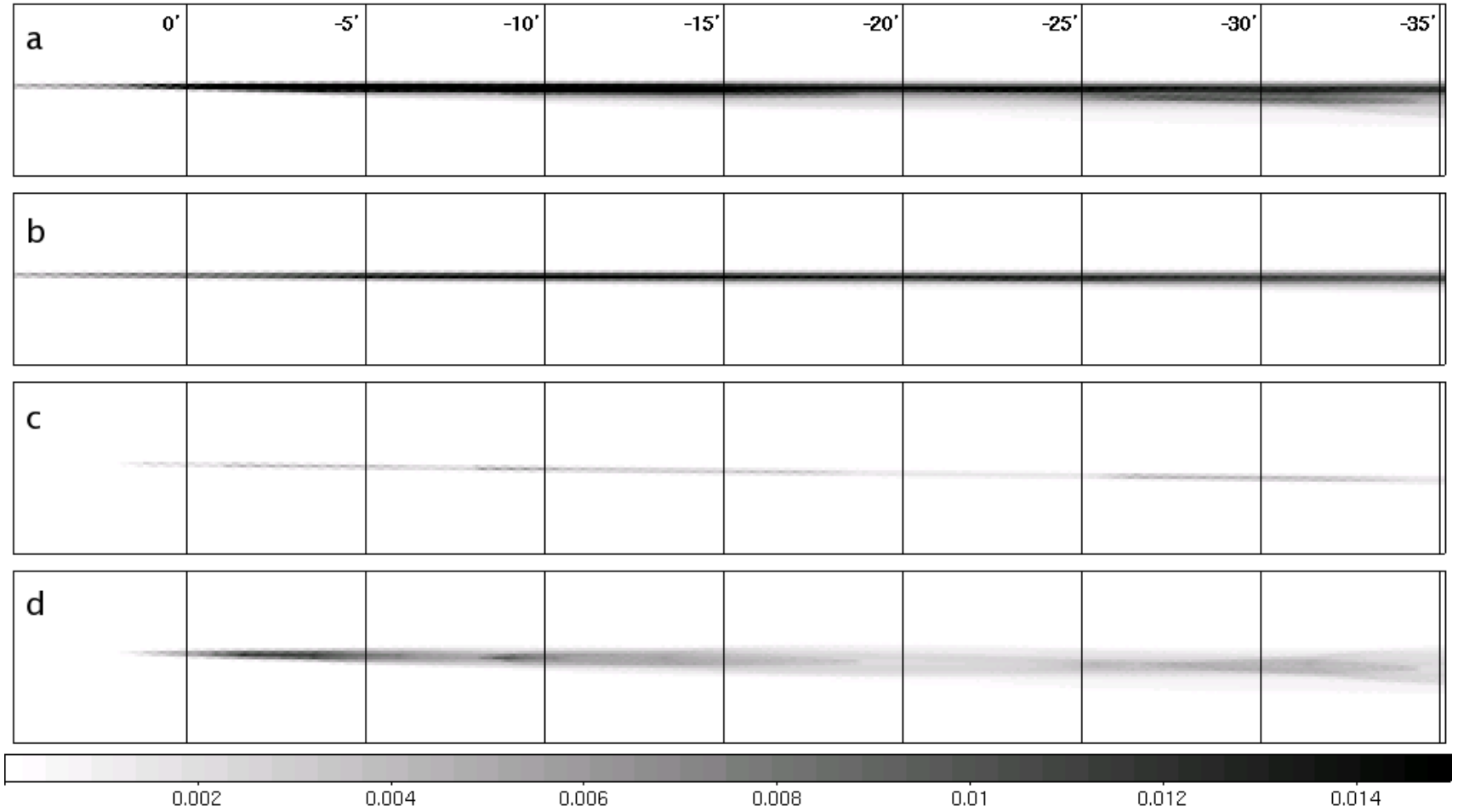

Figure 6.3: Simulated images with $\alpha = -3.9$, $f_\beta = 3$, and $f_v = 1$ for the date and geometrical conditions of the Spitzer 2006 observation (Section 4.2.4). The x-axis is aligned with the projected velocity vector of the comet. The vertical lines indicate the distance from the nucleus, and the intensity scale is linear but not matched to the observation. **a)** Dust emitted during the last seven perihelion passages. **b)** The old trail: dust emitted during the six apparitions before the last one in 2002/03 and after the Jupiter encounter 1959. **c)** The neckline: dust emitted during a time interval of ± 10 days around the date when the comet was at a true anomaly of -180° before the observation (Table 4.1). **d)** Dust emitted during the 2002/03 apparition without the neckline contribution.

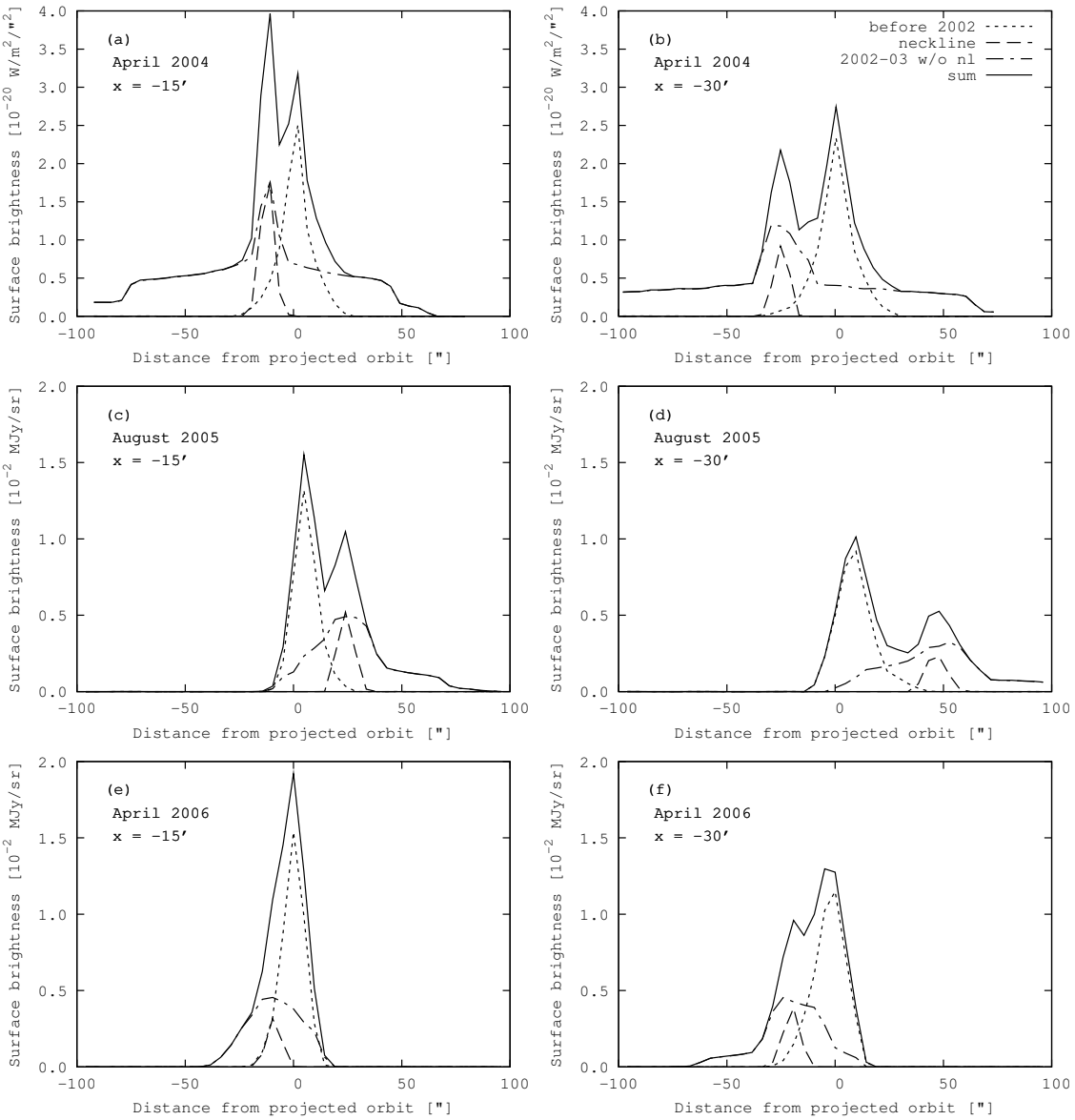

Figure 6.4: Profiles perpendicular to the x-axes at 15′ and 30′ behind the nucleus in Figures 6.1 to 6.3, the intensity was not scaled to match the observations. Solid, short-dashed, long-dashed, and dash-dotted lines correspond to Panels (a) to (d), respectively. **a)** and **b)** Profiles derived from Figure 6.1 (WFI, 2004). **c)** and **d)** Profiles derived from Figure 6.2 (Spitzer 2005). **e)** and **f)** Profiles derived from Figure 6.3 (Spitzer 2006).

Figures 6.5 to 6.7 show the distribution of particles of different sizes and emission times as a function of distance from the nucleus. The images were generated with the same model parameters as Figures 6.1 to 6.4. The smallest particles present in any of the FOVs are of size class 13 (s = 0.14 mm), emitted in 2002/03 (Figure 6.5). With the scaling factor f_β = 3, this size corresponds to a radiation pressure parameter β = 0.014. For f_β = 1, the minimum size of particles in the FOV is s = 60 μm (class 12, see Table 5.1).

The horizontal extensions of the coloured bars in Figures 6.5 to 6.7 demonstrate that in the old trail, particles of a given size class are more widely distributed than the corresponding particles emitted in 2002/03. Particle sizes in the old trail range from 3 cm near the nucleus to 3 mm at 30′ behind it. The major contribution to the surface brightness in the old trail stems from the two apparitions before last (i. e. 1988-90 and 1995-96). The dominant size of particles emitted in 2002/03 depends more strongly on the distance from the nucleus. At 15′ behind the nucleus, the neckline is dominated by particles on the order of 0.1 to 1 mm. With the parameters (f_v = 1 and f_β = 3) used for this simulation, the brightness bulge closely behind the nucleus must be due to particles with sizes on the order of 1 cm, because smaller particles are more widely spread along the orbit. To reproduce the observed relative brightness of trail and neckline sets a constraint on the ratio of mm-sized to cm-sized particles in the dust size distribution.

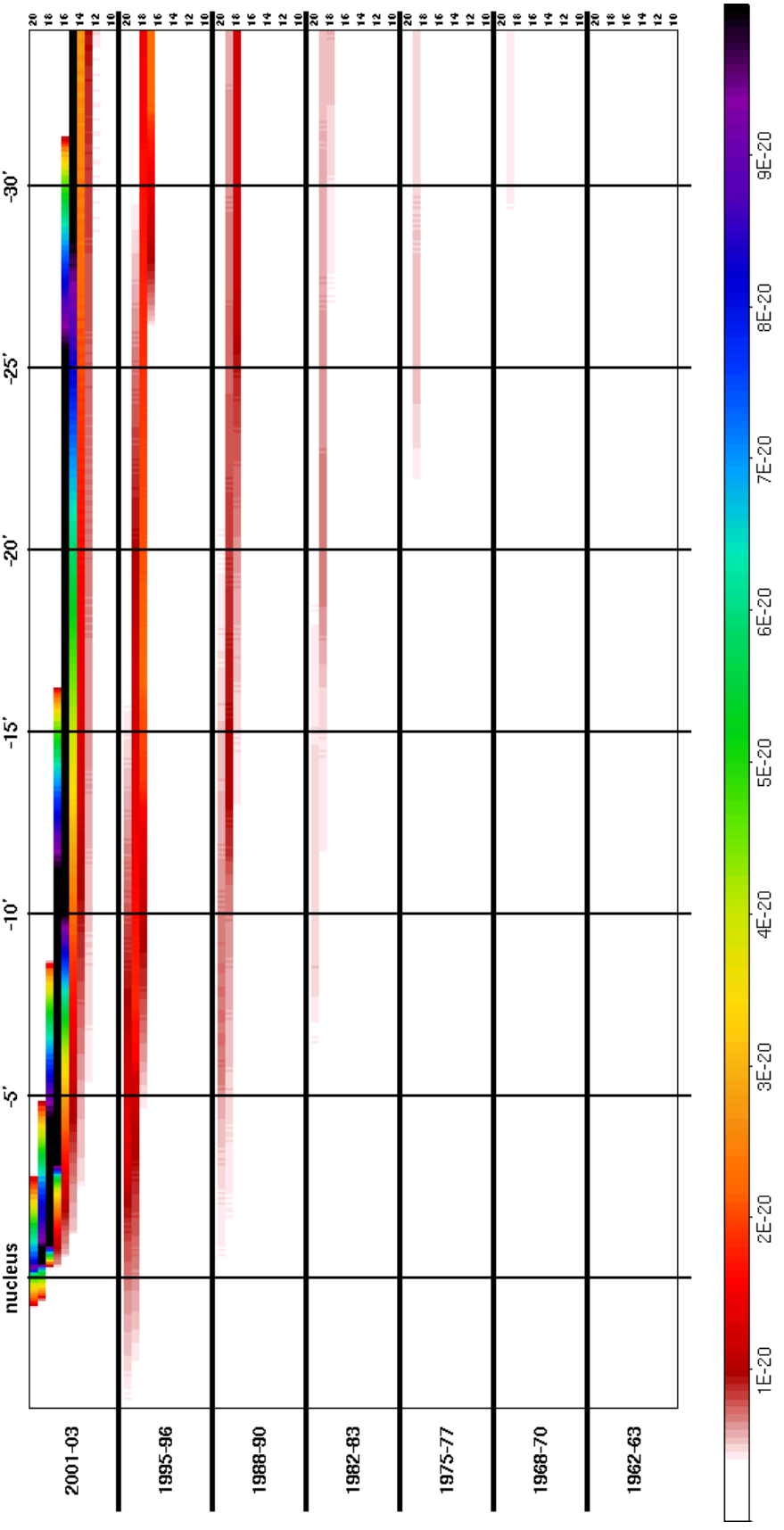

Figure 6.5: Distribution of particles of different sizes and emission times as a function of distance from the nucleus, simulated for the WFI 2004 observation and $\alpha = -3.9$, $f_\beta = 3$, and $f_v = 1$ (Figure 6.1). Each line shows colour-coded the integral over a perpendicular profile through an image generated for dust of a single size class and originating from a single apparition, at the nucleus distance indicated at the upper margin. The index of the size class is given at the right margin, the corresponding particle sizes are listed in Table 5.1. The emission time is indicated at the left margin. The figure focuses on the dimension along the orbit. The relative brightness of the lines is not representative of the relative surface brightness of the concerned dust population due to the integration over the perpendicular dimension. The colour scale is not matched to the observation.

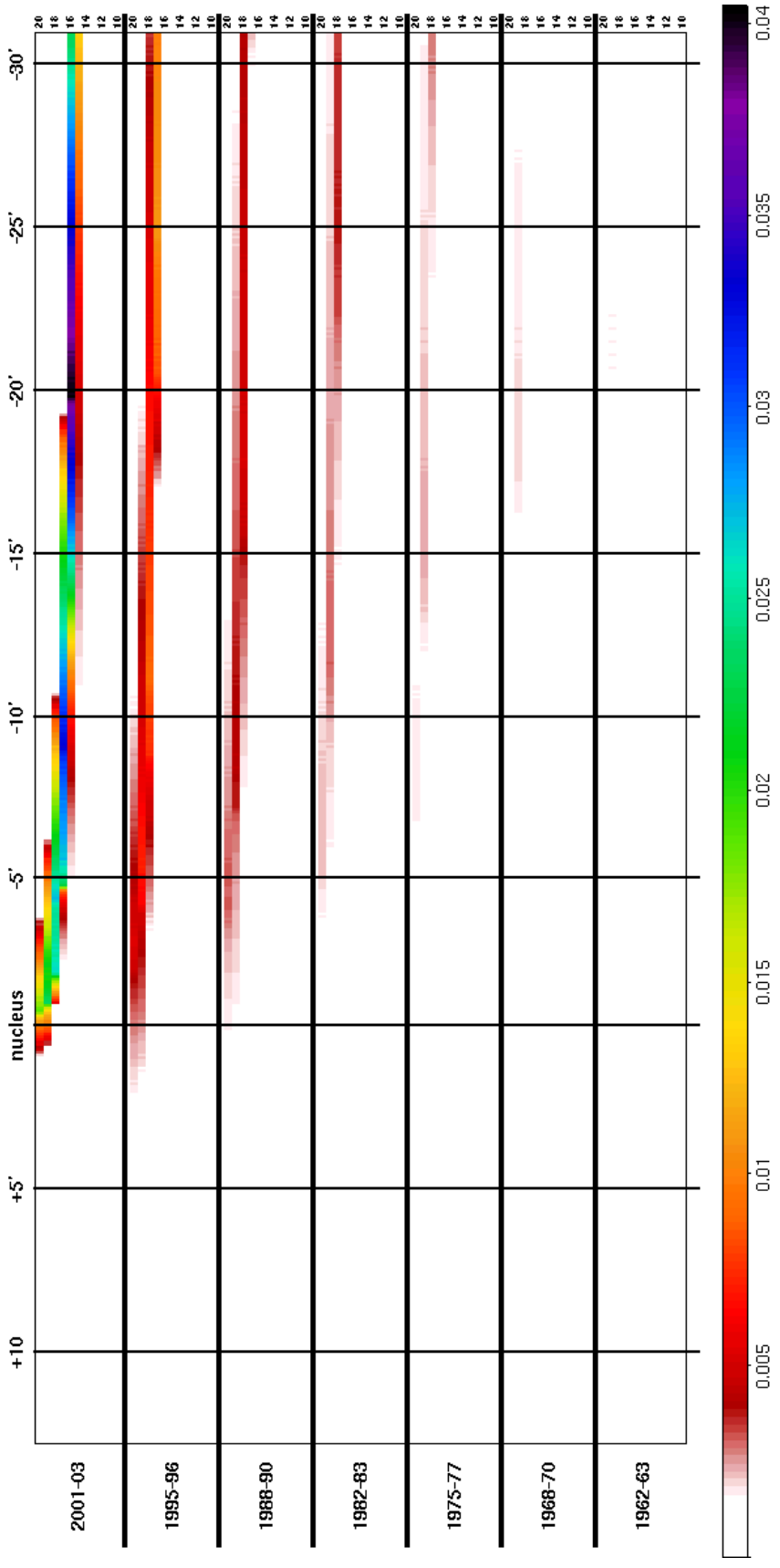

Figure 6.6: Distribution of particles of different sizes and emission times as a function of distance from the nucleus, simulated for the Spitzer 2005 observation and $\alpha = -3.9$, $f_\beta = 3$, and $f_v = 1$ (Figure 6.3). Each line shows colour-coded the integral over a perpendicular profile through an image generated for dust of a single size class and originating from a single apparition, at the nucleus distance indicated at the upper margin. The index of the size class is given at the right margin, the corresponding particle sizes are listed in Table 5.1. The emission time is indicated at the left margin. The figure focuses on the dimension along the orbit. The relative brightness of the lines is not representative of the relative surface brightness of the concerned dust population due to the integration over the perpendicular dimension. The colour scale is not matched to the observation.

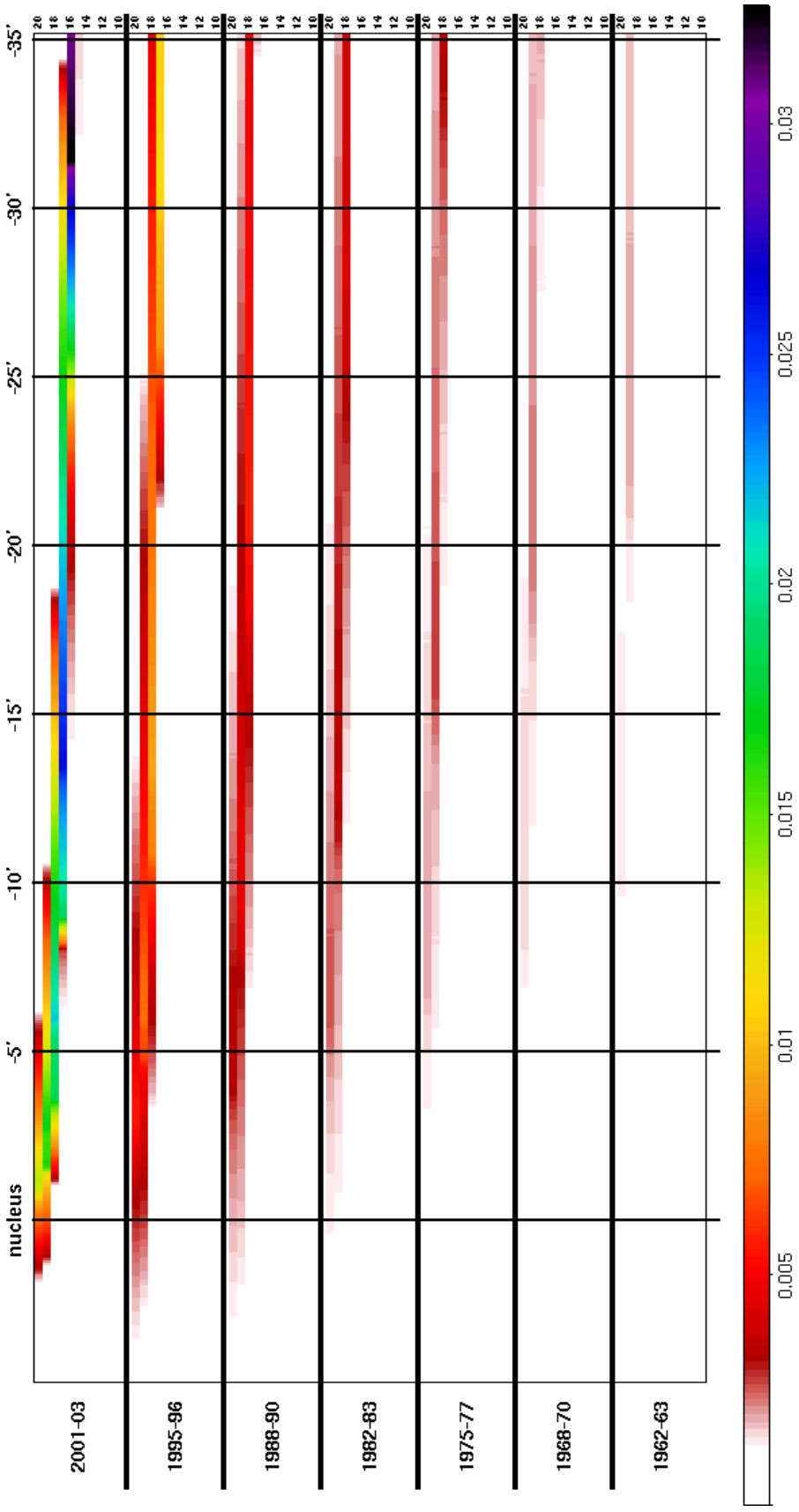

Figure 6.7: Distribution of particles of different sizes and emission times as a function of distance from the nucleus, simulated for the Spitzer 2006 observation and $\alpha = -3.9$, $f_\beta = 3$, and $f_v = 1$ (Figure 6.3). Each line shows colour-coded the integral over a perpendicular profile through an image generated for dust of a single size class and originating from a single apparition, at the nucleus distance indicated at the upper margin. The index of the size class is given at the right margin, the corresponding particle sizes are listed in Table 5.1. The emission time is indicated at the left margin. The figure focuses on the dimension along the orbit. The relative brightness of the lines is not representative of the relative surface brightness of the concerned dust population due to the integration over the perpendicular dimension. The colour scale is not matched to the observation.

6.2 Variation of the Parameters f_v, f_β, and α

Figures 6.8 to 6.10 show simulated trail profiles for varying scaling factors f_v of the emission speeds. Increasing the emission speeds has three major consequences for the dust distribution. (1) The extension perpendicular to the orbit increases with the emission speeds. (2) Correspondingly, the surface brightness of the profiles decreases, expressed in increasing scaling factors f_p for the production rates. (3) The bright bulge closely behind the nucleus becomes wider and flatter, and the steep flank ahead of the nucleus moves to the left.

Figures 6.11 to 6.13 show profiles obtained with different values of the radiation pressure factor f_β (Section 5.4.7). With increasing β, particles are separated from the nucleus more quickly. Hence the observed bulge behind the nucleus shifts towards the trailing direction (to the right in the images). The FWHM of the trail decreases slightly, because at a given nucleus distance, larger particles are found that were emitted with lower speeds. The FWHM depends on the radiation pressure parameter less than on the emission speed. No clear correlation is found between the relative brightness of old and young particles in the perpendicular profiles in Panels (c) to (f) on the one hand, and either f_v or f_β on the other hand.

Figures 6.14 to 6.19 show the results of varying the exponent of the differential size distribution $-4.3 < \alpha < -3.3$ for f_v = 0.5 and f_β = 1 (Figures 6.14 to 6.16), and f_v = 1 and f_β = 3 (Figures 6.17 to 6.19). The perpendicular profiles in Panels (c) to (f) show that α governs the relative brightness of the old trail and the particles emitted during the 2002/03 apparition. The surface brightness far from the nucleus compared with the bulge near the nucleus increases for smaller values of α (Panels a) because of the higher contribution from small particles, evident from the perpendicular profiles (c) to (f). In contrast, the relative brightness of the old trail and the bulge behind the nucleus depends little on the size distribution, because both are dominated by particles of the same size. The FWHM of the trail increases with decreasing α, also because of the higher relative contribution of the more widely distributed young particles. The position of the bulge behind the nucleus is not affected by α, because this peak is dominated by the large particles for all considered size distributions.

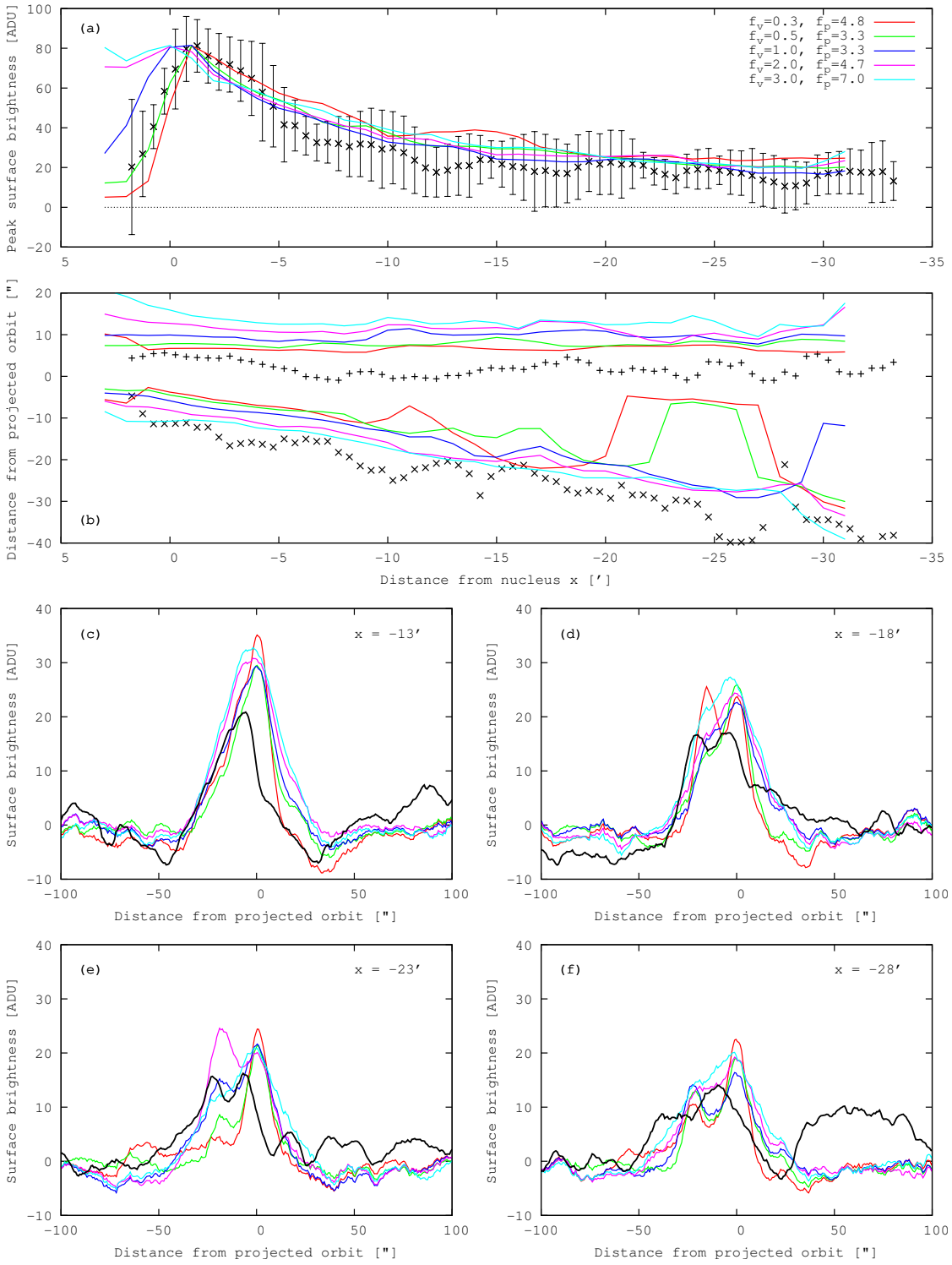

Figure 6.8: Surface brightness and FWHM of the trail in April 2004 for varying emission speeds. Black: WFI observation. Coloured: Simulation (with flatfield and averaging filter) for $\alpha = -3.9$ and $f_\beta = 1$. The scaling factors for the speeds, f_v, and production rates, f_p, are listed in Panel (a). **a)** Peak surface brightness as a function of distance from the nucleus. **b)** FWHM of the trail. "+" and "x" indicate the sides dominated by the old trail and particles from the last apparition, respectively. **c) - f)** Perpendicular profiles at 13′, 18′, 23′, and 28′ behind the nucleus. The mismatch between observed and simulated orbit distances is attributed to inaccurate orientation of the WFI image.

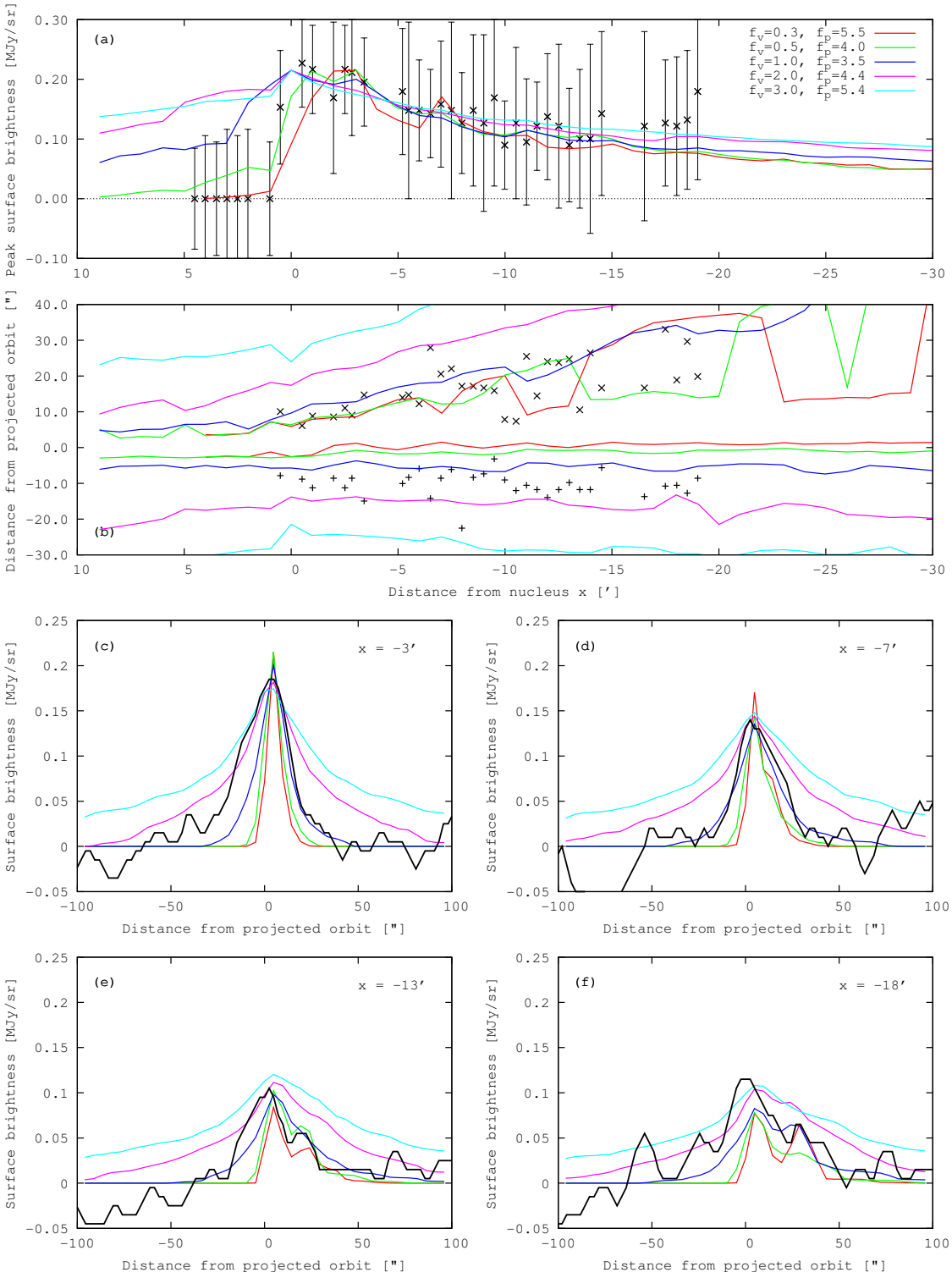

Figure 6.9: Surface brightness and FWHM of the trail in August 2005 for varying emission speeds. Black: Spitzer observation. Coloured: Simulated data for $\alpha = -3.9$ and $f_\beta = 1$. The scaling factors for the speeds, f_v, and production rates, f_p, are listed in Panel (a). **a)** Peak surface brightness as a function of distance from the nucleus. **b)** FWHM of the trail. "+" and "x" indicate the sides dominated by the old trail and particles from the last apparition, respectively. **c) - f)** Perpendicular profiles at 3′, 7′, 13′, and 18′ behind the nucleus.

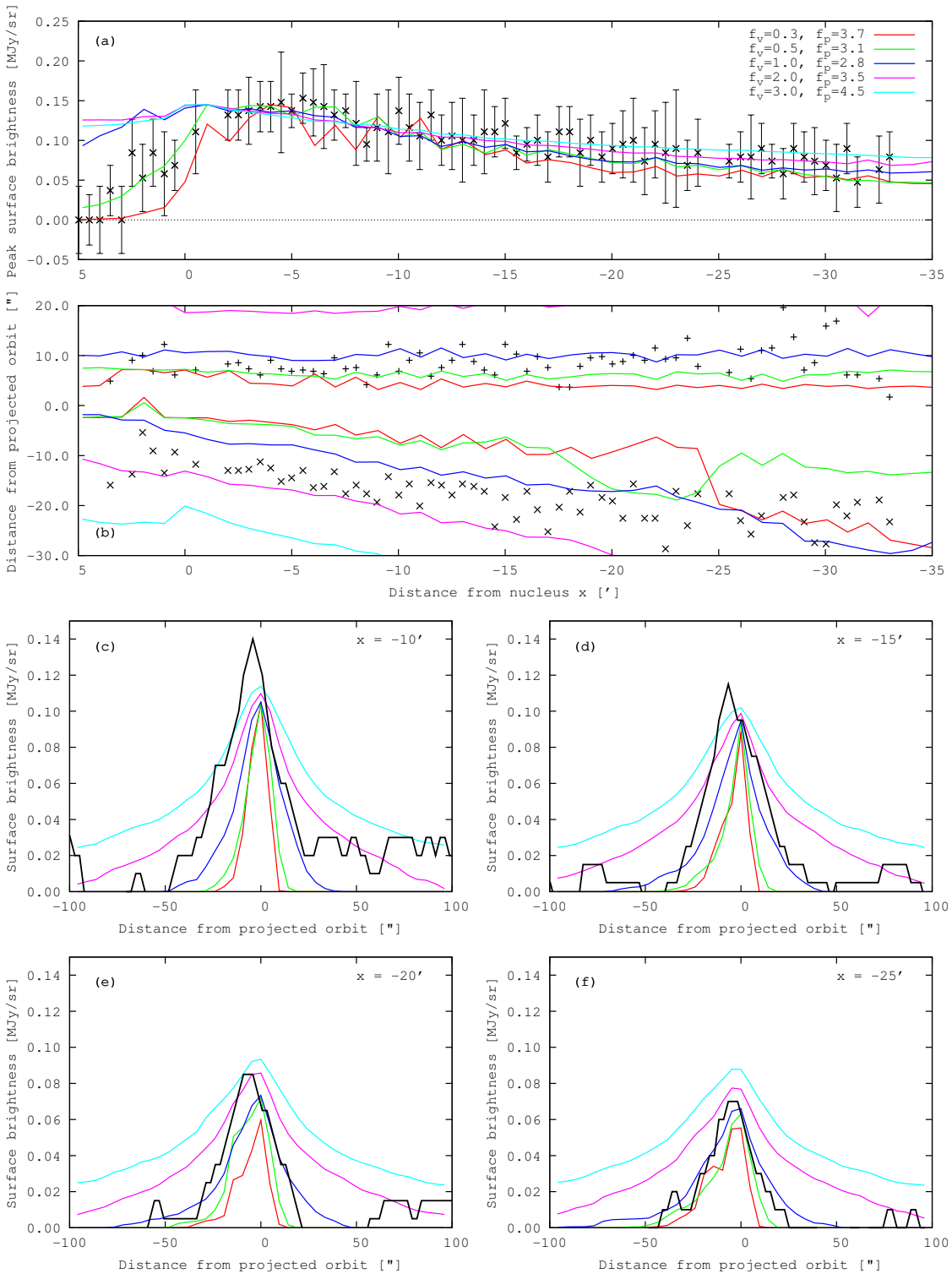

Figure 6.10: Surface brightness and FWHM of the trail in April 2006 for varying emission speeds. Black: Spitzer observation. Coloured: Simulated data for $\alpha = -3.9$ and $f_\beta = 1$. The scaling factors for the speeds, f_v, and production rates, f_p, are listed in Panel (a). **a)** Peak surface brightness as a function of distance from the nucleus. **b)** FWHM of the trail. "+" and "x" indicate the sides dominated by the old trail and particles from the last apparition, respectively. **c) - f)** Perpendicular profiles at 10′, 15′, 20′, and 25′ behind the nucleus.

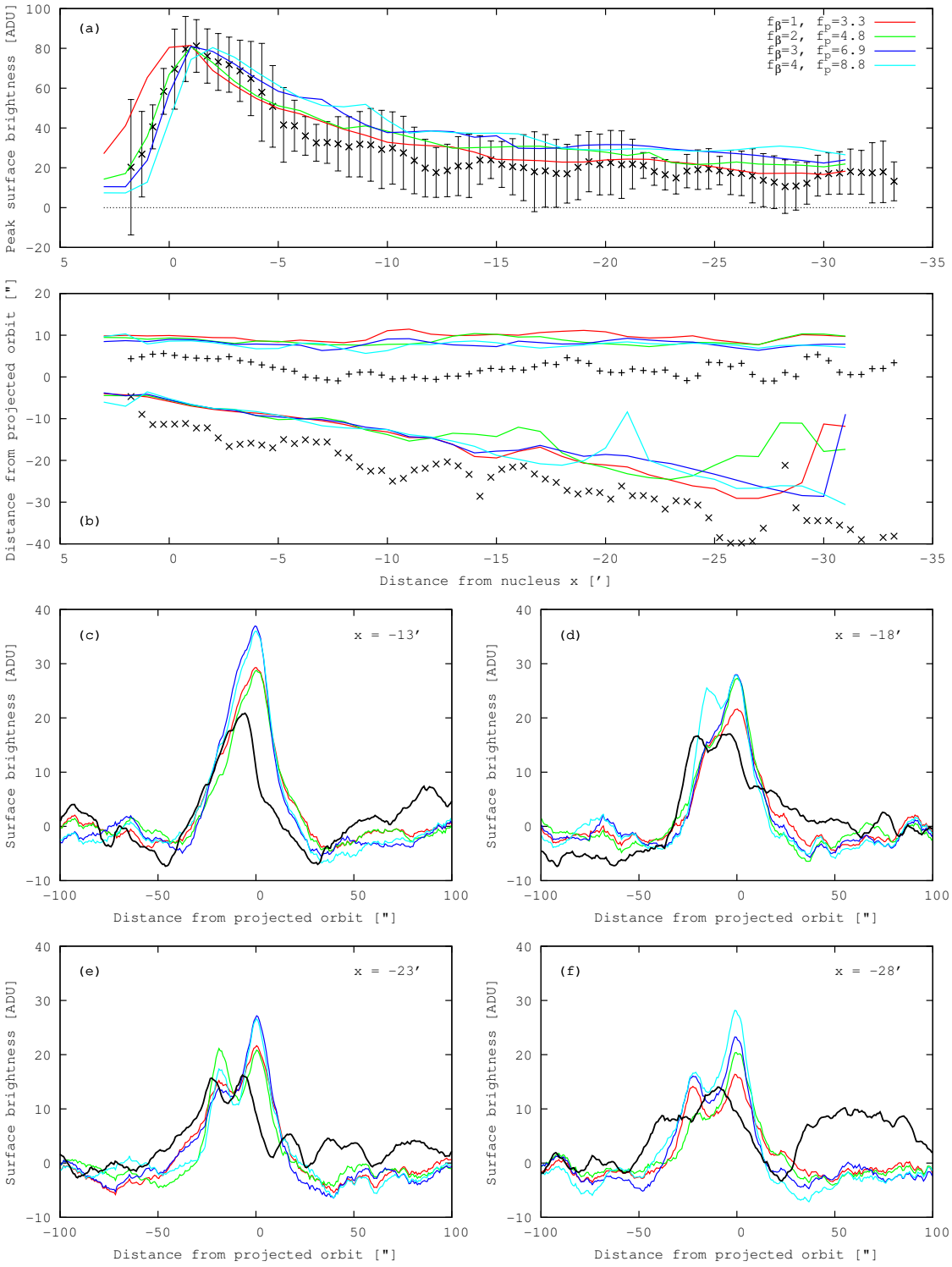

Figure 6.11: Surface brightness and FWHM of the trail in April 2004 for varying radiation pressure force. Black: WFI observation. Coloured: Simulation (with flatfield and averaging filter) for $\alpha = -3.9$ and $f_v = 1$. The scaling factors for the radiation pressure, f_β, and production rates, f_p, are listed in Panel (a). **a)** Peak surface brightness as a function of distance from the nucleus. **b)** FWHM of the trail. "+" and "x" indicate the sides dominated by the old trail and particles from the last apparition, respectively. **c) - f)** Perpendicular profiles at 13′, 18′, 23′, and 28′ behind the nucleus. The mismatch between observed and simulated orbit distances is attributed to inaccurate orientation of the WFI image.

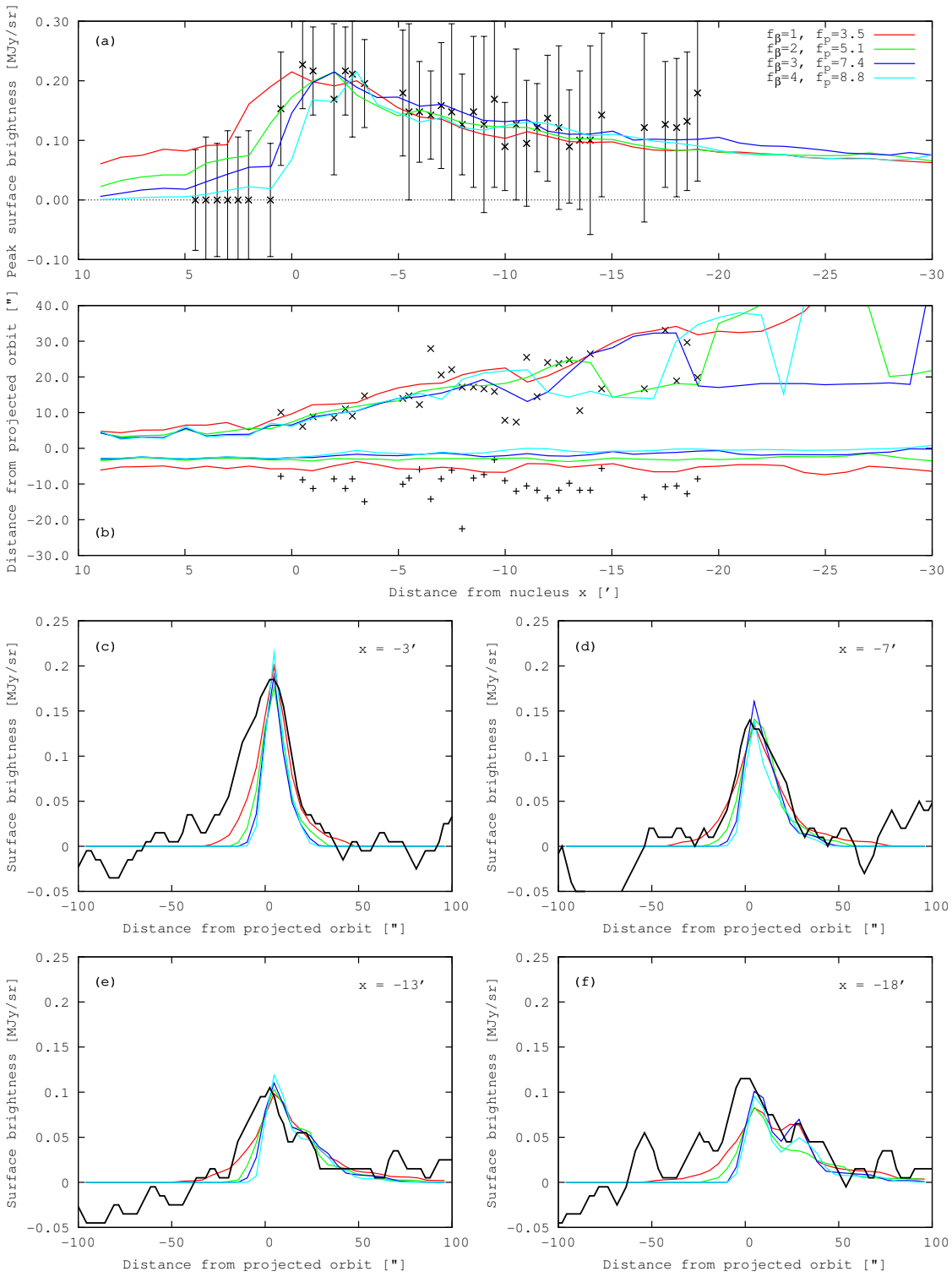

Figure 6.12: Surface brightness and FWHM of the trail in August 2005 for varying radiation pressure force. Black: Spitzer observation. Coloured: Simulated data for $\alpha = -3.9$ and $f_v = 1$. The scaling factors for the radiation pressure, f_β, and production rates, f_p, are listed in Panel (a). **a)** Peak surface brightness as a function of distance from the nucleus. **b)** FWHM of the trail. "+" and "x" indicate the sides dominated by the old trail and particles from the last apparition, respectively. **c) - f)** Perpendicular profiles at 3′, 7′, 13′, and 18′ behind the nucleus.

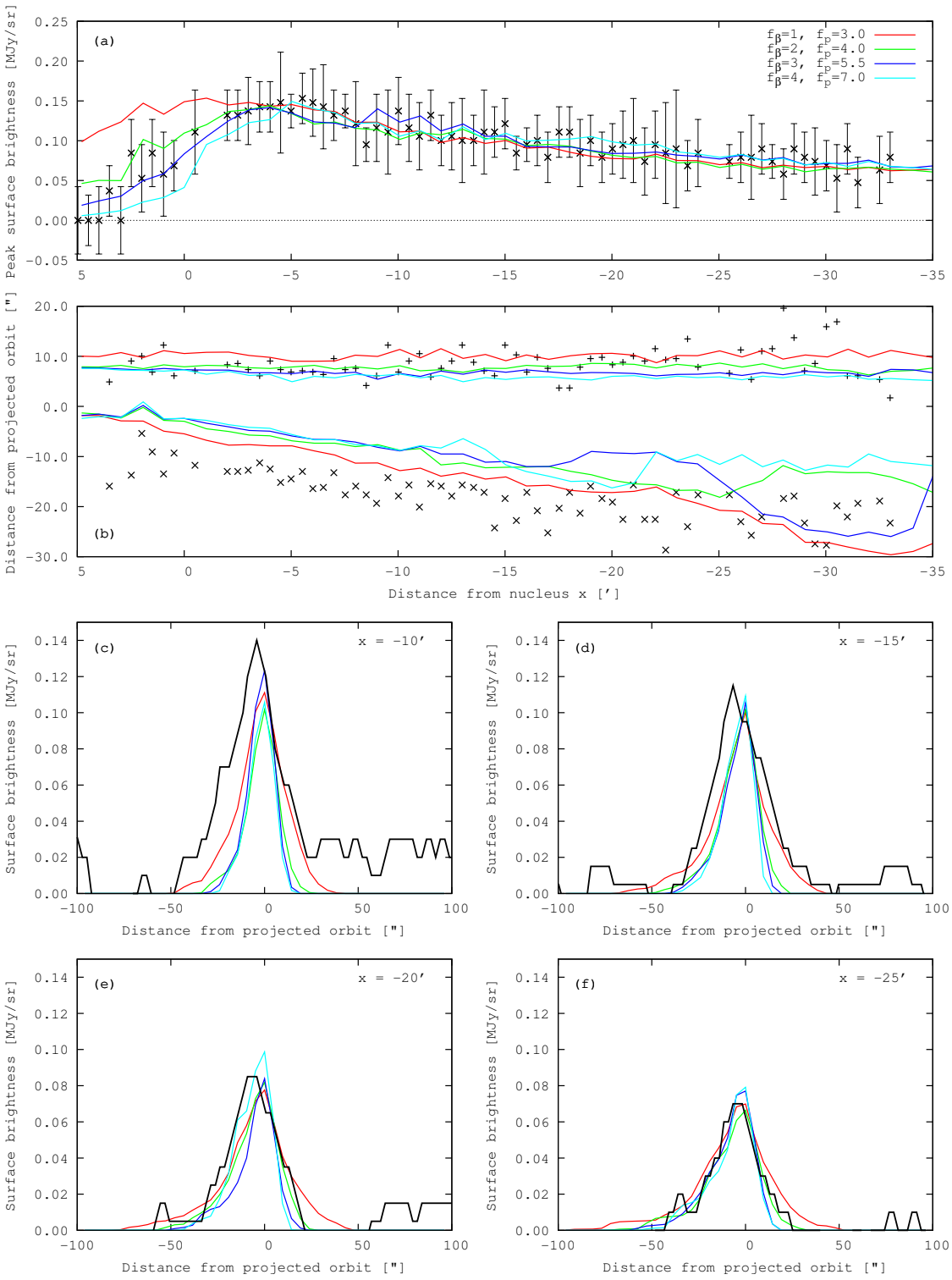

Figure 6.13: Surface brightness and FWHM of the trail in April 2006 for varying radiation pressure force. Black: Spitzer observation. Coloured: Simulated data for $\alpha = -3.9$ and $f_v = 1$. The scaling factors for the radiation pressure, f_β, and production rates, f_p, are listed in Panel (a). **a)** Peak surface brightness as a function of distance from the nucleus. **b)** FWHM of the trail. "+" and "x" indicate the sides dominated by the old trail and particles from the last apparition, respectively. **c) - f)** Perpendicular profiles at 10′, 15′, 20′, and 25′ behind the nucleus.

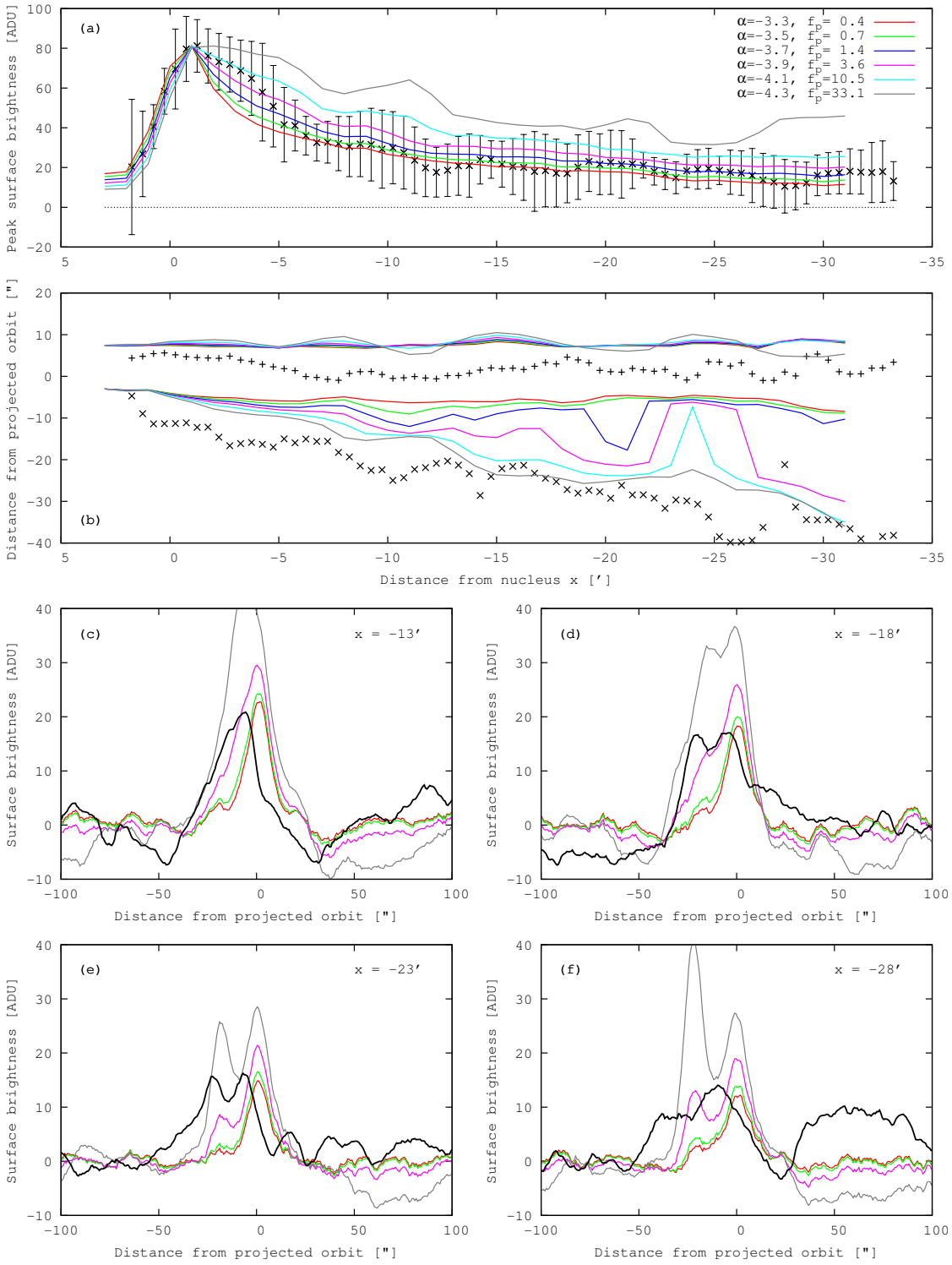

Figure 6.14: Surface brightness and FWHM of the trail in April 2004 for varying size distribution exponent. Black: WFI observation. Coloured: Simulation (with flatfield and averaging filter) for f_v = 0.5 and f_β = 1. The size distribution exponent, α, and production rate scaling factor, f_p, are listed in Panel (a). **a)** Peak surface brightness as a function of distance from the nucleus. **b)** FWHM of the trail. "+" and "x" indicate the sides dominated by the old trail and particles from the last apparition, respectively. **c) - f)** Perpendicular profiles at 13′, 18′, 23′, and 28′ behind the nucleus. The mismatch between observed and simulated orbit distances is attributed to inaccurate orientation of the WFI image.

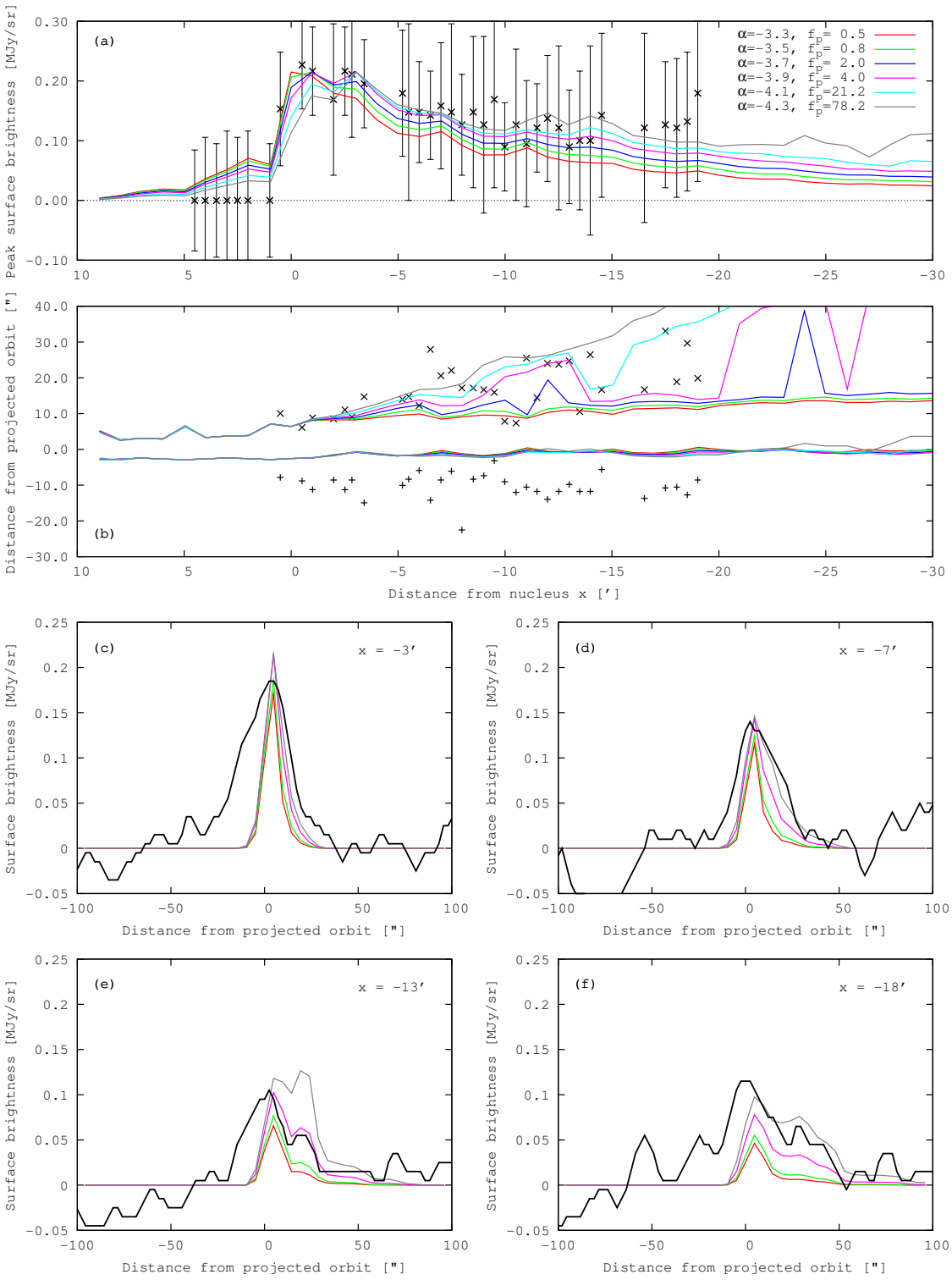

Figure 6.15: Surface brightness and FWHM of the trail in August 2005 for varying size distribution exponent. Black: Spitzer observation. Coloured: Simulated data for f_v = 0.5 and f_β = 1. The size distribution exponent, α, and production rate scaling factor, f_p, are listed in Panel (a). **a)** Peak surface brightness as a function of distance from the nucleus. **b)** FWHM of the trail. "+" and "x" indicate the sides dominated by the old trail and particles from the last apparition, respectively. **c) - f)** Perpendicular profiles at 3′, 7′, 13′, and 18′ behind the nucleus.

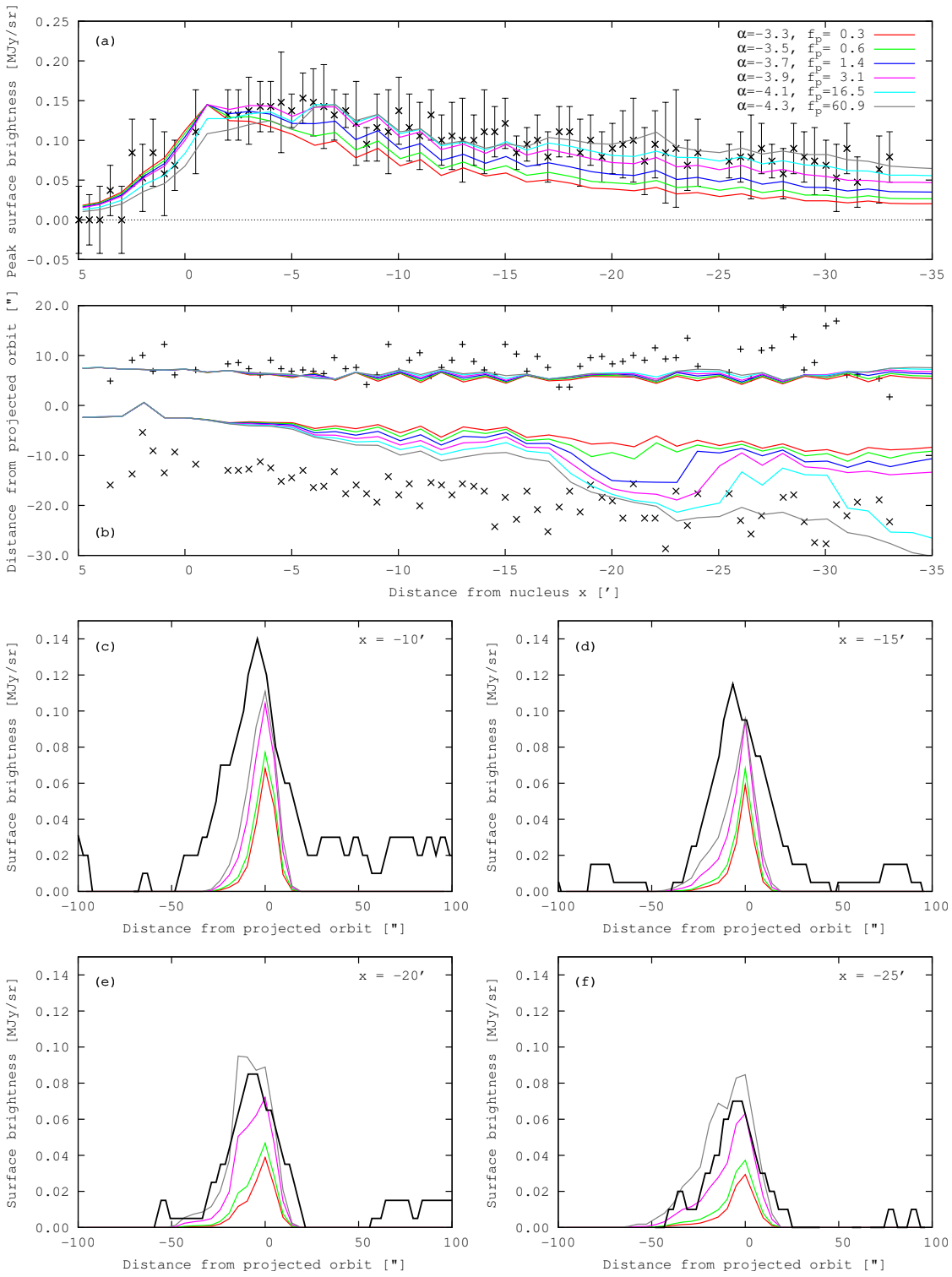

Figure 6.16: Surface brightness and FWHM of the trail in April 2006 for varying size distribution exponent. Black: Spitzer observation. Coloured: Simulated data for $f_v = 0.5$ and $f_\beta = 1$. The size distribution exponent, α, and production rate scaling factor, f_p, are listed in Panel (a). **a)** Peak surface brightness as a function of distance from the nucleus. **b)** FWHM of the trail. "+" and "x" indicate the sides dominated by the old trail and particles from the last apparition, respectively. **c) - f)** Perpendicular profiles at 10′, 15′, 20′, and 25′ behind the nucleus.

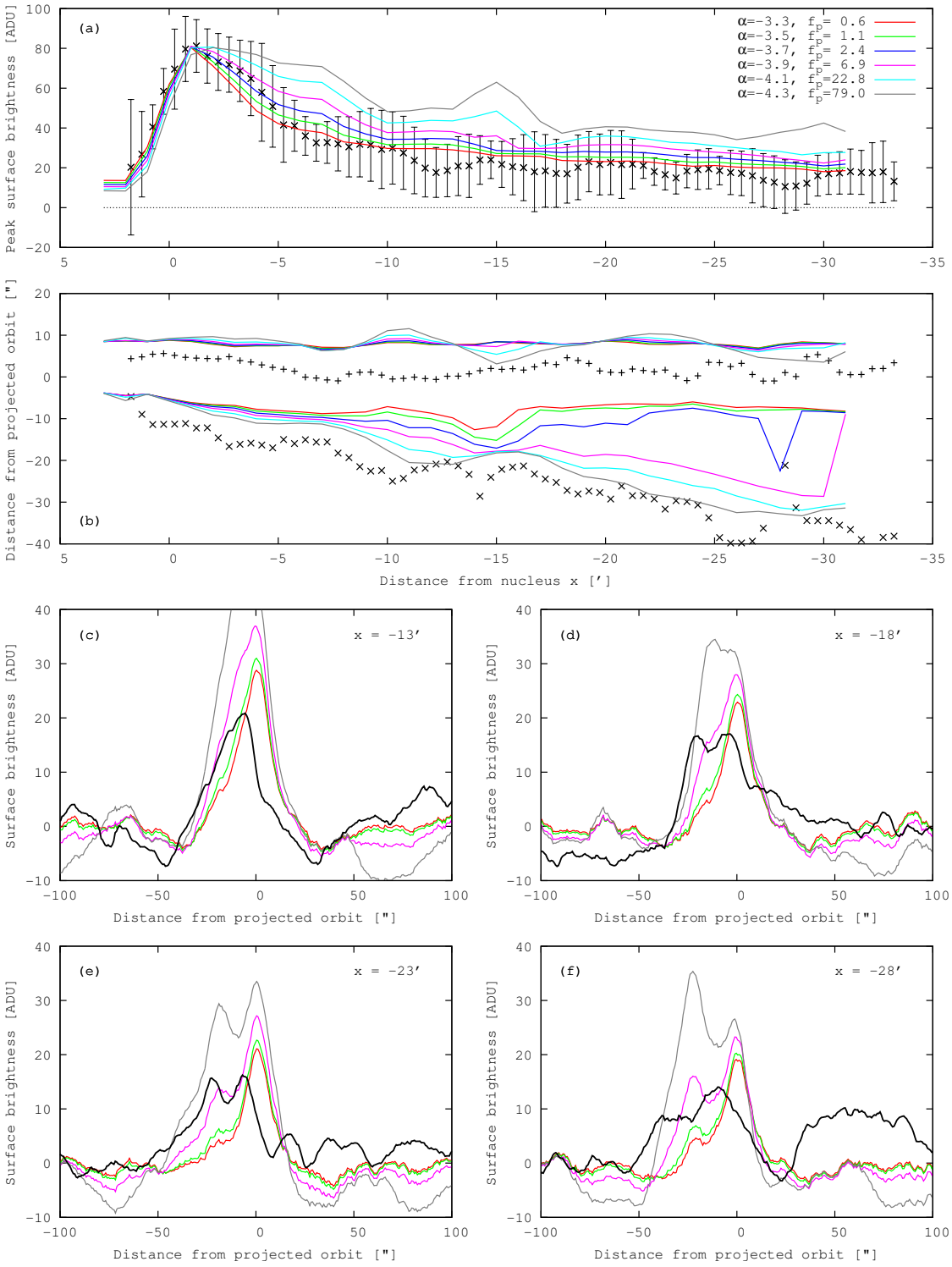

Figure 6.17: Surface brightness and FWHM of the trail in April 2004 for varying size distribution exponent. Black: WFI observation. Coloured: Simulation (with flatfield and averaging filter) for f_v = 1 and f_β = 3. The size distribution exponent, α, and production rate scaling factor, f_p, are listed in Panel (a). **a)** Peak surface brightness as a function of distance from the nucleus. **b)** FWHM of the trail. "+" and "x" indicate the sides dominated by the old trail and particles from the last apparition, respectively. **c) - f)** Perpendicular profiles at 13′, 18′, 23′, and 28′ behind the nucleus. The mismatch between observed and simulated orbit distances is attributed to inaccurate orientation of the WFI image.

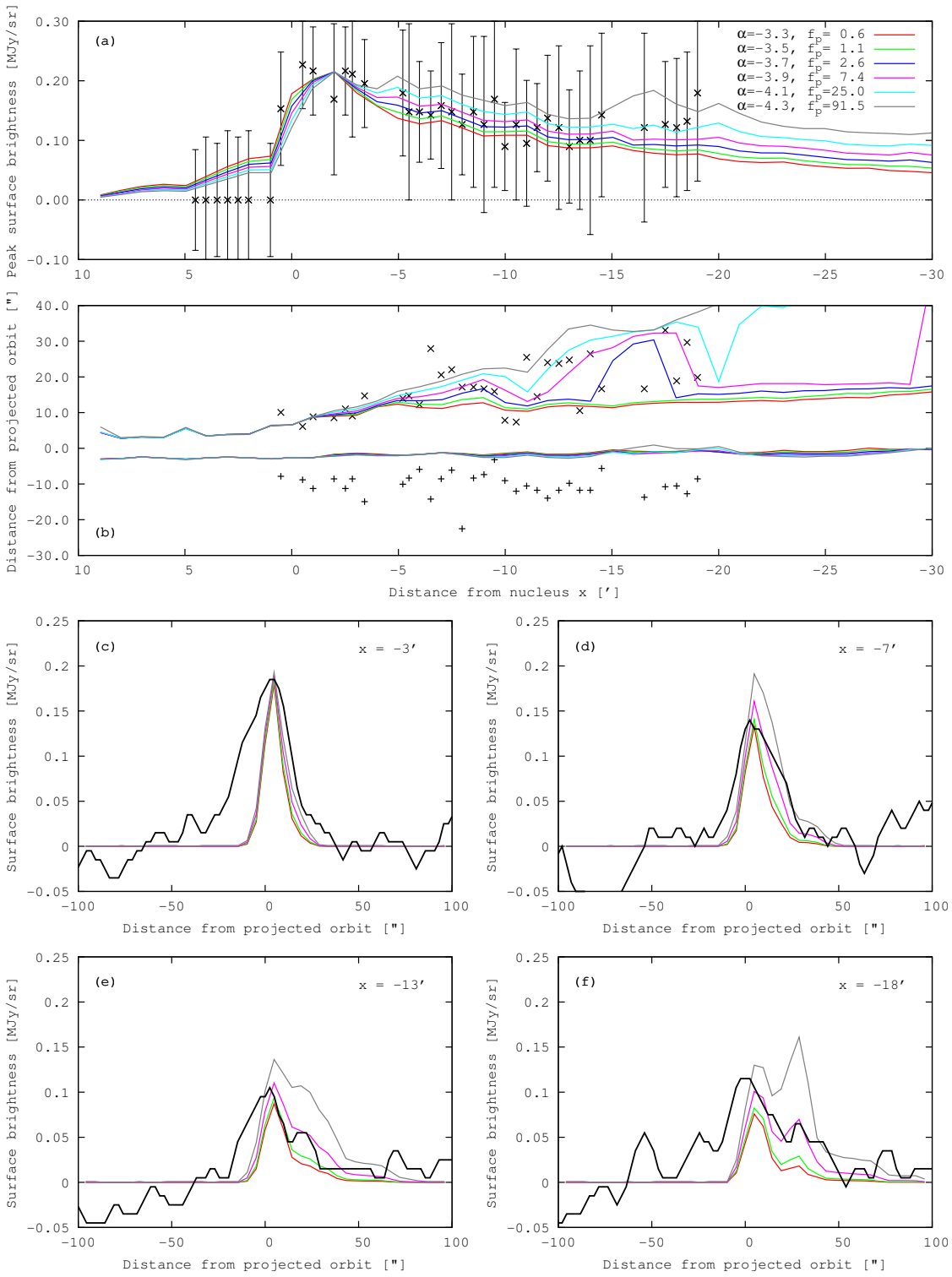

Figure 6.18: Surface brightness and FWHM of the trail in August 2005 for varying size distribution exponent. Black: Spitzer observation. Coloured: Simulated data for f_v = 1 and f_β = 3. The size distribution exponent, α, and production rate scaling factor, f_p, are listed in Panel (a). **a)** Peak surface brightness as a function of distance from the nucleus. **b)** FWHM of the trail. "+" and "x" indicate the sides dominated by the old trail and particles from the last apparition, respectively. **c) - f)** Perpendicular profiles at 3′, 7′, 13′, and 18′ behind the nucleus.

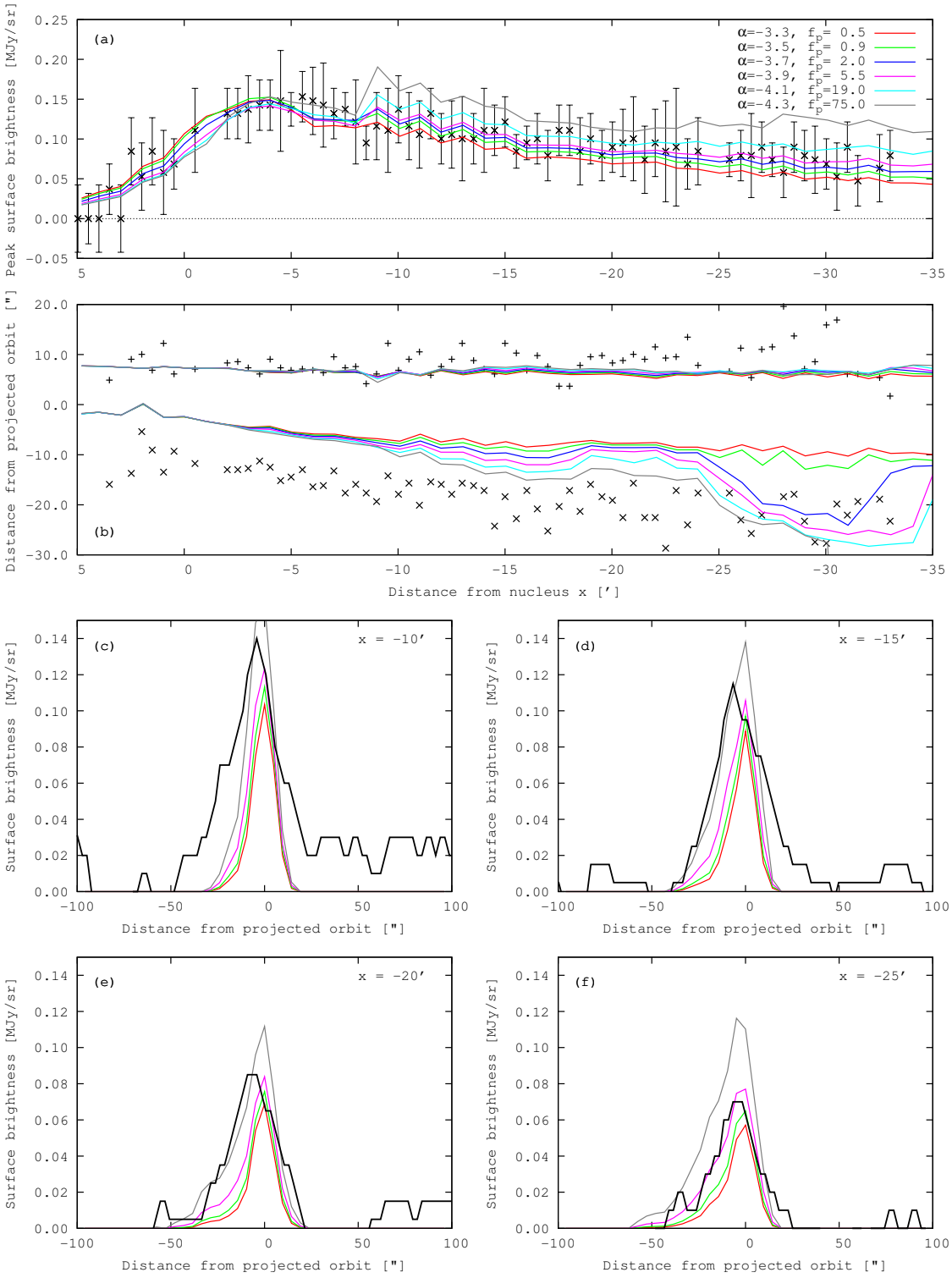

Figure 6.19: Surface brightness and FWHM of the trail in April 2006 for varying size distribution exponent. Black: Spitzer observation. Coloured: Simulated data for f_v = 1 and f_β = 3. The size distribution exponent, α, and production rate scaling factor, f_p, are listed in Panel (a). **a)** Peak surface brightness as a function of distance from the nucleus. **b)** FWHM of the trail. "+" and "x" indicate the sides dominated by the old trail and particles from the last apparition, respectively. **c) - f)** Perpendicular profiles at 10′, 15′, 20′, and 25′ behind the nucleus.

6.3 Derived Values of f_v, f_β, and α

In this section, values of f_v, f_β, and α are derived that are suitable to reproduce the observations.

The FWHM of the trail at a given nucleus distance depends on the emission speeds of the particles located at this position. Any dependence of the FWHM on the radiation pressure parameter or on the size distribution arises because these parameters affect the dominant particle size at a given position, and with the particle size also the emission speed of the observed dust. On the side of the trail dominated by old particles ("+"), the width depends primarily on the parameter f_v. It is unaffected by the choice of the size distribution exponent α within the considered interval of [-4.3,-3.3], because the surface brightness is in all cases dominated by the same species of particles (3 mm to 3 cm emitted before 2002). The trail width on the side where the neckline is observed increases for smaller values of α, because the relative contributions of smaller particles (having higher emission speeds) increase. The dependence of the trail width on the radiation pressure parameter is weak on both sides of the trail. Consequently, the parameter f_v must be chosen such that the trail width on the "+"-side is reproduced. The WFI image (Figure 6.8) is ill-suited for that purpose because of the mismatch in position angles. The width on the "+"-side is reproduced best with $1 < f_v < 1.5$ in the Spitzer 2005 image (Figure 6.9) and with $0.5 < f_v < 1$ in the Spitzer 2006 image (Figure 6.10). Because of the unexplained misalignment of the simulated old trail and the projected orbit in the 2005 image, the 2006 results are considered more reliable.

The slope of the bulge near the nucleus towards the forward direction is little influenced by the radiation pressure parameter and less so by the size distribution, whereas the position of the bulge centre is equally influenced by f_v and f_β. The observed slope of the bulge is reproduced when $f_v \leq 1$. Im summary, values of $0.5 < f_v < 1$ are considered as most appropriate to reproduce the observations. This corresponds to a dust bulk density of 100 kg/m^3 $< \rho <$ 400 kg/m^3 (Equations 5.48 and 5.50).

Increasing the radiation pressure parameter f_β shifts the centre of the bulge near the nucleus to the trailing direction (Panels (a) in Figures 6.11 to 6.13). Since variation of f_v has a similar effect for $f_v \leq 1$, f_β can only be inferred for a given value of f_v. For f_v = 0.5, f_β = 1 is appropriate (Panels (a) in Figures 6.8 to 6.10), while f_v = 1 is most suitably combined with f_β = 3 (Panels (a) in Figures 6.11 to 6.13). By Equations 2.7 and 5.46 this corresponds to $0.34 < Q_{\rm pr} < 0.45$, where the lower and upper boundaries are given by (f_β = 3, ρ = 100 kg/m^3) and (f_β = 1, ρ = 400 kg/m^3), respectively.

It is not possible to derive a single value for the size distribution exponent α suitable to reproduce all three observations in every aspect. The profile along the projected orbit in the WFI image (Panels (a) in Figures 6.14 and 6.17) is best reproduced by $-3.9 < \alpha < -3.3$. The large error bars in the Spitzer 2005 data (Panels (a) in Figures 6.15 and 6.18) encompass the entire considered range of $-4.3 < \alpha < -3.3$. The 2006 profile is compatible with $-4.1 < \alpha < -3.3$ (Figures 6.16 and 6.19).

Different ranges of α are derived from the relative brightness of neckline and trail, seen directly in the perpendicular profiles (Panels (c) to (f)) and indirectly in the FWHMs (Panels (b)). The observed equal brightness of trail and neckline in 2004 is reproduced when $-4.3 < \alpha < -3.9$ (Figures 6.14 and 6.17). A quantitative evaluation of the perpendic-

ular profiles in the 2005 observation (Figures 6.15 and 6.18) is difficult, $-4.1 < \alpha < -3.7$ seems most appropriate. The same range is found from the 2006 data (Figures 6.16 and 6.19). However, for all employed values of α, the simulated peak at less than $20'$ behind the nucleus in 2006 (Panels (c) and (d) in Figures 6.16 and 6.19) is on the projected orbit, while it is shifted towards the neckline direction in the observation. This effect is also seen from Panels (b) in Figures 6.16 and 6.19, showing that the FWHM of all simulated trail images is significantly smaller than the observed one. This indicates that more small particles are present in the field of view than given by any of the considered size distributions. A steeper size distribution ($\alpha < -4.3$) could not be reconciled with the parallel profile in the optical observation (Figures 6.14 and 6.17).

When the ratio of trail and neckline contributions in the perpendicular profiles is reproduced for the 2004 image, the total brightness of the trail beyond about $-5'$ from the nucleus is too high compared with the near-nucleus bulge. The relative brightness of the bulge and the old trail is fixed, because they consist of particles of the same size, emitted during different perihelion passages. To reproduce both the parallel and the perpendicular profiles, it would be necessary to decrease the amount of old particles relative to the young large particles in the bulge.

In summary, the closest reproduction of the observations is achieved with $0.5 < f_v < 1$, $1 < f_\beta < 3$, and $-4.1 < \alpha < -3.9$, where f_v and f_β are coupled.

6.4 The Geometric Albedo of the Dust

The results shown so far were obtained with an assumed geometric albedo of 4%. If this value was correct, the dust production scaling factors f_p required to reproduce the observed surface brightness should be the same for all three observations. Table 6.1 shows the scaling factors employed for those simulations that match the observations best. The scaling factors applied to the infrared images tend to be smaller than the corresponding factor used for the optical observation, which indicates that the albedo of the particles is less than 4%. However, there is also a systematic difference between the scaling factors derived from the two infrared images. The 2005 image requires higher scaling factors than the 2006 data. The geometric albedo p_i derived from any pair of observations is given by $p_i = 0.04 f_\mathrm{p}^\mathrm{vis} / f_\mathrm{p}^\mathrm{IR}$. The average albedo derived from the Spitzer 2005 observa-

Table 6.1: Dust production scaling factors derived for the simulated images best reproducing the observations. The scaling factors were determined such that the peak brightness near the nucleus is matched, implying an excess in simulated surface brightness at larger distance from the nucleus in the optical (2004) image.

f_v	f_β	α	f_p (VIS, 2004)	f_p (IR, 2005)	f_p (IR, 2006)
0.5	1.0	-3.9	3.3	4.0	3.1
0.5	1.0	-4.1	10.5	21.1	16.5
1.0	3.0	-3.9	6.9	7.4	5.5
1.0	3.0	-4.1	22.8	25.0	19.0

tion is p^{05} = 0.032 $\pm$ 0.004, while the Spitzer 2006 data yield p^{06} = 0.042 $\pm$ 0.006. The derived value is an average for the ensemble of particles and the entire wavelength band. Dependence of the albedo on wavelength cannot be inferred from this observation.

6.5 Dust Production Rates and $Af\rho$

The dust production rates required to reproduce the observed surface brightness are derived from the auxiliary production rates $Q_{j,\mathrm{aux}}$ (Section 5.4.10) and the scaling factors f_p applied to the Spitzer images (Table 6.1). This relation is independent of the particle albedo. Figure 6.20a and b show the mass production rates of particles with $s > 60\,\mu$m needed to reproduce the observations for the parameters $-4.1 < \alpha < -3.9$ and $0.5 < f_v < 1$. At perihelion the production rates are on the order of 300 to 1000 kg/s, where the lowest production rate corresponds to the parameter set $\alpha = -3.9$ and $f_v = 0.5$.

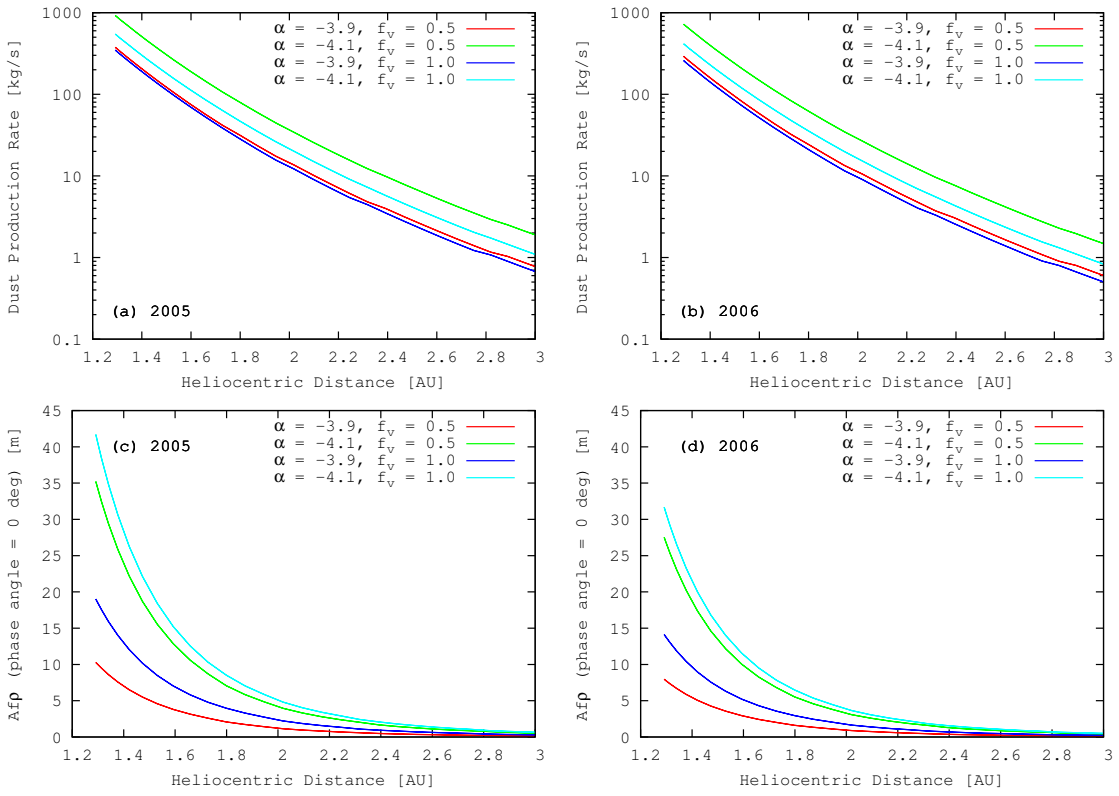

Figure 6.20: Mass production rates and $Af\rho$ of particles having $s > 60\,\mu$m as functions of heliocentric distance for the parameter sets most suitable to reproduce the observations, $-4.1 < \alpha < -3.9$ and $0.5 < f_v < 1$. The bulk density was assumed to be 100 kg/m^3 if f_v = 1, and 400 kg/m^3 if f_v = 0.5. **a)** Dust mass production rates required to reproduce the Spitzer 2005 image. **b)** Dust mass production rates required to reproduce the Spitzer 2006 image. **c)** $Af\rho$ in visible light corresponding to the production rates shown in Panel (a) and a geometric albedo of 4%. **d)** $Af\rho$ in visible light corresponding to the production rates shown in Panel (b) and a geometric albedo of 4%.

The dust production rates derived from the 2005 image are on average higher by a factor of 1.3 than those derived from the 2006 image (Table 6.1). In other words, the simulated images for a given production rate would display a similar surface brightness. The model does not reproduce the observed decrease in surface brightness from 2005 to 2006.

Figures 6.20c and d show the $Af\rho$-values in visible light due to particles with $s > 60\,\mu$m and for a phase angle of 0° that correspond to the derived production rates. These values are considerably higher than the measured data displayed in Figure 3.2, although they do not include the light scattered by particles smaller than $60\,\mu$m.

Chapter 7

Conclusion

7.1 Summary

The primary goal of this work was to constrain the size distribution and production rates of mm-sized and larger dust particles emitted by comet 67P/Churyumov-Gerasimenko. For this purpose, three images of the 67P/C–G dust trail – one in visible light and two at mid-infrared wavelengths – were obtained at heliocentric distances between 4.7 AU and 5.7 AU (Chapter 4). A method to generate simulated images of a cometary trail was presented in Chapter 5. From the comparison of observed and simulated images, suitable model parameters were derived in Chapter 6.

Assuming that cometary activity ceased at 3 AU, the dust present in the images is characterised by radiation pressure parameters $\beta < 0.01$, corresponding to sizes $s > 60\,\mu$m and masses $m > 4 \times 10^{-10}$ kg. The particles expected in the FOVs of the images were larger than the wavelengths at which the observations were made. The geometric optics approximation for the scattering of visible light was therefore adopted, and the thermal emission of the particles was modelled by that of a blackbody at the equilibrium temperature given by the heliocentric distance during the observation.

The free parameters of the simulation were the exponent α of the dust size distribution, the relation between emission speeds and particle sizes, which is governed by the bulk density ρ, the radiation pressure efficiency Q_{pr}, the average geometric albedo of the dust at visible wavelengths, and the magnitude of the dust production rate for a given heliocentric distance.

The closest reproduction of the observations was achieved with a size distribution exponent of $-4.1 < \alpha < -3.9$, which is well within the range of values given in the literature obtained by a variety of methods and for several comets (Table 2.1). The radiation pressure efficiency $0.34 < Q_{\mathrm{pr}} < 0.45$ roughly matches the value given by Gustafson et al. (2001) for astronomical silicates. The derived bulk density of 100 kg/m^3 $< \rho <$ 400 kg/m^3 is also in agreement with earlier findings. This confirms the common view that the dust particles are porous aggregates. For comparison, the bulk density of the solid material is on the order of 3000 kg/m^3 for silicates. The generally adopted dust geometric albedo of 4% is confirmed by the 2006 observation, while the 2005 observation yields a slightly smaller value of (3.2 ± 0.4)%. The production rates of particles larger than 60 μm are on the order of 200 to 1000 kg/s at perihelion and of 0.5 to 2 kg/s at 3 AU.

7.2 Open Questions and Future Work

Translating the production rates, emission speeds, and size distribution required to reproduce the observed trail brightness to $Af\rho$, the values obtained for large particles alone are on the same order of magnitude or exceed those measured for all dust in the coma (Figures 3.2 and 6.20). This implies that the coma brightness in the inner solar system would be dominated by particles of 60 μm and larger, which is contrary to the evidence from multiple sources, including mid-infrared spectra and in situ data. It could be argued that this evidence was obtained for a variety of comets and that 67P/C–G might be an exceptional one. But also for the coma of 67P/C–G Divine et al. (1986) have derived a peak grain radius on the order of 0.6 μm between 1.3 and 1.9 AU from thermal infrared spectra. The model presented in this thesis is therefore not suitable to reconcile the observed surface brightness in the trail with the coma brightness measured within 3 AU.

Three further aspects of the observations cannot be reproduced with the adopted model. In the simulated image for 2004, the surface brightness of the old trail (large particles emitted before 2002) is too high relative to the surface brightness in the bulge close to the nucleus attributed to particles of the same size emitted during the 2002/03 apparition. The effect may be present in the 2005 and 2006 images as well, but the lower resolution of these images precludes a definite evaluation of this aspect.

Not reproducible, either, is the observed width of the trail south of the projected orbit at less than 20′ behind the nucleus in the 2006 image (Figure 4.9). Since the excess brightness is found comparatively far from the projected orbit, it must be attributed to particles subject to significant radiation pressure.

The third aspect not reflected by the simulations is the observed decrease of the trail surface brightness by a factor of 1.3 from 2005 to 2006, which is significant despite the low SNR of the 2005 image.

The excess of old, large particles in the simulation could be avoided by assuming that the activity of 67P/C–G during the 2002/03 apparition was stronger than during the previous passages through the inner solar system. This, however, is not supported by the measured $Af\rho$ values (Figure 3.2) which are on the same order of magnitude for the last three apparitions. Dissipation of the trail particles due to planetary perturbations is not expected to be relevant for the timescales in question, either (J. Vaubaillon, private communication).

Fulle et al. (2004) and Moreno et al. (2004) have derived the size distribution and production rates of dust emitted by 67P/C–G from images taken between perihelion in 2002 and 2.7 AU. They propose a constant production rate of 200 kg/s and a size distribution exponent of $\alpha = -3.5$ between 3.6 AU and 1.7 AU before the perihelion passage, dropping to 10 kg/s and $\alpha = -4.5$ after perihelion. The suggested high production rates before perihelion are not in direct conflict with observations, because no data are available for the time in question (Figure 3.2). The simulation tool described in Chapter 5 has not been run with the parameters suggested by Fulle et al. (2004) and Moreno et al. (2004). The high production rate over a long time interval may be sufficient to reproduce the observed surface brightness without getting in conflict with the measured $Af\rho$ around and after perihelion. Assuming further that the high production rate was specific to the 2002/03 apparition, also the imbalance between young and old large particles in the 2004

observation may be accounted for. The observed brightness south of the projected orbit in 2006, probably due to small particles, cannot be explained by a high production rate long before perihelion. The same is most likely true for the decrease in surface brightness from 2005 to 2006.

Green et al. (2004) infer from in situ measurements of the dust number density and mass distribution in the coma of comet 81P/Wild 2 a high variability on small spatial scales of both these quantities, which they ascribe to localised emission from the surface (jets) and particle fractionation after release from the nucleus. The breaking up of large particles on timescales of at least several years after their emission from the nucleus could account for the four major unresolved issues discussed above. If the trail particles had been disintegrating during the time interval covered by the observations, there would have been be a population of small particles in the FOVs that may have contributed significantly to the measured surface brightness. There would be no need to assume unrealistically high production rates of large particles to reproduce the observations. The declining brightness contribution by old, large particles would follow from their disintegration, as would the decreasing surface brightness from 2005 to 2006. The small, high-β particles observed in 2006 would be the fragments of broken-up trail particles.

A quantitative evaluation of particle fractionation in the trail requires a much more elaborate model than the one presented in this work. The size distribution in such a model would have to be time dependent; the emission speed would not be a unique function of particle size; and – due to the presence of small particles –, the simple assumptions made for the scattering and thermal emission by dust would no longer be appropriate. Quantitative information on the occurrence of particle fragmentation in the coma of 67P/C–G will be obtained by help of the instruments on board the Rosetta spacecraft. Fragmentation products would for example be seen by the GIADA instrument as a population of small particles with comparatively low speeds.

Appendix A

Stars Used for WFI Calibration

Table A.1: Stars used for the calibration of the WFI image. The first column gives their ID in the USNO-B1.0 catalogue. The B1 and R1 magnitudes were derived from the POSS1 set of plates, while the B2, R2, and I2 magnitudes were measured on POSS2 plates. The standard deviation of the magnitudes given in the catalogue is 0.25 mag (Monet et al., 2003). The last column refers to the night during which the concerned star was used for calibration.

ID	R.A. (J2000)	DEC (J2000)	Epoch	B1	R1	B2	R2	I2	Night
07860263175	14:21:41.88	−11:18:52.95	1973.7	20.34	19.07	19.87	19.15	18.61	1
07860263334	14:22:28.077	−11:19:10.73	1973.7	20.11	18.59	20.31	19.27	18.88	1
07870261539	14:21:12.517	−11:14:17.81	1978.3	20.59	–	19.9	19.17	18.55	1
07870261859	14:22:59.546	−11:15:42.33	1973.7	19.94	19.19	19.95	19.26	18.38	1
07880263163	14:21:48.816	−11:10:33.00	1973.7	20.69	19.02	20.29	18.97	18.71	1
07880263342	14:22:45.831	−11:07:05.24	1973.7	20.13	18.98	19.73	19.05	18.27	1
07880263372	14:22:56.551	−11:11:33.41	1973.7	20	18.99	20.24	19.19	18.57	1
07880263379	14:22:58.203	−11:06:45.86	1973.7	19.87	19.09	20.04	18.89	18.67	1
07890260860	14:20:49.277	−11:04:28.88	1973.7	20.38	19.3	20.29	19.07	18.85	1
07890261125	14:22:06.00	−11:02:36.04	1973.7	20.05	19.43	19.62	18.36	18.12	1
07890261195	14:22:29.807	−11:00:13.31	1978.3	20.33	–	20.34	19.23	18.83	1
07900263354	14:21:18.393	−10:58:57.32	1973.7	19.96	18.78	19.36	18.67	18.32	1
07900263603	14:22:36.451	−10:54:14.29	1973.7	20.29	19.42	20.27	19.41	18.75	1
07910260234	14:21:02.91	−10:52:01.01	1978.3	20.3	–	20.23	19.3	18.83	1
07910260359	14:21:40.062	−10:50:13.97	1973.7	20.2	18.96	20.19	19.13	18.55	1
07910260440	14:22:02.959	−10:49:39.36	1973.7	20.46	19.58	20.43	19.42	18.93	1
07910260575	14:22:46.981	−10:50:11.38	1973.7	20.22	19.21	20.23	18.85	18.63	1
07910260625	14:22:57.041	−10:53:02.30	1973.7	20.08	18.77	19.29	18.12	18.12	1
07910260627	14:22:57.963	−10:50:46.60	1973.7	20.16	19.37	20.07	19.31	18.77	1
07920261533	14:20:42.305	−10:47:25.67	1973.5	20.05	18.74	19.89	18.61	18.66	1
07920261755	14:21:46.57	−10:47:43.87	1973.7	19.73	18.62	19.5	18.46	18.31	1
07950257080	14:09:04.947	−10:25:42.04	1984.7	–	18.71	20.01	19.2	18.66	3
07950257100	14:09:15.054	−10:27:07.70	1978.6	19.55	18.66	19.54	18.87	18.17	2
07950257134	14:09:23.666	−10:28:19.30	1978.6	20.64	18.69	19.92	19.03	18.65	2
07950257159	14:09:30.739	−10:27:06.60	1978.6	20.25	18.97	20.3	19.04	18.44	2
07950257181	14:09:38.389	−10:27:06.38	1978.6	19.64	18.69	19.81	18.79	18.63	2
07950257194	14:09:41.991	−10:27:15.70	1978.6	20.56	19.43	20.37	19.03	18.6	2
07950257348	14:10:17.328	−10:25:29.51	1976.3	20.14	18.85	19.81	18.47	17.99	2,3
07950257603	14:11:05.26	−10:24:08.90	1976.3	19.38	18.28	19.19	18.46	17.86	2
07960254867	14:09:26.739	−10:22:04.87	1978.6	20.48	19.32	20.78	19.47	18.94	2,3,4

Continued on next page

Table A.1 – continued from previous page

ID	R.A. (J2000)	DEC (J2000)	Epoch	B1	R1	B2	R2	I2	Night
07960254985	14:09:59.599	−10:20:41.30	1976.3	19.9	18.37	19.7	18.44	18.46	3
07960254991	14:10:00.805	−10:21:44.44	1973.3	19.14	18.42	19.51	18.34	18.05	3
07960255007	14:10:04.539	−10:21:22.31	1974.9	18.67	18.39	18.83	18	17.81	3
07960255028	14:10:10.458	−10:18:47.86	1974.9	19.68	18.81	19.72	18.7	18.56	2,3
07960255097	14:10:27.003	−10:21:41.43	1976.3	20.27	18.89	20.07	18.94	18.89	2,3
07960255127	14:10:33.187	−10:23:34.80	1976.3	19.95	18.86	19.62	18.35	17.8	2,3
07960255164	14:10:43.588	−10:18:23.39	1977.2	20.32	19.23	20.38	19.1	19.09	2
07960255233	14:11:00.639	−10:21:33.51	1974.9	20.05	19.07	20.03	18.67	18.57	2
07960255277	14:11:10.956	−10:23:39.56	1978.6	19.45	18.81	19.86	19.12	18.48	2
07970255032	14:08:18.937	−10:17:51.57	1978.6	19.62	19.09	19.81	18.75	18.52	3,4
07970255045	14:08:24.154	−10:13:23.70	1984.7	19.99	–	20.41	19.51	18.95	3,4
07970255071	14:08:30.283	−10:17:04.21	1978.6	20.58	19.45	20.68	19.42	18.86	3,4
07970255111	14:08:49.509	−10:13:51.78	1978.6	19.61	18.27	19.16	18.26	17.88	4
07970255137	14:08:59.455	−10:13:51.88	1978.6	20.25	18.97	20.16	19.22	18.76	3,4
07970255242	14:09:30.39	−10:14:26.19	1978.6	19.89	19.07	19.92	18.82	18.19	2,3,4
07970255269	14:09:37.639	−10:17:56.95	1978.6	20	19.33	20.42	19.64	18.8	2,3,4
07970255313	14:09:46.705	−10:14:44.00	1976.3	19.61	18.4	19.41	18.38	17.9	4
07970255387	14:10:01.812	−10:14:48.38	1974.9	19.31	18.89	19.74	18.66	18.35	2,3
07970255405	14:10:06.182	−10:14:34.64	1974.9	19.51	17.75	18.98	17.78	17.67	3
07970255428	14:10:09.366	−10:14:48.26	1974.9	19.51	18.18	19.03	17.83	17.48	2
07970255462	14:10:14.756	−10:17:07.19	1974.9	19.93	18.67	19.99	18.64	18.28	2,3
07970255488	14:10:19.807	−10:13:17.66	1974.9	20.32	19.14	20.37	19.2	18.67	2,3
07970255512	14:10:24.056	−10:16:33.59	1975.6	20.4	19.56	20.52	19.6	19.07	2,3
07970255534	14:10:26.946	−10:14:45.85	1977.2	19.97	18.64	20.29	18.85	18.84	2,3
07970255558	14:10:31.584	−10:16:00.77	1974.9	19.66	18.49	19.47	18.39	17.75	3
07970255574	14:10:33.331	−10:12:26.50	1978.6	19.63	18.25	19.43	18.48	17.95	2,3
07970255753	14:11:14.778	−10:14:58.79	1974.9	19.59	18.21	19.4	18.58	18.39	2
07980254469	14:08:23.886	−10:09:22.36	1978.6	19.55	18.53	19.35	18.34	18.04	3
07980254615	14:09:13.955	−10:07:13.90	1978.6	19.8	18.63	19.66	18.55	18.3	2,3
07980254642	14:09:19.743	−10:09:16.57	1978.6	19.97	18.74	19.57	18.11	18.08	3,4
07980254741	14:09:50.857	−10:08:08.23	1978.6	20.08	18.61	20.17	19.34	19.03	2,3,4
07980254744	14:09:51.376	−10:06:21.86	1976.3	19.84	18.62	19.47	18.78	18.45	2,4
07980254782	14:09:59.318	−10:10:21.72	1976.3	19.5	18.4	19.32	18.16	17.64	3
07980254814	14:10:07.026	−10:11:36.07	1976.3	18.8	17.97	18.38	17.72	17.33	3
07980254934	14:10:30.474	−10:06:34.38	1974.9	20.11	19.5	20.17	19.15	18.59	2,3
07980254943	14:10:31.362	−10:10:02.98	1976.3	19.93	19.36	19.75	18.93	18.66	3
07980254972	14:10:36.729	−10:11:57.58	1978.6	19.78	18.81	20.11	19.2	18.58	2,3
07990256110	14:09:10.088	−10:01:55.54	1978.6	19.4	18.24	19.43	18.14	18.21	3
07990256191	14:09:37.529	−10:01:10.45	1978.6	20.28	18.62	19.59	18.61	18.31	2,3
07990256522	14:11:06.524	−10:03:29.78	1974.9	20	18.85	20.02	18.84	18.47	2
07990256525	14:11:06.853	−10:01:54.40	1974.9	19.76	18.72	19.66	18.31	18.32	2
07990256528	14:11:07.625	−10:04:50.99	1974.9	19.61	18.38	19.65	18.54	18.32	2
08000257137	14:07:45.973	−09:59:02.65	1978.6	19.96	18.64	20.5	19.34	19.07	4
08000257229	14:08:21.319	−09:56:31.61	1978.6	19.26	17.98	19.04	17.85	18.07	4
08000257234	14:08:23.283	−09:58:20.33	1978.6	19.78	18.66	19.86	18.87	18.73	3,4
08000257245	14:08:25.697	−09:55:05.75	1978.6	19.48	18.48	19.41	18.29	18.23	4
08000257535	14:09:52.32	−09:57:28.56	1978.6	20.1	19.02	20.12	19.21	18.8	2,3,4
08000257555	14:09:58.53	−09:56:38.15	1978.6	20.12	19.08	20.18	19.3	18.61	2,3
08000257880	14:10:57.309	−09:57:41.77	1977.2	20.33	19.08	20.52	19.23	18.59	2

Appendix B

Impact of Flatfield on WFI Data

In Section 4.1.6 it was argued that the superflats used to remove the instrumental signature from the WFI raw data contain information from the dust trail, leading to a decreased signal in the final data. The `boxcar` spatial averaging filter also influences the observed brightness distribution. For the analyses in Chapter 6, the simulated trail images were therefore subjected to an analogous process of simulated flatfielding. In the following, the procedure to simulate the flatfielding process is described and the introduced error is discussed.

The simulated image is rotated by 26.5° and magnified to the same scale of 0.71″/pix as the original image, conserving the total flux. Then 50 images are created containing Gaussian noise with the variance σ_0 = 241.5 ADU, derived in Section 4.1.5 for the individual exposures, and a mean of 40 000 ADU, which represents the mean sky level in the raw images. The flux in the simulated trail image is converted to ADU by the factor $c = 2.21 \times 10^{-21}$ W/m^2/ADU (Equation 4.7) and added to the simulated background with offsets reflecting the nucleus coordinates in the original data. Superflats are simulated by generating median-averaged images from five exposures each. The superflats are normalised by division through the mean sky level. The original images are divided by the corresponding superflat and average-combined in the co-moving frame of the comet. The resulting image is `boxcar` filtered averaging over 200×10 pixels^2. The peak brightness parallel to the projected orbit and the FWHM as a function of distance from the nucleus are then evaluated in analogy to the observed image, estimating a lower and upper limit for the sky background from perpendicular profiles.

The attenuation of the trail signal due to flatfielding generally depends on the brightness and shape of the original image. The error increases with lower surface brightness in the original data. A quantitative estimate of the error can therefore only be given for a specific input image. This is done in the following for the simulated image obtained with $\alpha = -3.9$, $f_\beta = 3$, and $f_v = 1$, which was found in Chapter 6 to match the observation reasonably well.

To separate the action of the superflat from that of the `boxcar` filter, the original image is also boxcar-filtered without simulating the superflat. The derived profiles and FWHM are shown in Figure B.1. The `boxcar` filter flattens the profiles but does not significantly alter the flux. In contrast, the flatfielding results in a decrease in surface brightness by 20 to 40%, which is in good agreement with the expectations (Section 4.1.6).

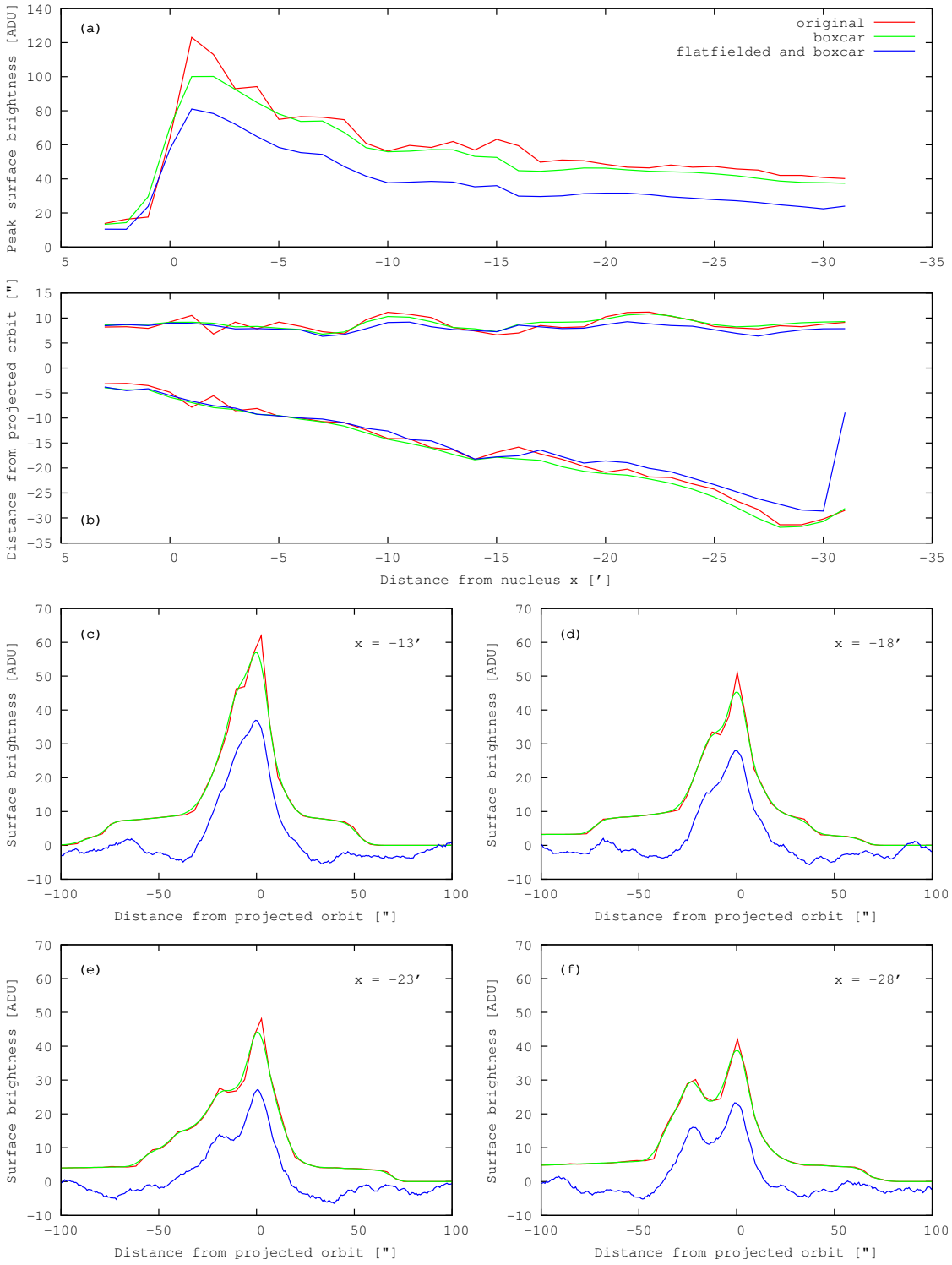

Figure B.1: Profiles and width of simulated trail image for $\alpha = -3.9$, $f_\beta = 3$, and $f_v = 1$, before and after simulated flatfielding and `boxcar` filtering. Red: original image, green: only `boxcar` filtered, blue: flatfielded and `boxcar` filtered. **a)** Peak brightness along the trail axis. **b)** FWHM as function of distance from the nucleus. **c) - f)** Profiles perpendicular to the orbit.

Appendix C

Hydrodynamic Coma Model

The emission speeds of dust particles were obtained as the terminal speeds in the hydrodynamic coma model described in detail in Müller and Grün (1997, 1998); Müller (1999); Landgraf et al. (1999). The comet nucleus is assumed to be spherical, and – for the present purpose – the activity distribution on its surface was considered isotropic. In the cited publications, more realistic activity distributions have also been implemented. The flows of gas and dust around the comet are calculated, yielding at any position in the coma the density, velocity, and temperature of the gas, and the number density and velocity of dust particles of different mass classes. Each class represents particles having masses within one decade in the range of 10^{-20} to 10 kg. All dust particles of one class are assigned the same representative mass and radius. It is assumed that the particles have spherical shapes and a constant bulk density.

The numerical method used to compute the dynamics of gas and dust takes advantage of the fact that the influence of the dust on the gas flow is of minor importance. In a first step, the gas flow is calculated without taking into account the presence of dust. It is assumed that the gas is in thermal equilibrium everywhere, and that the mean molecular mass is constant across the coma and given by the mean of the masses of the two most common molecules, H_2O and CO, weighted by their overall abundances in the coma. The production rates of these species are input parameters to the model. The CO activity is treated as independent of heliocentric distance using the value of 10^{26} molecules/s. The water activity is assumed to depend on heliocentric distance as indicated by spectroscopic measurements (Figure 3.1).

In a second step, dust trajectories are integrated considering the gravitation of the nucleus and the drag force exerted by the gas. The emission speeds used in this thesis were obtained from fitting the analytical expression given by Equation 5.48 to the terminal speeds of particles at a distance of 20 km from the nucleus centre, where the gas flow is sufficiently to preclude a significant momentum transfer to the dust particles.

Appendix D

List of Acronyms

26P/G–S	26P/Grigg-Skjellerup
67P/C–G	67P/Churyumov-Gerasimenko
ADU	Analogue Digital Units
AOR	Astronomical Observation Request
APEX	Spitzer Astronomical Point Source EXtraction
AU	Astronomical Unit
BCD	Basic Calibrated Data
CBS	Cometocentric Bipolar System
CCD	Charge Coupled Device
COBE	Cosmic Background Explorer
DCE	Data Collection Event
DFMI	Dust Flux Monitor Instrument
DIDSY	Dust Impact Detection System
ESO	European Southern Observatory
FORS	FOcal Reducer and low dispersion Spectrograph
FOV	Field of View
FWHM	Full Width Half Maximum
GIADA	Grain Impact Analyser and Dust Accumulator
GRE	Giotto Radio Science Experiment
IRAF	Image Reduction and Data Analysis Facility
IRAS	Infrared Astronomical Satellite
JPL	Jet Propulsion Laboratory
MIPS	Multiband Imaging Photometer
MOPEX	Mosaicking and Point Source EXtraction
MPG	Max Planck Society
POSS	Palomar Observatory Sky Survey
PSF	Point Spread Function
SNR	Signal-to-Noise Ratio
SPOT	Spitzer Planning Observations Tool
SSC	Spitzer Science Centre
TNG	Telescopio Nazionale Galileo
USNOFS	United States Naval Observatory Flagstaff Station
VeGa	Venera Galley
VLT	Very Large Telescope
WFI	Wide Field Imager

Appendix E

Physical and Astronomical Constants

Physical Constants:[1]

Planck's constant	h	=	$(6.626\,068\,96 \pm 0.000\,000\,33) \times 10^{-34}$ J s
Boltzmann's constant	k_B	=	$(1.380\,650\,4 \pm 0.000\,002\,4) \times 10^{23}$ J K^{-1}
Wien's displacement constant (λ)	b	=	$(2.897\,768\,5 \pm 0.000\,005\,1 \times 10^{-3}$ m K)
Stefan-Boltzmann constant	σ	=	$(5.670\,400 \pm 0.000\,040) \times 10^{-8}$ W m^{-2} K^{-4}
Gravitational constant	G	=	$(6.674\,2 \pm 0.001\,0) \times 10^{-11}$ m^3 kg^{-1} s^{-2}
Speed of light in vacuum[2]	c	=	299 792 458 m s^{-1}

Astronomical Quantities:

Astronomical Unit[3]	AU	=	$1.495\,978\,706{,}6 \times 10^{11}$ m
Luminosity of the Sun[3]	$L_\odot$	=	$(3.845 \pm 0.008) \times 10^{26}$ W
Mass of the Sun[3]	$M_\odot$	=	1.9891×10^{30} kg
Solar flux at 1 AU[3]	$I_\odot$	=	1365 . . . 1369 W m^{-2}
Solar R-magnitude[4]			-27.14 mag

[1] 2006 CODATA recommended values, maintained at the Physics Laboratory of the National Institute of Standards and Technology (`http://physics.nist.gov/cuu/Constants/`).

[2] The value of c is exact because of the definition of the metre.

[3] Values taken from Cox (2000).

[4] Values given in the literature vary between -26.9 and -27.3, depending on the employed filter (e. g. Szabó et al., 2002).

Bibliography

J. Agarwal, M. Müller, and E. Grün. Dust Environment Modelling of Comet 67P/Churyumov-Gerasimenko. *Space Science Reviews*, pages 82–134, February 2007.

M. F. A'Hearn, M. J. S. Belton, W. A. Delamere, J. Kissel, K. P. Klaasen, L. A. McFadden, K. J. Meech, H. J. Melosh, P. H. Schultz, J. M. Sunshine, P. C. Thomas, J. Veverka, D. K. Yeomans, M. W. Baca, I. Busko, C. J. Crockett, S. M. Collins, M. Desnoyer, C. A. Eberhardy, C. M. Ernst, T. L. Farnham, L. Feaga, O. Groussin, D. Hampton, S. I. Ipatov, J.-Y. Li, D. Lindler, C. M. Lisse, N. Mastrodemos, W. M. Owen, J. E. Richardson, D. D. Wellnitz, and R. L. White. Deep Impact: Excavating Comet Tempel 1. *Science*, 310:258–264, October 2005.

M. F. A'Hearn, R. L. Millis, D. G. Schleicher, D. J. Osip, and P. V. Birch. The ensemble properties of comets: Results from narrowband photometry of 85 comets, 1976-1992. *Icarus*, 118:223–270, December 1995.

M. F. A'Hearn, D. G. Schleicher, R. L. Millis, P. D. Feldman, and D. T. Thompson. Comet Bowell 1980b. *AJ*, 89:579–591, April 1984.

C. W. Allen. *Astrophysical quantities*. London: University of London, Athlone Press, —c1973, 3rd ed., 1973.

D. Bockelée-Morvan, R. Moreno, N. Biver, J. Crovisier, J.-F. Crifo, M. Fulle, and M. Grewing. CO and dust productions in 67P/Churyumov-Gerasimenko at 3 AU post-perihelion. In L. Colangeli, E. Mazzotta Epifani, and P. Palumbo, editors, *ASSL Vol. 311: The New Rosetta Targets. Observations, Simulations and Instrument Performances*, pages 25–36, October 2004.

C. F. Bohren and D. R. Huffman. *Absorption and scattering of light by small particles*. New York: Wiley, 1983, 1983.

D. Brownlee, P. Tsou, J. Aléon, C. M. O. '. Alexander, T. Araki, S. Bajt, G. A. Baratta, R. Bastien, P. Bland, P. Bleuet, J. Borg, J. P. Bradley, A. Brearley, F. Brenker, S. Brennan, J. C. Bridges, N. D. Browning, J. R. Brucato, E. Bullock, M. J. Burchell, H. Busemann, A. Butterworth, M. Chaussidon, A. Cheuvront, M. Chi, M. J. Cintala, B. C. Clark, S. J. Clemett, G. Cody, L. Colangeli, G. Cooper, P. Cordier, C. Daghlian, Z. Dai, L. D'Hendecourt, Z. Djouadi, G. Dominguez, T. Duxbury, J. P. Dworkin, D. S. Ebel, T. E. Economou, S. Fakra, S. A. J. Fairey, S. Fallon, G. Ferrini, T. Ferroir, H. Fleckenstein, C. Floss, G. Flynn, I. A. Franchi, M. Fries, Z. Gainsforth, J.-P. Gallien, M. Genge,

M. K. Gilles, P. Gillet, J. Gilmour, D. P. Glavin, M. Gounelle, M. M. Grady, G. A. Graham, P. G. Grant, S. F. Green, F. Grossemy, L. Grossman, J. N. Grossman, Y. Guan, K. Hagiya, R. Harvey, P. Heck, G. F. Herzog, P. Hoppe, F. Hörz, J. Huth, I. D. Hutcheon, K. Ignatyev, H. Ishii, M. Ito, D. Jacob, C. Jacobsen, S. Jacobsen, S. Jones, D. Joswiak, A. Jurewicz, A. T. Kearsley, L. P. Keller, H. Khodja, A. L. D. Kilcoyne, J. Kissel, A. Krot, F. Langenhorst, A. Lanzirotti, L. Le, L. A. Leshin, J. Leitner, L. Lemelle, H. Leroux, M.-C. Liu, K. Luening, I. Lyon, G. MacPherson, M. A. Marcus, K. Marhas, B. Marty, G. Matrajt, K. McKeegan, A. Meibom, V. Mennella, K. Messenger, S. Messenger, T. Mikouchi, S. Mostefaoui, T. Nakamura, T. Nakano, M. Newville, L. R. Nittler, I. Ohnishi, K. Ohsumi, K. Okudaira, D. A. Papanastassiou, R. Palma, M. E. Palumbo, R. O. Pepin, D. Perkins, M. Perronnet, P. Pianetta, W. Rao, F. J. M. Rietmeijer, F. Robert, D. Rost, A. Rotundi, R. Ryan, S. A. Sandford, C. S. Schwandt, T. H. See, D. Schlutter, J. Sheffield-Parker, A. Simionovici, S. Simon, I. Sitnitsky, C. J. Snead, M. K. Spencer, F. J. Stadermann, A. Steele, T. Stephan, R. Stroud, J. Susini, S. R. Sutton, Y. Suzuki, M. Taheri, S. Taylor, N. Teslich, K. Tomeoka, N. Tomioka, A. Toppani, J. M. Trigo-Rodríguez, D. Troadec, A. Tsuchiyama, A. J. Tuzzolino, T. Tyliszczak, K. Uesugi, M. Velbel, J. Vellenga, E. Vicenzi, L. Vincze, J. Warren, I. Weber, M. Weisberg, A. J. Westphal, S. Wirick, D. Wooden, B. Wopenka, P. Wozniakiewicz, I. Wright, H. Yabuta, H. Yano, E. D. Young, R. N. Zare, T. Zega, K. Ziegler, L. Zimmerman, E. Zinner, and M. Zolensky. Comet 81P/Wild 2 Under a Microscope. *Science*, 314: 1711–1716, December 2006.

J. A. Burns, P. L. Lamy, and S. Soter. Radiation forces on small particles in the solar system. *Icarus*, 40:1–48, October 1979.

A. N. Cox. *Allen's astrophysical quantities*. Allen's astrophysical quantities, 4th ed. Publisher: New York: AIP Press; Springer, 2000. Edited by Arthur N. Cox. ISBN: 0387987460, 2000.

J. F. Crifo, G. A. Lukyanov, V. V. Zakharov, and A. V. Rodionov. Physical Model of the coma of Comet 67P/Churyumov-Gerasimenko. In L. Colangeli, E. Mazzotta Epifani, and P. Palumbo, editors, *ASSL Vol. 311: The New Rosetta Targets. Observations, Simulations and Instrument Performances*, pages 119–130, October 2004.

J. Crovisier, P. Colom, E. Gérard, D. Bockelée-Morvan, and G. Bourgois. Observations at Nançay of the OH 18-cm lines in comets. The data base. Observations made from 1982 to 1999. *A&A*, 393:1053–1064, October 2002.

N. Divine. A simple radiation model of cometary dust for P/Halley. In *ESA SP-174: The Comet Halley. Dust and Gas Environment*, pages 47–53, November 1981.

N. Divine, H. Fechtig, T. I. Gombosi, M. S. Hanner, H. U. Keller, S. M. Larson, D. A. Mendis, R. L. Newburn, R. Reinhard, Z. Sekanina, and D. K. Yeomans. The Comet Halley dust and gas environment. *Space Science Reviews*, 43:1–104, February 1986.

N. Divine and R. L. Newburn. Modeling Halley before and after the encounters. *A&A*, 187:867–872, November 1987.

T. Erben, M. Schirmer, J. P. Dietrich, O. Cordes, L. Haberzettl, M. Hetterscheidt, H. Hildebrandt, O. Schmithuesen, P. Schneider, P. Simon, E. Deul, R. N. Hook, N. Kaiser, M. Radovich, C. Benoist, M. Nonino, L. F. Olsen, I. Prandoni, R. Wichmann, S. Zaggia, D. Bomans, R. J. Dettmar, and J. M. Miralles. GaBoDS: The Garching-Bonn Deep Survey. IV. Methods for the image reduction of multi-chip cameras demonstrated on data from the ESO Wide-Field Imager. *Astronomische Nachrichten*, 326:432–464, 2005.

P. Feldman, M. A'Hearn, and M. Festou. Observations of Comet 67P/Churyumov-Gerasimenko with the International Ultraviolet Explorer at Perihelion in 1982. In L. Colangeli, E. Mazzotta Epifani, and P. Palumbo, editors, *ASSL Vol. 311: The New Rosetta Targets. Observations, Simulations and Instrument Performances*, pages 47–52, October 2004.

J. Fertig and G. H. Schwehm. Dust environment models for comet P/Halley: Support for targeting of the GIOTTO S/C. *Advances in Space Research*, 4:213–216, 1984.

M. L. Finson and R. F. Probstein. A theory of dust comets. I. Model and equations. *ApJ*, 154:327–352, 1968.

M. P. Fitzgerald. The Intrinsic Colours of Stars and Two-Colour Reddening Lines. *A&A*, 4:234–243, February 1970.

M. Fulle. Motion of cometary dust. In M. C. Festou, H. U. Keller, and H. A. Weaver, editors, *Comets II*, pages 565–575, 2004.

M. Fulle, C. Barbieri, G. Cemonese, H. Rauer, M. Weiler, G. Milani, and R. Ligustri. The dust environment of comet 67P/Churyumov-Gerasimenko. *A&A*, 422:357–368, July 2004.

M. Fulle, L. Colangeli, V. Mennella, A. Rotundi, and E. Bussoletti. The sensitivity of the size distribution to the grain dynamics: simulation of the dust flux measured by GIOTTO at P/Halley. *A&A*, 304:622–630, December 1995.

R. D. Gehrz and E. P. Ney. 0.7- to 23-micron photometric observations of P/Halley 2986 III and six recent bright comets. *Icarus*, 100:162–186, November 1992.

S. F. Green, J. A. M. McDonnell, N. McBride, M. T. S. H. Colwell, A. J. Tuzzolino, T. E. Economou, P. Tsou, B. C. Clark, and D. E. Brownlee. The dust mass distribution of comet 81P/Wild 2. *Journal of Geophysical Research (Planets)*, 109(E18):E12S04, December 2004.

J. M. Greenberg and A. Li. Morphological Structure and Chemical Composition of Cometary Nuclei and Dust. *Space Science Reviews*, 90:149–161, October 1999.

E. Grün and E. K. Jessberger. Dust. In W. Huebner, editor, *Physics and Chemistry of Comets*, pages 113–176, 1990.

B. A. S. Gustafson. Physics of Zodiacal Dust. *Annual Review of Earth and Planetary Sciences*, 22:553–595, 1994.

B. A. S. Gustafson, J. M. Greenberg, L. Kolokolova, Y. Xu, and R. Stognienko. Interactions with Electromagnetic Radiation: Theory and Laboratory Simulations. In E. Grün, B. A. S. Gustafson, S. F. Dermott, and H. Fechtig, editors, *Interplanetary Dust*, pages 509–558, 2001.

M. S. Hanner. The Mineralogy of Cometary Dust. In T. K. Henning, editor, *LNP Vol. 609: Astromineralogy*, pages 171–188, 2003.

M. S. Hanner, R. H. Giese, K. Weiss, and R. Zerull. On the definition of albedo and application to irregular particles. *A&A*, 104:42–46, December 1981.

M. S. Hanner and R. L. Newburn. Infrared photometry of comet Wilson (1986l) at two epochs. *AJ*, 97:254–261, January 1989.

M. S. Hanner, E. Tedesco, A. T. Tokunaga, G. J. Veeder, D. F. Lester, F. C. Witteborn, J. D. Bregman, J. Gradie, and L. Lebofsky. The dust coma of periodic Comet Churyumov-Gerasimenko (1982 VIII). *Icarus*, 64:11–19, October 1985.

F. Hörz, R. Bastien, J. Borg, J. P. Bradley, J. C. Bridges, D. E. Brownlee, M. J. Burchell, M. Chi, M. J. Cintala, Z. R. Dai, Z. Djouadi, G. Dominguez, T. E. Economou, S. A. J. Fairey, C. Floss, I. A. Franchi, G. A. Graham, S. F. Green, P. Heck, P. Hoppe, J. Huth, H. Ishii, A. T. Kearsley, J. Kissel, J. Leitner, H. Leroux, K. Marhas, K. Messenger, C. S. Schwandt, T. H. See, C. Snead, F. J. Stadermann, T. Stephan, R. Stroud, N. Teslich, J. M. Trigo-Rodríguez, A. J. Tuzzolino, D. Troadec, P. Tsou, J. Warren, A. Westphal, P. Wozniakiewicz, I. Wright, and E. Zinner. Impact Features on Stardust: Implications for Comet 81P/Wild 2 Dust. *Science*, 314:1716–1719, December 2006.

P. Jenniskens. Discoveries from Observations and Modeling of the 1998/99 Leonids. In E. Grün, B. A. S. Gustafson, S. F. Dermott, and H. Fechtig, editors, *Interplanetary Dust*, pages 233–252, 2001.

M. S. Kelley, C. E. Woodward, D. E. Harker, W. T. Reach, R. D. Gehrz, and Spitzer GO Comet Team. Comet Astromineralogy with Spitzer: Initial Results. *American Astronomical Society Meeting Abstracts*, 207:#04.17, December 2005.

M. S. Kelley, C. E. Woodward, D. E. Harker, D. H. Wooden, R. D. Gehrz, H. Campins, M. S. Hanner, S. M. Lederer, D. J. Osip, J. Pittichová, and E. Polomski. A Spitzer Study of Comets 2P/Encke, 67P/Churyumov-Gerasimenko, and C/2001 HT50 (LINEAR-NEAT). *ApJ*, 651:1256–1271, November 2006.

M. R. Kidger. Dust production and coma morphology of 67P/Churyumov-Gerasimenko during the 2002-2003 apparition. *A&A*, 408:767–774, September 2003.

H. Kimura and C. Liu. On the structure of cometary dust tails. *Chin. Astron.*, 1:235–264, 1977.

L. Kolokolova, M. S. Hanner, A.-C. Levasseur-Regourd, and B. Å. S. Gustafson. Physical properties of cometary dust from light scattering and thermal emission. In M. C. Festou, H. U. Keller, and H. A. Weaver, editors, *Comets II*, pages 577–604, 2004.

E. D. Kondrateva and E. A. Reznikov. Comet Tempel-Tuttle and the Leonid meteor swarm. *Astronomicheskii Vestnik*, 19:144–151, October 1985.

P. L. Lamy, I. Toth, B. J. R. Davidsson, O. Groussin, P. Gutiérrez, L. Jorda, M. Kaasalainen, and S. C. Lowry. A Portrait of the Nucleus of Comet 67P/Churyumov-Gerasimenko. *Space Science Reviews*, pages 74–117, February 2007.

P. L. Lamy, I. Toth, H. Weaver, L. Jorda, and M. Kaasalainen. The Nucleus of Comet 67P/Churyumov-Gerasimenko, the New Target of the Rosetta Mission. *AAS/Division for Planetary Sciences Meeting*, 35, May 2003.

P. L. Lamy, I. Toth, H. A. Weaver, L. Jorda, M. Kaasalainen, and P. J. Gutiérrez. Hubble Space Telescope observations of the nucleus and inner coma of comet 67P/Churyumov-Gerasimenko. *A&A*, 458:669–678, November 2006.

M. Landgraf, M. Müller, and E. Grün. Prediction of the in-situ dust measurements of the stardust mission to comet 81P/Wild 2. *Planet. Space Sci.*, 47:1029–1050, August 1999.

C. M. Lisse, J. VanCleve, A. C. Adams, M. F. A'Hearn, Y. R. Fernández, T. L. Farnham, L. Armus, C. J. Grillmair, J. Ingalls, M. J. S. Belton, O. Groussin, L. A. McFadden, K. J. Meech, P. H. Schultz, B. C. Clark, L. M. Feaga, and J. M. Sunshine. Spitzer Spectral Observations of the Deep Impact Ejecta. *Science*, 313:635–640, August 2006.

S. C. Lowry, A. Fitzsimmons, and S. Collander-Brown. CCD photometry of distant comets. III. Ensemble properties of Jupiter-family comets. *A&A*, 397:329–343, January 2003.

M. Müller, S. F. Green, and N. McBride. Constraining cometary ejection models from meteor storm observations. In *ESA SP-495: Meteoroids 2001 Conference*, pages 47–54, November 2001.

J. T. T. Mäkinen. Water production rate of comet 67P/Churyumov-Gerasimenko. In L. Colangeli, E. Mazzotta Epifani, and P. Palumbo, editors, *ASSL Vol. 311: The New Rosetta Targets. Observations, Simulations and Instrument Performances*, pages 61–68, October 2004.

D. Makovoz and I. Khan. Mosaicking with MOPEX. In P. Shopbell, M. Britton, and R. Ebert, editors, *Astronomical Data Analysis Software and Systems XIV*, volume 347 of *Astronomical Society of the Pacific Conference Series*, pages 81–85, December 2005.

B. G. Marsden. Reports on the Progress of Astronomy: Comets. *Quarterly Journal of the Royal Astronomical Society*, 11:221–235, 1970.

L. Massonne. Coma morphology and dust emission pattern of Comet Halley. *Advances in Space Research*, 5:187–196, 1985.

L. Massonne. Modeling of a cometary dust coma. *Ph.D. Thesis*, 1987.

J. A. M. McDonnell, G. C. Evans, S. T. Evans, W. M. Alexander, W. M. Burton, J. G. Firth, E. Bussoletti, R. J. L. Grard, M. S. Hanner, and Z. Sekanina. The dust distribution within the inner coma of comet P/Halley 1982i - Encounter by Giotto's impact detectors. *A&A*, 187:719–741, November 1987.

J. A. M. McDonnell, P. L. Lamy, and G. S. Pankiewicz. Physical properties of cometary dust. In R. L. Newburn, Jr., M. Neugebauer, and J. Rahe, editors, *ASSL Vol. 167: IAU Colloq. 116: Comets in the post-Halley era*, pages 1043–1073, 1991.

J. A. M. McDonnell, N. McBride, R. Beard, E. Bussoletti, L. Colangeli, P. Eberhardt, J. G. Firth, R. Grard, S. F. Green, and J. M. Greenberg. Dust particle impacts during the Giotto encounter with Comet Grigg-Skjellerup. *Nature*, 362:732–734, April 1993.

K. J. Meech and D. C. Jewitt. Observations of Comet P/Halley at minimum phase angle. *A&A*, 187:585–593, November 1987.

G. Mie. Beitrge zur Optik trber Medien, speziell kolloidaler Metallsungen. *Ann. Physik*, 25:377–445, November 1908.

R. L. Millis, M. F. Ahearn, and D. T. Thompson. Narrowband photometry of Comet P/Stephan-Oterma and the backscattering properties of cometary grains. *AJ*, 87:1310–1317, September 1982.

R. L. Minkowski and G. O. Abell. *The National Geographic Society-Palomar Observatory Sky Survey*, pages 481–+. Basic Astronomical Data: Stars and stellar systems, edited by K. A. Strand. Published by the University of Chicago Press, Chicago, IL USA, 1968, p.481, 1963.

D. G. Monet, S. E. Levine, B. Canzian, H. D. Ables, A. R. Bird, C. C. Dahn, H. H. Guetter, H. C. Harris, A. A. Henden, S. K. Leggett, H. F. Levison, C. B. Luginbuhl, J. Martini, A. K. B. Monet, J. A. Munn, J. R. Pier, A. R. Rhodes, B. Riepe, S. Sell, R. C. Stone, F. J. Vrba, R. L. Walker, G. Westerhout, R. J. Brucato, I. N. Reid, W. Schoening, M. Hartley, M. A. Read, and S. B. Tritton. The USNO-B Catalog. *AJ*, 125:984–993, 2003.

F. Moreno, L. M. Lara, O. Muñoz, J. J. López-Moreno, and A. Molina. Dust in Comet 67P/Churyumov-Gerasimenko. *ApJ*, 613:1263–1269, October 2004.

B. E. A. Mueller. CCD-photometry of comets at large heliocentric distances. In A. W. Harris and E. Bowell, editors, *Asteroids, Comets, Meteors 1991*, pages 425–428, December 1992.

M. Müller. A Model of the Inner Coma of Comets with Applications to the Comets P/Wirtanen and P/Wild 2. PhD Thesis, Universität Heidelberg., May 1999.

M. Müller and E. Grün. An Engineering Model of the Dust Environment of the Inner Coma of Comet P/Wirtanen, Part 1. *ESA-RO-ESC-TA-5501*, 1997.

M. Müller and E. Grün. An Engineering Model of the Dust Environment of the Inner Coma of Comet P/Wirtanen, Part 2. *ESA-RO-ESC-TA-5501*, 1998.

M. Müller, N. McBride, S. F. Green, and J. C. Zarnecki. Prediction of the 2001 Leonid activity and an assessment of the spacecraft impact hazard. *Royal Society of London Philosophical Transactions Series A*, 361:175–179, January 2003.

E. P. Ney. Multiband photometry of Comets Kohoutek, Bennett, Bradfield, and Encke. *Icarus*, 23:551–560, December 1974.

E. P. Ney. *Optical and infrared observations of bright comets in the range 0.5 micrometers to 20 micrometers. In* Comets *(L. Wilkening, ed.)*, pages 323–340. Univ. of Arizona, Tucson, 1982.

E. P. Ney and K. M. Merrill. Comet West and the scattering function of cometary dust. *Science*, 194:1051–1053, December 1976.

D. J. Osip, D. G. Schleicher, and R. L. Millis. Comets - Groundbased observations of spacecraft mission candidates. *Icarus*, 98:115–124, July 1992.

W. T. Reach, M. S. Kelley, and M. V. Sykes. A survey of debris trails from short-period comets. *ArXiv e-prints*, 704, April 2007.

I. N. Reid, C. Brewer, R. J. Brucato, W. R. McKinley, A. Maury, D. Mendenhall, J. R. Mould, J. Mueller, G. Neugebauer, J. Phinney, W. L. W. Sargent, J. Schombert, and R. Thicksten. The second Palomar Sky Survey. *Publ. Astr. Soc. Pac.*, 103:661–674, July 1991.

R. Reinhard. The Giotto Encounter with Comet Halley. *Nature*, 321:313–318, May 1986.

K. Richter, W. Curdt, and H. U. Keller. Velocity of individual large dust particles ejected from Comet P/Halley. *A&A*, 250:548–555, October 1991.

G. H. Rieke, E. T. Young, C. W. Engelbracht, D. M. Kelly, F. J. Low, E. E. Haller, J. W. Beeman, K. D. Gordon, J. A. Stansberry, K. A. Misselt, J. Cadien, J. E. Morrison, G. Rivlis, W. B. Latter, A. Noriega-Crespo, D. L. Padgett, K. R. Stapelfeldt, D. C. Hines, E. Egami, J. Muzerolle, A. Alonso-Herrero, M. Blaylock, H. Dole, J. L. Hinz, E. Le Floc'h, C. Papovich, P. G. Pérez-González, P. S. Smith, K. Y. L. Su, L. Bennett, D. T. Frayer, D. Henderson, N. Lu, F. Masci, M. Pesenson, L. Rebull, J. Rho, J. Keene, S. Stolovy, S. Wachter, W. Wheaton, M. W. Werner, and P. L. Richards. The Multiband Imaging Photometer for Spitzer (MIPS). *ApJS*, 154:25–29, September 2004.

D. G. Schleicher. Compositional and physical results for Rosetta's new target Comet 67P/Churyumov Gerasimenko from narrowband photometry and imaging. *Icarus*, 181: 442–457, April 2006.

D. G. Schleicher, R. L. Millis, and P. V. Birch. Narrowband Photometry of Comet P/Halley: Variation with Heliocentric Distance, Season, and Solar Phase Angle. *Icarus*, 132:397–417, April 1998.

R. Schulz, J. A. Stüwe, and H. Boehnhardt. Rosetta target comet 67P/Churyumov-Gerasimenko. Postperihelion gas and dust production rates. *A&A*, 422:L19–L21, July 2004a.

R. Schulz, J. A. Stüwe, and H. Böhnhardt. Monitoring Comet 67P/Churyumov-Gerasimenko from ESO in 2003. In L. Colangeli, E. Mazzotta Epifani, and P. Palumbo, editors, *ASSL Vol. 311: The New Rosetta Targets. Observations, Simulations and Instrument Performances*, pages 15–24, October 2004b.

Z. Sekanina and H. E. Schuster. Meteoroids from periodic comet d'Arrest. *A&A*, 65: 29–35, April 1978.

A. D. Storrs, A. L. Cochran, and E. S. Barker. Spectrophotometry of the continuum in 18 comets. *Icarus*, 98:163–178, August 1992.

M. V. Sykes, D. M. Hunten, and F. J. Low. Preliminary analysis of cometary dust trails. *Advances in Space Research*, 6:67–78, 1986a.

M. V. Sykes, L. A. Lebofsky, D. M. Hunten, and F. Low. The discovery of dust trails in the orbits of periodic comets. *Science*, 232:1115–1117, 1986b.

M. V. Sykes and R. G. Walker. Cometary dust trails. I - Survey. *Icarus*, 95:180–210, 1992.

G. M. Szabó, L. L. Kiss, K. Sárneczky, and K. Sziládi. Spectrophotometry and structural analysis of 5 comets. *A&A*, 384:702–710, March 2002.

G. Tancredi, J. A. Fernández, H. Rickman, and J. Licandro. A catalog of observed nuclear magnitudes of Jupiter family comets. *A&A Suppl. Ser.*, 146:73–90, October 2000.

G. Tancredi, J. A. Fernández, H. Rickman, and J. Licandro. Nuclear magnitudes and the size distribution of Jupiter family comets. *Icarus*, 182:527–549, June 2006.

A. T. Tokunaga, W. F. Golisch, D. M. Griep, C. D. Kaminski, and M. S. Hanner. The NASA infrared telescope facility Comet Halley monitoring program. I - Preperihelion results. *AJ*, 92:1183–1190, November 1986.

A. J. Tuzzolino, T. E. Economou, B. C. Clark, P. Tsou, D. E. Brownlee, S. F. Green, J. A. M. McDonnell, N. McBride, and M. T. S. H. Colwell. Dust Measurements in the Coma of Comet 81P/Wild 2 by the Dust Flux Monitor Instrument. *Science*, 304: 1776–1780, June 2004.

M. Weiler, H. Rauer, and J. Helbert. Optical observations of Comet 67P/Churyumov-Gerasimenko. *A&A*, 414:749–755, February 2004.

M. W. Werner, T. L. Roellig, F. J. Low, G. H. Rieke, M. Rieke, W. F. Hoffmann, E. Young, J. R. Houck, B. Brandl, G. G. Fazio, J. L. Hora, R. D. Gehrz, G. Helou, B. T. Soifer, J. Stauffer, J. Keene, P. Eisenhardt, D. Gallagher, T. N. Gautier, W. Irace, C. R. Lawrence, L. Simmons, J. E. Van Cleve, M. Jura, E. L. Wright, and D. P. Cruikshank. The Spitzer Space Telescope Mission. *ApJS*, 154:1–9, September 2004.

F. L. Whipple. A comet model. I. The acceleration of Comet Encke. *ApJ*, 111:375–394, March 1950.

F. L. Whipple. A Comet Model. II. Physical Relations for Comets and Meteors. *ApJ*, 113: 464–474, May 1951.

Acknowledgements

Many people have supported and encouraged me during the work that has finally resulted in the writing of this thesis. First and foremost, my gratitude is to Professor Eberhard Grün for having accepted me as his student, for teaching me optimism, for encouraging me to present and publish my results, for giving me the independence I wanted, and the advice I needed.

Michael Müller was an unfailing mentor for the modelling aspects of this work, his works were not only the starting point for my efforts but have proved invaluable guides along the way. Hermann Böhnhardt introduced me to the world of telescopes and flat-fields, and helped me to actually find the comet in the pile of FITS files that arrived on my desk one day. To William Reach I am deeply grateful for imparting to me some of his intimate knowledge of the Spitzer Space Telescope and for his detailed and precise guidelines throughout the observation campaign. I thank Mark Sykes and David Lien for making me feel welcome in Tucson, Arizona, and for the extensive and stimulating discussions. Philippe Lamy opened my eyes to the complexity of dust interacting with radiation, I am indebted to him for some valuable pieces of advice. I am grateful to Jürgen Fertig for having supported this work to be carried out as a cooperation between the European Space Operations Centre in Darmstadt and the Max Planck Institute for Nuclear Physics in Heidelberg.

I am immensely thankful to Nicolas Altobelli, Uwe Beckmann, Valeri Dikarev, Stefan Helfert, Sean Hsu, Sascha Kempf, Harald Krüger, Gudrun Linkert, Anna Mocker, Richard Moissl, Georg Moragas-Klostermeyer, Wolfgang Müller, Frank Postberg, Ralf Srama and all other present and former members of the Heidelberg Dust Group family for their always unhesitating support. Their frankness, enthusiasm, animated discussions and merry coffee breaks have made these four years joyful and unforgettable.

Substantial funding for this work was provided by the Cassini Project, by the European Space Agency and by the Studienstiftung des deutschen Volkes. The Max Planck Institute for Nuclear Physics admitted me as a guest and generously supported many journeys, enabling me to meet with and learn from scientists around the world. Travels were also facilitated by the European Space Research and Technology Centre, the Deutsche Forschungsgemeinschaft, the Observatoire Astronomique de Marseille Provence, and the University of Hawaii. I am particularly grateful to the Studienstiftung des deutschen Volkes and to the Max Planck Institute for Nuclear Physics for supporting my efforts to reconcile the demands of a young family with those of PhD work.

This work is based on observations made with the MPG/ESO 2.2m telescope at the La Silla Observatory under programme ID 072.A-9011(A), and with the Spitzer Space Telescope under programme ID 20235, which is operated by the Jet Propulsion Laboratory, California Institute of Technology under a contract with NASA. The research has made use of the USNOFS Image and Catalogue Archive operated by the United States Naval Observatory, Flagstaff Station. Ephemerides were obtained from the HORIZONS system provided by the Solar System Dynamics Group of the Jet Propulsion Laboratory.

Image processing was done with IRAF, which is written and supported by the IRAF programming group at the National Optical Astronomy Observatories (NOAO) in Tucson, Arizona, and with MOPEX, developed at the Spitzer Science Center, Jet Propulsion Laboratory, California Institute of Technology. Use was made of SAOImage DS9, developed by the Smithsonian Astrophysical Observatory, and of numerous other software packages provided by both the astronomical and the free software communities. This thesis was processed with LaTeX.

Following the strange custom to mention those last that are dearest to one, I wish to thank Jens for being a companion to share enthusiasm, belief and doubts. I am grateful to my parents for their love and specifically for their being wonderful grandparents to Clemens, who has had to share his mother with the comet from the very beginning. His – nearly – unlimited patience and cheerfulness are the greatest gifts.

Jessica Agarwal
Heidelberg, June 2007